



THE HONG KONG
POLYTECHNIC UNIVERSITY

香港理工大學

Pao Yue-kong Library

包玉剛圖書館

Copyright Undertaking

This thesis is protected by copyright, with all rights reserved.

By reading and using the thesis, the reader understands and agrees to the following terms:

1. The reader will abide by the rules and legal ordinances governing copyright regarding the use of the thesis.
2. The reader will use the thesis for the purpose of research or private study only and not for distribution or further reproduction or any other purpose.
3. The reader agrees to indemnify and hold the University harmless from and against any loss, damage, cost, liability or expenses arising from copyright infringement or unauthorized usage.

IMPORTANT

If you have reasons to believe that any materials in this thesis are deemed not suitable to be distributed in this form, or a copyright owner having difficulty with the material being included in our database, please contact lbsys@polyu.edu.hk providing details. The Library will look into your claim and consider taking remedial action upon receipt of the written requests.

**Design, Fabrication, and Characterization
of Flexible, Wearable and Highly Durable
Strain Sensors Assisted by Bioinspired
Polydopamine**

NIU BEN

PhD

The Hong Kong Polytechnic University

2021

The Hong Kong Polytechnic University

Institute of Textiles and Clothing

**Design, Fabrication and Characterization of Flexible, Wearable and
Highly Durable Strain Sensors Assisted by Bioinspired Polydopamine**

NIU BEN

**A thesis submitted in partial fulfilment of the requirements
for the degree of Doctor of Philosophy**

September 2020

Certificate of Originality

I hereby declare that this thesis is my own work and that, to the best of my knowledge and belief, it reproduces no material previously published or written, nor material that has been accepted for the award of any other degree or diploma, except where due acknowledgement has been made in the text.

(Signed)

NIU BEN

(Name of student)

Abstract

Due to the rapid development of the personal information platform and Internet of Things, more and more flexible and multifunctional sensors are being applied into our daily life, such as the field of smart textiles, human health monitoring, and soft robotics. As one of the hot research topics in sensing devices, strain sensors are attracting intensive attentions recently, which offers a facile way to transfer the complex physical movements into the readable electronic signal. However, it is still challenging to fabricate high-performance strain sensors with integratable capability into textile/clothing and qualified working durability and wearability for practical applications. To address the issues, this thesis focuses on designing and developing flexible and wearable strain sensors. Especially, the mussel-inspired polydopamine (PDA) is introduced to enhance the interface between the conductive materials and soft polymer substrate for notable durability.

At first, a new yarn-type strain sensor with both one-dimensional (1D) configuration and excellent weavability was developed by employing the commonly used elastic polyurethane yarn (PUY) as a substrate coated with a reduced graphene oxide (rGO) conductive layer, allowing the sensor to be incorporated within the textile structure easily and efficiently without interfering with the exceptional properties of the fabric as well as the comfort and aesthetic beauty of the clothing. Moreover, as a unique adhesive and skin-friendly material for packaging the sensing structure, mussel-inspired PDA

was introduced into the sensor system, leading to a great enhancement of the interfacial adhesion between the PUY core and conductive sheath, the stability of the sensing layer and the integrality of the sensor. The resultant yarn sensor exhibits excellent sensing properties, with a large gauge factor (131.8 at 90% strain), very low hysteresis, and especially perfect linearity (a correlation coefficient of 0.999). Of great importance is its superior durability even after longtime stretching–releasing for 30 000 cycles.

In addition, the sensing mechanism of the as-made 1D yarn strain sensor was studied by recording the cracks morphologies under different strains using scanning electron microscope (SEM), and then a finite element analysis (FEA) was conducted based on the SEM images to simulate the voltage drops of the strain sensors. It is proved that the resistance increase of the yarn strain sensor lies in the crack formation of the conductive rGO layer under strains. Moreover, prestretching was demonstrated as an effective method to adjust the electro-mechanical properties of the yarn strain sensor, and larger prestretching strain benefits higher sensitivity, lower hysteresis and repeatability errors. Moreover, benefiting from the reasonable design of structure and material system, the yarn strain sensor is proved to possess a good capability to sense multiple mechanical deformations of stretching and bending.

Subsequently, since the textile is considered as an ideal platform that can integrate diverse flexible electronic devices for developing textile-based wearable electronic systems. A 1D flexible sensor in a yarn-type configuration is an ideal device for a

textile-based wearable system, which can be easily woven and knitted into textile structures for fabricating fabrics via existing textile technologies. Based on the as-made yarn sensor, a new sensing textile was further developed by integrating the yarn sensor into the sateen fabric structure by using the automatic weaving machine. The obtained fabric sensor presents a very good and stable sensing performance even after 10 000 testing cycles. Moreover, the fabric sensor proves good wearability and efficiency for detecting various human motions.

At last, a facile method was put forward to fabricate mechanically and electrically durable e-textiles by chemical deposition of silver nanoparticles (AgNPs) on widely used cotton fabric. The interface between AgNPs and fabric was tightly strengthened by PDA, and a highly waterproof and anticorrosive surface was further obtained by modifying with a fluorine containing agent of *1H,1H,2H,2H*-perfluorodecanethiol (PFDT). Besides the low sheet resistance of 0.26 ohm/sq and high conductivity of 233.4 S/cm, the e-textiles present outstanding stability to different mechanical deformations including ultrasonication and machine washing. Moreover, this e-textile is capable to respond well to mechanical bending with a gauge factor of 7.1. Thanks to the surface roughness of AgNPs and low surface energy of PFDT, a superhydrophobic surface, with a water contact angle of ca. 152°, was further obtained, endowing the e-textiles excellent anti-corrosion to water, acid/alkaline solution and various liquids (e.g. milk, coffee and tea). Moreover, the application of this highly conductive e-textiles in

wearable electrothermal heater is also demonstrated. Together with the facile, all-solution-based, and environmentally friendly fabrication protocol, the e-textiles show great potential of large-scale applications in wearable electronics.

In summary, this thesis carried out a systematic research on designing, fabricating and characterizing the new-type wearable textile-based strain sensors. These strain sensors possess excellent sensing performance and especially outstanding wearability, and of great importance is the greatly improved adhesion between conductive materials and the soft substrate by the introduction of bioinspired PDA, well solving the challenging stability problem of the strain sensors for practical applications. This study opens up a new prospect to combine the traditional textile technologies and materials science for preparing high-performance textile-based strain sensors. Furthermore, the facile and environmentally friendly methodologies developed are also versatile to other textile-based electronics, thus showing great potential in smart textiles.

List of Publications

Referred Journal Paper

1. **Niu B**, Hua T, Hu H, Xu B, Tian X, Chan K, Chen S. A highly durable textile-based sensor as a human-worn material interface for long-term multiple mechanical deformation sensing. *Journal of Materials Chemistry C*, 2019, 7, 14651-14663;
2. **Niu B**, Hua T, Xu B. Robust deposition of silver nanoparticles on paper assisted by polydopamine for green and flexible electrode. *ACS Sustainable Chemistry & Engineering*, 2020, 8, 12842-12851;
3. **Niu B**, Yang S, Hua T, Tian X, Koo M. Facile fabrication of highly conductive, waterproof, and washable e-textiles for wearable applications. *Nano Research*, 2020, DOI: [org/10.1007/s12274-020-3148-3](https://doi.org/10.1007/s12274-020-3148-3);
4. Hu H, Bai Z, **Niu B**, Wu M, Hua T, Binder-free bonding modularized MXene thin films into thick film electrodes for on-chip micro-supercapacitor with enhanced areal performance metrics, *Journal of Materials Chemistry A*, 2018, 6, 14876-14884.
5. Chen S, Tian X, Hua T, Chan K, Fu J, **Niu B**. Exploring the relationship between applied fabric strain and resultant local yarn strain within the elastic fabric based on finite element method, *Journal of Materials Science*, 2020, 55, 10258–10270.

6. Tian X, Chan K, Hua T, **Niu B**, Chen S. Wearable strain sensors enabled by integrating one-dimensional polydopamine-enhanced graphene/polyurethane sensing fibers into textile structures, *Journal of Materials Science*, 2020, 55, 17266-17283.

Conference Presentations

Oral Presentation

Niu B, Hua T, Xu B, Chen S, Lee N, Pang K. Enhancement of interface between graphene and polyurethane inspired by mussel for high-performance strain sensor. The Fiber Society 2019 Spring Conference, May 21–23, 2019, Hong Kong

Poster Presentation

Chen S, Hua T, **Niu B**, Tian X, Chan K. Mechanical model and simulation of yarn behavior within fabrics under uniaxial tension based on finite element method. The Fiber Society 2019 Spring Conference, May 21–23, 2019, Hong Kong (Best Poster Award)

Acknowledges

First of all, I would like to give my sincere appreciation to my chief supervisor Dr. Hua Tao for instructing and supporting me throughout my research studies. During the last three years, starting from the initial attempting in the field of flexible and wearable strain sensors, now I have acquired a much deeper understanding and richer research experience under his insightful and patient guidance, which is beneficial to me forever. Moreover, I would like to thank the financial support of the Research Grant Council of Hong Kong, Hong Kong Polytechnic University, and Institute of Textiles and Clothing, who provide a perfect platform for my research.

I would also like to thank my co-supervisor Prof. Xu Bingang and the technicians of the Institute of Textiles and Clothing as well as University Research Facility in Materials Characterization and Device Fabrication. In the meanwhile, I would like to thank all the members in Dr. Hua's group during the three years, who give a lot of kind help and useful advice to my research work.

At last, I would like to express gratitude to my families and friends, who always support me to persist in my educational career. With your encouragement, the tough road of research studying becomes warm and hopeful.

Table of Contents

Certificate of Originality	I
Abstract.....	II
List of Publications	VI
Acknowledges	VIII
List of Figures.....	XIII
List of Tables.....	XXIII
List of Abbreviations.....	XXIV
CHAPTER 1: Introduction.....	26
1.1 Background and Challenges	26
1.2 Research Objectives.....	29
1.3 Research Methodologies.....	31
1.4 Research Significance	36
1.5 Outline of the Thesis	38
CHAPTER 2. Literature Review.....	41
2.1 Structures and Classifications of Flexible Strain Sensors.....	41
2.1.1 Material Systems.....	45
2.1.2 Classifications	49
2.2 Sensing Mechanisms of Strain Sensors	54
2.3 Performances Evaluation of Strain Sensors	58
2.3.1 Stretchability	58
2.3.2 Sensitivity	60
2.3.3 Linearity.....	62
2.3.4 Hysteresis.....	64

2.3.5 Durability	65
2.3.6 Safety and wearing comfort	66
2.4 Structure Design Strategies Towards Desired Strain Sensors.....	68
2.4.1 Patterned structure	69
2.4.2 Auxetic structure	75
2.4.3 Hybrid structure	82
2.4.4 Prestretching	85
2.4.5 Self-cleaning	87
2.5 Fabrication Technologies	89
2.6 Summary	94

CHAPTER 3: Design and Fabrication of Flexible One-Dimensional Strain Sensor Based on Polyurethane Yarn, Graphene and Polydopamine Encapsulation96

3.1 Introduction.....	96
3.2 Experimental Section.....	101
3.2.1 Materials	101
3.2.2 Preparation	102
3.2.3 Characterization	103
3.3 Results and Discussion	104
3.3.1 Fabrication of yarn strain sensor.....	104
3.3.2 Morphology and structure of yarn strain sensor	106
3.3.3 Electro-mechanical properties of yarn sensor for sensing tensile strain and PDA influence	109
3.4 Conclusions.....	118

CHAPTER 4: Study of the Sensing Mechanism and Effects of Prestretching and Applied Bending on the Sensing Properties of One-Dimensional Strain Sensor119

4.1 Introduction.....	119
4.2 Experimental Section.....	121

4.2.1 Characterization	121
4.2.2 Finite element analysis.....	122
4.3 Results and Discussion	122
4.3.1 Sensing mechanism of one-dimensional yarn strain sensor	122
4.3.2 Effect of prestretching on the electro-mechanical properties of yarn sensor	131
4.3.3 Electro-mechanical properties of yarn sensor for sensing bending-induced strain	135
4.4 Conclusions.....	141
CHAPTER 5: Wearable Fabric Sensor by Integrating the One-Dimensional Yarn Sensor into Fabric	142
5.1 Introduction.....	142
5.2 Experimental Section	144
5.2.1 Preparation	144
5.2.2 Characterization	146
5.3 Results and Discussion	147
5.3.1 Fabrication of fabric sensors by weaving the 1D yarn sensor into fabric	147
5.3.2 Electromechanical properties of the fabric sensor	149
5.3.3 Effect of fabric structure on the sensing performance	157
5.3.4 Wearable fabric sensor prototypes for human motion detection.....	162
5.4 Conclusions.....	165
CHAPTER 6: Polydopamine Assisted Deposition of Silver Nanoparticles on Cotton Fabric for Highly Conductive E-Textiles as Wearable Strain Sensor and Heater	167
6.1 Introduction.....	167
6.2 Experimental Section	171
6.2.1 Materials	171
6.2.2 Preparation	172

6.2.3 Characterization	172
6.3 Results and Discussion	174
6.3.1 Fabrication procedures.....	174
6.3.2 Morphologies change of the e-textiles during preparation	179
6.3.3 Electrical response of the e-textiles to mechanical bending	183
6.3.4 Superhydrophobic and anti-corrosive properties	187
6.3.5 Electromechanical stability	190
6.4 Conclusions.....	198
CHAPTER 7: Conclusions and outlook	199
7.1 Conclusions.....	199
7.2 Outlook	202
REFERENCES.....	204

List of Figures

Fig 2.1 Scheme showing the four structures of strain sensors.

Fig 2.2 Schemes showing the deformation of conductive networks of two CPCs strain sensors: (a) MWCNT/PU and (b) graphene/PDMS.

Fig 2.3 The composition of flexible strain sensors: the sensing micro/nanomaterials and flexible polymer substrate

Fig 2.4 (A) The deformation of graphene network under strain of 50% of a typical graphene/PU yarn resistive-type strain sensor; (B) Sensing mechanism, sample schematic, SEM image of CNT networks in the electrode, and sample mounting scheme of a typical capacitive-type strain sensor. (C) Scheme showing the structure and working mechanism of a TENG based sensor.

Fig 2.5 (a) 1D strain sensor of coaxial TPE-wrapped SWCNT fibers; (b) 1D strain sensor of graphene/PU yarn composites; (c) 2D strain sensor of three-layer stacked PU-PEDOT:PSS/SWCNT/PU-PEDOT:PSS on a PDMS substrate; and (d) 3D strain sensor of CNT/PU auxetic foam.

Fig 2.6 Scheme showing (A) the tunneling effect in the CPC and (B) the deformation of AgNWs in the strain sensor of AgNWs/PDMS; (C) the crack propagation for the MXene/CNTs/PDMS strain sensor.

Fig 2.7 (a) Scheme showing the fabrication procedures of SWCNT strain sensor with open-mesh geometries, and (b) wrinkled CNT thin film on Ecoflex substrate.

Fig 2.8 (a) Effects of graphene concentration and number of coatings on the GF of yarn-

based strain sensor, (b) strain sensor with a sandwich-like $\text{Ti}_3\text{C}_2\text{T}_x$ MXene/CNT layer; (c) spider-inspired crack sensor; and (d) fabrication procedures for an ultrasensitive strain sensor by the aid a steel net.

Fig 2.9 Electrical signal development upon stretching for (a) capacitive and (b) resistive strain sensors, respectively.

Fig 2.10 (a) SEM image of a dense array of 50-nm radius Pt coated nanohairs; (b) SEM image of ZnO nanowires on the PDMS micropillars; (c) SEM image of a composite film with microdome arrays; (d) SEM images of AgNWs/PDMS film strain sensor with a densely packed microprism-array architecture.

Fig 2.11 Schematic illustration of the fabrication process of (a) AgNWs/PDMS strain sensor moulded by steel net; and (b) SWCNTs/PDMS strain sensor moulded by silk.

Fig 2.12 (a) Scheme showing the formation of beads on PDMS fiber based on the phenomenon of Plateau-Rayleigh, and the SEM images of the gold layer at different positions along the PDMS fiber; (b) fabrication flowchart of the microhairy fibers, and the structural scheme as well as SEM image of the microhairy conductive fibers twisted to another one fiber; (c) scheme showing the fabrication process of micro-nanoscale segmental soft-hard fibers, and the relationship between the pre-strain with the linearity and GF of the conductive fibers.

Fig 2.13 Scheme showing the deformation of (a) conventional flat film, and auxetics; (b) normalized displacement in transverse direction under nominal axial strain; and (c) bending behaviors of non-auxetic material and auxetic material, showing the saddle-

shape and dome-shape curve, respectively.

Fig 2.14 (a) Diagram of a strain sensor based on auxetic structure in bottom and top views. The strain sensor is composed of an auxetic PDMS frame prepared by 3D printing, PDMS film, and SWCNT network; (b) strain distribution from FEA simulation under a nominal strain of 15%; (c) GF and strain concentration ε_c comparison; (d) SEM images of microcracks distribution within the auxetic and flat strain sensors under a nominal strain of 15%; (e) applications of the auxetic film sensor in the radial pulse detection.

Fig 2.15 (a) Scheme of the structure conversion from conventional foams to auxetic foams; (b) photographs and corresponding SEM images of auxetic foam before and after stretching; (c) relative resistance change with respect to both tensile and compressive strain for conventional and auxetic foam sensors; and (d) illustration of the auxetic triboelectric nanogenerator.

Fig 2.16 Schematic illustration of (a) the interaction between CNTs and graphene, and the microstructural change of (b) CNTs thin film; (c) CNTs/graphene hybrid thin film under stretching and releasing; (d) hybrid networks in the graphene/CNTs/PU CPCs under different strains; (e) Scheme showing the structure change of AgNPs/graphene strain sensor in the three states of strain free, small strain, and large strain.

Fig 2.17 (a) Schematic illustration of fabrication process, structure and SEM image about the hierarchically buckled CNT sheath-rubber core fibers. (b) fabrication of conductive AgNWs shell-PU core fibers with wrinkled microstructures, and SEM

image of piezoresistive fibers by twisting two wrinkle microstructures fibers as pressure sensor; (c) Scheme and relevant SEM images of conductive TPU films coated with AgNWs/graphene layer after prestretching and releasing, and the resistance change versus strain curves of the conductive films treated by different pre-stretching strains.

Fig 2.18 Preparation steps of 1D strain sensors by (A) dip coating the PU yarn in graphene solution. (B) electro spinning of PU fibers, followed by dipping in CNTs solution. (C) infusing graphene into elastic bands. (D) dry-spinning CNT fiber on Ecoflex substrate and (E) coaxial wet-spinning of the CNT/PU sensing fibers.

Fig 2.19 Examples showing the different fabrication methods for 2D film strain sensors: (A) filtration method, (B) transferring and micromolding method, (C) printing technology, (D) solution mixing, (E) coating techniques, and (F) chemical vapor deposition.

Fig 2.20 (a) Sketch showing the fabrication process of foam-based pressure sensor, and the fabricated artificial skin based on the foam based pressure sensor; (b) Scheme showing the preparation process of aligned CNT/PU foam, and photo of a lightweight foam based pressure sensor standing on a flower.

Fig 3.1 The tensile stress versus strain curve of PUY, which was conducted by the machine of Instron 5944, with the gauge length of 10 cm and speed of 100 mm/min.

Fig 3.2 Scheme illustrating the preparation process of PDA/rGO/PUY strain sensors. (a) Dip coating in PVA solution. (b) Dip coating in rGO solution. (c) Reaction in dopamine solution. (d) Photo of the sensor of PDA/rGO/PUY wrapped around a pencil,

showing an excellent flexibility.

Fig 3.3 Scheme showing the chemical formation mechanism of PDA.

Fig 3.4 SEM morphologies of (a₁) PUY, (b₁) rGO/PUY, and (c₁) PDA/rGO/PUY strain sensor on the cross section, and SEM morphologies of (a₂, a₃) PUY, (b₂, b₃) rGO/PUY and (c₂, c₃) PDA/rGO/PUY strain sensor along the length direction respectively.

Fig 3.5 FTIR curves of PUY, rGO/PUY, PDA, and PDA/rGO/PUY strain sensor.

Fig 3.6 Electro-mechanical properties of the PDA/rGO/PUY strain sensor under different strains.

Fig 3.7 The development of GF, R^2 , and δh of the strain sensor under strains from 10% to 90%.

Fig 3.8 Resistance change versus a strain of 50%, and SEM images showing the surface morphologies' change during the stretching and releasing of the sensor.

Fig 3.9 Schematic illustrations showing the resistance model of the sensor and the equivalent circuit.

Fig 3.10 Durability of the PDA/rGO/PUY sensor undergoing the stretching-releasing cycles of 30000 (under the strain of 50% and stretching-releasing speed of 100 mm min⁻¹).

Fig 3.11 The electro-mechanical properties of the PDA/rGO/PUY sensor under varied stretching-releasing speeds at a strain of 50%.

Fig 3.12 The response and recovery curves of (a) rGO/PUY and (b) PDA/rGO/PUY under a small strain of 5% and a testing speed of 600 mm/min.

Fig 3.13 (a) Comparison on the resistance-strain curves between rGO/PUY and PDA/rGO/PUY sensors. (b) Comparison of sensing properties, in terms of GF, R^2 , δh , and durability between rGO/PUY and PDA/rGO/PUY sensors.

Fig 3.14 Electro-mechanical curves of the sensing yarn before and after sweat dipping. (a) 50 cycles. (b) 3 cycles. (For the effect of sweat, the sensing yarn was dipped into an artificial sweat (pH 8.0) for 30 min at room temperature, and then the sensor was cleaned by deionized water and fully dried in the air.)

Fig 4.1 SEM images of the yarn strain sensor at strains from 0% to 50%, and the stretching direction is horizontal.

Fig 4.2 The relationship curves between the crack percentage and relative resistance change with the applied strain.

Fig 4.3 Scheme showing the effect of different crack models on the current flow of conductive rGO layer.

Fig 4.4 Flow chart of the voltage drop simulation process: (a) original SEM image. (b) binarized SEM image by vectorization. (c) boundary conditions applied. (d) simulation method of KCL. (e) image after meshing. (f) calculated results of potential distribution.

Fig 4.5 Current flow of unit $V_{i,j}$ with the neighboring units.

Fig 4.6 Simulated potential distribution of the SEM images in Fig 4.1.

Fig 4.7 (a) Initial resistance change curve of 20 cycles at a strain of 50% without prestretching. (b) Resistance change-strain relationship at a strain of 50% after prestretching at different strains.

Fig 4.8 (a) GF and R^2 of the PDA/rGO/PUY sensor after prestretching at different strains. (b) Hysteresis and repeatability errors of the PDA/rGO/PUY sensor after prestretching at different strains.

Fig 4.9 Scheme showing the sensing mechanism of the sensor.

Fig 4.10 Bending properties of the sensor. (a) Photo of the experimental setup for bending test (diameter of the pressure head is 30 mm). (b) Dependence of resistance change on displacement of the pressure head during bending and releasing (movement speed of the pressure head is 100 mm/min).

Fig 4.11 Scheme showing the two situations during the bending process of the strain sensor: (a) $d \leq r$ and (b) $d > r$.

Fig 4.12 Cyclic stability test of compressive bending of the sensing (a) yarn and (b) fabric under the displacement of moving pressure head of 10 mm and the movement speed of pressure head of 100 mm/min.

Fig 5.1 Photographs showing (a) the weaving system. (b) the control software. (c) weaving process. (d) the obtained fabric during weaving.

Fig 5.2 Architecture of sateen fabric with the black arrow for indicating the intended position for the yarn sensor

Fig 5.3 (a) Fabric structure for integrating the sensing yarn. (b) Scheme of the weaving process. (c) Photo of the fabric sensor.

Fig 5.4 (a) Resistance change–time curve during stretching–releasing cycles. (b) Relative resistance change–strain curve of the fabric sensor.

Fig 5.5 (a) The response and recovery curves the fabric sensors under a small strain of 5% and a testing speed of 600 mm/min. (b) The electromechanical properties of the fabric sensor under varied stretching–releasing speeds at a strain of 50%.

Fig 5.6 Durability test of the fabric sensor for tension.

Fig 5.7 Cyclic stability test of compressive bending of the fabric sensor under the displacement of moving pressure head of 10 mm and the movement speed of pressure head of 100 mm/min.

Fig 5.8 The sensing performance change of the fabric sensor before and after washing.

Fig 5.9 Optical image of fabric cross-section for examining the yarn configuration under increased strain from 0% to 50%.

Fig 5.10 (a) Comparison between the applied strain on fabric and actual yarn strain. (b) The applied boundary conditions for FEM.

Fig 5.11 Wearing demonstrations of yarn sensor in monitoring the chewing.

Fig 5.12 Wearing demonstrations of fabrics sensors in monitoring human motions. (a) Relative resistance change of sensing wrist-band made of fabric sensor during palm opening and closing. (b) Relative resistance change of different elbow bending degrees.

Fig 5.13 Wearing demonstrations of fabric sensors in monitoring human motions. (a) Relative resistance change of sensing knee-band in detecting leg bending and (b) gait during walking upstairs.

Fig 6.1 Scheme showing (a) the fabrication process and (b) chemical reactions of PFDT/Ag/PDA/CF e-textiles. (c) Scheme showing the molecular structure of

PFDT/Ag/PDA/CF e-textiles.

Fig 6.2 The relationship between the AgNO₃ concentration and the sheet resistance of Ag/PDA/CF and PFDT/Ag/PDA/CF.

Fig 6.3 (a) TGA curves of CF, PDA/CF, and Ag/PDA/CF, respectively. (b) Tensile properties of CF, PDA/CF, and PFDT/Ag/PDA/CF.

Fig 6.4 Photographs of (a) the electric resistance of a e-textile sample with dimension of 40 mm×10 mm, and (b) a large area sample.

Fig 6.5 SEM images of (a, b) pristine CF with different magnifications, (c) PDA/CF, (d-f) Ag/PDA/CF with different magnifications, (g) PFDT/Ag/PDA/CF e-textiles and the relevant elemental mapping of (h) Ag and (i) F, (j-l) Cross-sectional SEM images of the e-textiles with different magnifications.

Fig 6.6 (a) Photographs of the pristine CF and PDA/CF. (b) FTIR curves of CF, PDA, and PDA/CF, respectively. (c) XPS curves of the CF and PDA/CF samples.

Fig 6.7 (a) Relative resistance change of the e-textiles under different bending length and (b) bending length of 10 mm for 500 cycles.

Fig 6.8 (a) Schemes illustrating the electrical resistance model. Photographs showing the LEDs connected by e-textiles under (b) flat and (c) bent states.

Fig 6.9 (a) Water CAs of CF, PDA/CF, Ag/PDA/CF and PFDT/Ag/PDA/CF, and the insets showing the non-adhesive surface of PFDT/Ag/PDA/CF e-textiles. (b) Resistance stability of PFDT/Ag/PDA/CF e-textiles immersed in water, and insets of application as interconnects underwater. (c) CAs for water, HCl solution (0.1 mol/L)

and NaOH solution (0.1 mol/L) on the surface of PFDT/Ag/PDA/CF e-textiles.

Photographs showing the state of different liquid droplets on the surface of (d)

PFDT/Ag/PDA/CF e-textiles and (e) CF.

Fig 6.10 (a) The relative resistance change of the e-textiles after different cycles of ultrasonication, where the insets show the water CA and SEM surface morphologies after 6 cycles' ultrasonication. (b) The sheet resistance changes of e-textile after different cycles of ultrasonication.

Fig 6.11 (a) The relative resistance change of the e-textiles after different cycles of machine washing, where the insets show the water CA and SEM surface morphologies after 6 cycles' machine washing. (b) The sheet resistance changes of e-textile after different cycles of machine washing.

Fig 6.12. (a) Photograph showing the abrasion testing setup (b) the sheet resistance change of the e-textile with increasing abrasion cycles; (c-d) SEM images of the e-textile sample after abrasion testing of 1000 cycles.

Fig 6.13 (a) Time-dependent temperature development of the e-textiles under different voltages. (b) Current-Voltage curve of the e-textile. (c) Experimental results of T_s versus U^2 and the linear fitting. (d) Temperature development of the e-textiles under cyclic heating and cooling test applied with a voltage of 3V.

Fig 6.14 The deicing performance of the e-textiles applied (a) with a voltage of 3V and (b) without voltage. (c) IR images of the e-textiles attached on the human finger as wearable heater before and after the applying of a 3V voltage.

List of Tables

Table 4.1 Performance comparisons to recently reported 1D strain sensors.

Table 5.1 Specifications of the sensing sateen fabric.

Table 5.2 Performance comparisons to related state of the art 2D textile-based strain sensors

Table 5.3 Sensing parameters comparison between 1D yarn sensor and 2D fabric sensor

List of Abbreviations

SEM	Scanning electronic microscope
TGA	Thermogravimetric analysis
FTIR	Fourier transform infrared spectroscopy
CA	Contact angle
EDS	Energy dispersive X-ray spectroscopy
rGO	Reduced graphene oxide
PU	Polyurethane
PUY	Polyurethane yarn
1D	One-dimensional
2D	Two-dimensional
3D	Three-dimensional
AgNPs	Ag nanoparticles
CF	Cotton fabric
FEA	Finite element analysis
GF	Gauge factor
PDA	Polydopamine
SLS	Sodium lauryl sulfate
PVA	Polyvinyl alcohol
PDMS	Polydimethylsiloxane
PFDT	1 <i>H</i> ,1 <i>H</i> ,2 <i>H</i> ,2 <i>H</i> -perfluorodecanethiol
AgNO ₃	Silver nitrate
HCl	Hydrochloric acid
NaOH	Sodium hydroxide
NH ₃ ·H ₂ O	Ammonium hydroxide
Tris	Tris(hydroxymethyl) aminomethane

CNTs	Carbon nanotubes
SWCNTs	Single-walled carbon nanotubes
MWCNTs	Mingle-walled carbon nanotubes
DHI	5,6-dihydroxyindole
R^2	Correlation coefficient
δh	Hysteresis error
LED	Light emitting diodes
CBs	Carbon blacks
PEDOT-PSS	Poly(3,4-ethylenedioxythiophene)-poly(styrenesulfonate)
AgNWs	Ag nanowires
PPy	Polypyrrole
CPCs	Conductive polymer composites
TENG	Triboelectric nanogenerator
SNR	Signal-to-noise ratio
TPEs	Thermoplastic elastomers

CHAPTER 1: Introduction

1.1 Background and Challenges

By transducing commonly mechanical movements into readable and high-quality electrical signals, strain sensors offer us a facile way to detect different human motions, thus showing great potential in the foreseeable future of intelligent applications, such as personal healthcare monitoring, human-machine interfaces, and smart textiles. Hence, a great many flexible strain sensors with excellent sensing performance have been successfully developed through decades of technology advancement [1-5]. The realization of high-performance and versatile strain sensors strongly depends on the rational design of materials selection and micro/nanostructural configurations. Compared with traditional electronics made from melt foils and fragile semiconductors, the using of flexible and stretchable polymer matrix notably improves their strain range and wearability, so that can be mounted onto different body positions with complicated surface curves and large-range movement (strain above 50%). Besides the high stretchability, an ideal strain sensor should also fulfill some other requirements including high sensitivity, good linearity, reliable work durability, and low hysteresis behavior [1]. Among them, sensitivity, defined as gauge factor (GF), the slope of the relative change of electrical signal, is always a chief concern, which allows for the precise detection of human motions ranging from tiny phonation vibration to large leg

joint movement. By manipulating the structures of conductive active materials and/or flexible polymers, many strain sensors with high sensitivity have been successfully prepared. For example, compared with single conductive materials, the hybrid structure with two differently dimensional micro/nano materials can endow the strain sensors a much better sensitivity because of improved distribution and reinforced connection between the conductive fillers, and the typical examples are the composites of graphene/carbon nanotubes (CNTs), MXene/CNTs, graphene/silver nanoparticles, etc. Besides, the performance improvement can also be achieved by the structuring of polymer substrate, and one of the successful strategies is to introduce patterned microstructures on polymer surface, such as the pioneering work of electric skin with pyramid-structure arrays mainly by photolithography, and sensors with various special patterns replicated from natural plants/animals (e.g., mimosa leaf, rose petal, and spider) or artifacts (e.g., silk and steel net). It is generally believed that the designed structure can greatly alter the mechanical properties of polymer substrate, resulting in increased sensitivity and faster response. In addition, recently it was reported that by applying auxetic mechanical metamaterials to increase expansion in both longitudinal and transverse directions upon stretching, a notable 24-fold improvement in sensitivity can also be achieved. Although strain sensors with enough high sensitivity have been achieved, the progress on improving other performance parameters including linearity, durability and hysteresis behavior has received very little attention. In fact, linearity, which depends on the homogeneous structure change during stretching, can be

evaluated by how constant the GF is over the testing range, and a good linearity significantly simplifies the calibration process. Durability determines the service life of strain sensors to longtime testing with stable electrical and mechanical performances. Nevertheless, due to the moduli-mismatch and weak interactions between the rigid conductive materials and the soft polymer substrates, the sensing materials are easy to detach from the polymer substrate, and finally the performance degradation of strain sensors is always unavoidable, in fact, most kinds of flexible strain sensors are reported to have a durability less than 10000 stretching/releasing cycles. As for the hysteresis, besides the inherent viscoelastic nature of used polymer substrate, the weak interaction between organic/soft polymers and inorganic/rigid nanomaterials is also responsible for the hysteresis behavior. Therefore, enhancing the adhesion between the conducting fillers and polymers is of great significance to a better performed strain sensor. Generally, most of the flexible strain sensors can be classified into two types: resistive and capacitive ones. In contrast, the resistive sensors possess high sensitivity, but poor linearity and severe hysteresis, while the capacitive ones are characterized by excellent linearity, weak hysteresis, but very low sensitivity ($GF < 1$). Therefore, it is still challenging to prepare a strain sensor which combines both high sensitivity, linearity, durability and low hysteresis.

For a qualified strain sensor, the excellent performance in sensitivity, linearity, durability etc. is of paramount significance. While for the application of strain sensor

to detect various human motions, the strain sensors should also satisfy some other crucial requirements, for instance, the strain sensors can be easily and tightly mounted to the human skin or integrated into the clothes for accurate detection of human motions. On the other hand, lightweight and small-sized characteristics should also be in consideration, so that the strain sensors will not bring additional discomfort to human. However, most reported wearable strain sensors adopt a two-dimensional (2D) planar strip structure, and the size and weight of these strain sensors are typically not small to be immediately mounted to human skin without any discomfort, while attaching such 2D planar configured strain sensors on clothes will greatly degrade the textiles' softness, breathability, wearing aesthetics and so forth. As an alternative, the development of wearable textile-based strain sensors offers a good way to satisfy the wearable comfort as well as sensing functions. Textiles, the assembly of numerous fibers, witness the evolution of human civilization. As a second skin for human, textiles can protect well human body from external interference, at the same time provide a breathable and comfortable wearing. Therefore, endowing the available textiles sensing function is considered as an easy but efficient way to accomplish the wearable sensing.

1.2 Research Objectives

This research thesis is concerned with the design, fabrication and characterization of

flexible and wearable textile-based strain sensors, with the following specific objectives:

1. To design, fabricate and characterize a new-type 1D flexible strain sensor based on a coaxial yarn architecture that offers excellent sensing performances and weavability, including high sensitivity, good stretchability, low hysteresis, linearity and long-term durability. Especially, the interfacial interaction between rigid conductive nanomaterials and flexible polymer substrate will be enhanced by introducing mussel-inspired polydopamine (PDA) as an adhesive package material, thus improving the durability and suppressing the hysteresis behavior of the strain sensor; Moreover, this new strain sensor is also lightweight and easily integrated into fabric structure by commercial textile technologies;

2. To investigate the sensing mechanism of the 1D strain sensor and important influential factors on its electro-mechanical properties. As reported, most studies simply believed the resistance change upon strain comes from the crack generation and growth on the conductive network. However, until now a detailed mechanism is still in infancy, and how the cracks develop under different strains is still unknown. Therefore, it is necessary to clarify the sensing mechanism; Moreover, the effects of prestretching and applied bending on the sensing performance of 1D yarn sensor will also be investigated in details.

3. To design, fabricate and characterize strain sensing fabric via the incorporation of the

newly-developed 1D flexible strain sensor into fabric structures by using weaving technologies. Experimental investigation on the electro-mechanical properties of the above woven strain sensing fabrics integrated with the yarn strain sensor will be investigated to study the effect of fabric structure. Moreover, the deformation behavior of the integrated 1D strain sensor within the fabric will be in-situ observed by optical microscope, and a finite element method model will be put forward to simulate the deformation process of the yarn sensor with applied strain. At last, the 1D fiber-based and 2D fabric-based strain sensors will be applied to monitor different human motions.

4. To develop highly conductive and multi-functional electronic textiles for wearable applications including bending-induced strain sensing and heater through PDA assisted deposition of silver nanoparticles on fabric substrate. As one kind carbon-based materials, graphene shows many advantages, but unfortunately with relatively higher cost and lower conductivity compared with the metals, which will result in higher driving voltage and energy waste. Thus, metal coated textiles are still required for many certain fields, such as highly conductive electrodes and efficient heater.

1.3 Research Methodologies

To solve the potential research issues, this thesis is organized using the following

methodologies:

M1. Design and fabrication of a new type 1D strain sensor with enhanced sensing performance by enhancing the adhesion between conducting fillers and polymer substrate

The commercially available, flexible polyurethane yarn (PUY), which contains a group of ten 40- μm -diameter monofilaments, was chosen as the soft polymer substrate. Meanwhile, a reduced graphene solution with a certain concentration was prepared by ultrasonication. Then the PUY was dipped into the graphene solution 6 times to obtain a layer of graphene coating, where a dilute polyvinyl alcohol solution was employed to enhance the interaction between the graphene layers and PUY during the coating. Finally, a strain sensor with a structure of graphene sheath – PUY core can be obtained. Moreover, to enhance the weak adhesion between the rigid graphene and soft PUY, the mussel inspired material, polydopamine (PDA), was selected to improve the weak interface because of its strong adhesive nature, simplicity and versatility. The adhesive PDA layer can immediately cover the surface of the as-prepared sensor by simply immersing into a dilute aqueous solution of dopamine with a pH of 8.5 for reacting 12/24 hours, in this way, the sensor is totally wrapped with a PDA protecting layer, and the sensing system will become much stable due to the adhesion support of PDA.

M2. Study of the sensing mechanism by examining the conductive layer using

scanning electron microscope (SEM) and finite element analysis (FEA) and investigation on effects of prestretching and applied bending on the sensing performance of 1D yarn sensor

For a deeper understanding of the sensing mechanism, the crack generation and growth on the conductive rGO layer of the 1D strain sensor will be thoroughly examined by SEM. In details, the morphologies of the rGO layer with applied different strains will be recorded immediately by SEM observation. Then the percentage of the cracks under different strains will be summarized and analyzed. Furthermore, based on the software of COMSOL Multiphysics and obtained SEM images, a FEA model will be put forward to study the effect of cracks on the voltage distribution. On this basis, prestretching will be applied to manipulate the rGO layer as well as the sensing performance of the yarn sensor. In addition, the electromechanical properties of the yarn sensor under different working modes including tension and bending induced strain will also be studied.

M3. Design and fabrication of strain sensing fabrics by incorporating the 1D yarn sensor using available weaving technologies

By using available weaving technologies, the above 1D strain sensor can be introduced into a fabric structure as a sensing element. The flexible 1D strain sensor will be introduced into the designed 2D sateen structure as a weft yarn in the intended positions, and the designed elastic core-spun yarns that have a similar mechanical properties as

that of the yarn strain sensor will be used as other weft yarns to provide the fabric with a strain sensing function as well as adequate stretchability in the weft direction, which can deform in line with the yarn strain sensor. The variation in the resistance of the sensing fabrics when they are stretched mainly depends on the deformation of the yarn sensing element within the fabric. In order to record the corresponding changes in the fabric geometry, particularly the yarn configuration with fabric deformation, an in-situ photography system will be set up perpendicular to the fabric plane to capture the geometry changes of the fabric and corresponding yarn deformation. The images and results obtained from photographing method will be used to analyze and describe the development of the yarn and fabric deformations. Consequently, the local deformation characteristics of the yarn sensing element with fabric extension can be identified. In addition, a prototype of fabric sensor in a bandage will be developed for human motion detection, and the strain sensing fabrics will be attached on different human body position, such as the face, arms, and legs, to testify the ability to detect different body movements, such as the chewing, elbow bending, and walking.

M4. Design and fabrication of highly conductive, waterproof and washable e-textiles for wearable strain sensor and heater

To obtain the high conductivity, Ag with excellent conductivity will be selected to deposit onto the textile substrate. In details, the silver nanoparticles (AgNPs) will be coated on widely used cotton fabric by electroless plating, where the Tollen's agent and

glucose is applied as Ag ions source and reducing agent. The bioinspired PDA will be applied to enhance the interface between AgNPs and fabric, and a highly waterproof and anticorrosive surface will be further obtained by modifying with a fluorine containing agent of *1H,1H,2H,2H*-perfluorodecanethiol (PFDT). The effects on the conductivity of the e-textiles will be studied to optimize the fabrication procedures.

M5. Characterization of materials and yarn- and fabric-based strain sensors

The sample morphologies will be tracked by the scanning electron microscope (SEM) with an accelerating voltage of 20 KV, while energy dispersive X-ray spectroscopy (EDS) will be utilized for elemental analysis. The molecular information on sample surface will be studied by Fourier transform infrared spectroscopy (FTIR), with a scanning number of 16 and resolution of 4 cm^{-1} . The thermal stability will be studied by heating the sample from $50\text{ }^{\circ}\text{C}$ to $800\text{ }^{\circ}\text{C}$ with a heating rate of $20\text{ }^{\circ}\text{C}/\text{min}$ under N_2 atmosphere using thermogravimetric analysis (TGA). The sheet resistance of the samples will be tested by a 4-point probe resistivity meter. The tensile properties of the samples will be conducted by a universal testing system.

For the electro-mechanical properties of the as-made strain sensors, the prepared sensing yarns and fabrics were tested by the combination of an Instron tester and a Keithley's Multimeter, which provides cyclic stretching and releasing, and collects the resistance signals, respectively. Moreover, different testing conditions, such as the

stretching speed, the applied strain were applied to fully investigate the sensing performance and limit of the sensing fabrics. From the measured resistance-strain curves, the sensing performances between the original 1D strain sensor and the 2D fabric sensor were analyzed in terms of sensitivity, linearity, hysteresis, response/recovery time as well as durability, so that the effects of fabric structure and fabrication process will be clarified for further improvement.

1.4 Research Significance

Due to huge potentials in the field of smart textiles, human health monitoring, and soft robotics, strain sensors are attracting intensive attentions from both industry and academia. However, there is still a lack of high-performance and reliable towards practical applications. This thesis designs and fabricates new-type 1D and 2D strain sensors, and of great importance is the greatly improved adhesion between conductive materials and the soft substrate by the introduction of bioinspired PDA, well solving the challenging stability problem of the strain sensors for practical applications.

Firstly, we developed a 1D strain sensor based on rGO and PUY by a facile method of dip-coating. Moreover, the mussel-inspired PDA was applied to encapsulate the strain sensor, with the aim of improving the adhesion between the rGO and PUY. The obtained

strain sensor presented excellent sensing performance in sensitivity, linearity, and especially the durability up to 30000 testing cycles. The simple but efficient method by PDA encapsulation in this work provides a good direction to tackle the stability issue, which can serve as a guide to fabricate other kinds of strain sensors.

Secondly the sensing mechanism of the 1D strain sensor was firstly studied in details. The SEM observations provided a direct impression on the crack development of the rGO layer. The crack information was summarized to investigate the relationship between the crack growth and resistance change under different strains. Moreover, a FEA model was put forward to simulate the effects of different cracks. This study is of significance to deeply understand the crack-based strain sensors, and the FEA model set up a bridge between the morphology change and electrical resistance change of strain sensors.

Thirdly, the obtained 1D yarn sensor was integrated into the fabric structure by commercial weaving technology. The fabric strain sensors also possess outstanding sensing performance. Moreover, the effect of fabric structure was also systematically studied, shedding light on the design and further optimization of fabric-based strain sensors. On the other hand, the fabric sensors are breathable and wearable without any discomfort, and the successful applications for detecting different human motions demonstrating the excellent capability for wearable applications. On this basis, it is expected that many other applications are promising to be fulfilled in the future, such

as for remote and personalized health care, rehabilitation, and sports and occupational wear for monitoring purposes.

Fourthly, a highly conductive e-textile was fabricated by chemical deposition of AgNPs on cotton fabric with the aid of PDA. Compared with carbon-based materials like graphene, the dense deposition of highly conductive AgNPs endows the common textiles notable conductivity, thus greatly extending the applications such as interconnects and wearable heater. Besides, the waterproof surface granted by PFDT coating also provides a guide to improve the environmental stability and anti-corrosion. This research work can promote the development of highly conductively e-textiles for multi-functional wearable applications. Furthermore, this facile and environmentally friendly method also promises the large-scale production, enabling the low-cost and wide applications of e-textiles in the future.

1.5 Outline of the Thesis

This thesis is organized as follows:

Chapter 1 briefly introduces the research background of wearable and flexible strain sensors, and the current issues in preparing high-performance strain sensors for

CHAPTER 1

practical applications. In addition, the research objectives, methodologies, significance in this thesis are described in details.

Chapter 2 reviews the recent research frontier of the strain sensors, which mainly contain the materials, classifications, structures, performance evaluations, structure design and so on.

Chapter 3 designs and fabricates the PUY based 1D strain sensor, with the rGO as conductive layer by dip-coating and PDA as encapsulation layer by solution reacting. The sensing properties of the 1D yarn-based strain sensor are systematically evaluated in terms of sensitivity, linearity, hysteresis and durability.

Chapter 4 studies the sensing mechanism by SEM and FEA. The morphologies development of the rGO layer under increasing strain are tracked by SEM, and the cracks information is abstracted and summarized. FEA is applied to simulate the effect of cracks on the electrical properties of strain sensors. Moreover, the effect of prestretching on the sensing performance of the yarn sensor is also investigated.

Chapter 5 prepares a 2D fabric strain sensor by weaving the as-made 1D yarn strain sensor into a sateen structure. The sensing performance of the fabric sensor is evaluated and compared with that of yarn sensor, and the deformation of the yarn within the fabric is examined by optical microscope and simulated by a FEA model. Moreover, a

CHAPTER 1

prototype of fabric sensor in a bandage is developed for human motion detection.

Chapter 6 is about a highly conductive e-textile, which is accomplished by chemical deposition of AgNPs on cotton fabric. The e-textiles present high conductivity and especially outstanding stability, which is able to keep stable resistance under intense ultrasonication and machine washing. The multi-functions of the e-textiles are finally demonstrated, which include bending strain sensor, conductive interconnects, and wearable heater.

Chapter 7 summarizes the whole research work and discusses the outlook of future work needed to further improve the flexible strain sensors.

CHAPTER 2. Literature Review

To get a brief understanding of flexible strain sensors, this chapter reviews the flexible strain sensors in details from five aspects: materials and classifications, sensing mechanisms, performance evaluation, structure design strategies, and fabrication technologies.

2.1 Structures and Classifications of Flexible Strain Sensors

Devices which transform mechanical deformations into readable electrical signals, can be called strain sensors. The flexible strain sensors refer to the sensors which is stretchable and able to undergo large deformation [1-5]. The flexible and wearable strain sensors are mainly made of conductive micro/nanomaterials and soft and stretchable polymer substrate, where the micro/nanomaterials act as the sensing elements, and the polymer serves as the supporting material to provide stretchability and protection for the sensing micro/nanomaterials. According to the different combination forms between the conductive fillers and polymer substrate, the strain sensors can be categorized into four kinds of structures as shown in Fig 2.1, which include C structure, CP structure, CPC structure, and PC structure, where C and P

represents the conductive filler and polymer substrate, respectively. At first, the C structure refers to the strain sensors composed by only the conductive filler, and the typical example is the carbon fibers. Generally, the C structured strain sensors possess very small stretchability less than 5%, which is believed unsuitable for large range human motion detection. Secondly, depositing a layer of conductive material on the surface of polymer substrate is a simple and common method, which can be completed by facile dip-coating, sputtering, spraying and so forth. Thirdly, the CPC structures are characterized by the uniform distribution of conductive fillers in the polymer substrate. Mixing of the two components by melting or solution dissolving is always utilized to fabricate this structure, and the proper distribution of the conductive fillers is the key point to a perfect conductive network. However, a high loading of the conductive filler is always needed to reach the percolation threshold, which will lead to the deteriorated flexibility of the strain sensors. Fourthly, to protect the conductive filler from external interference, the polymer can be used to wrap them, forming the PC structure. The PC structure can keep the high conductivity of the conductive fillers, but the preparation process like coaxial spinning and molding injection is relatively complicated. The performances of the strain sensors depend heavily on the different structures, and the varying sensing mechanisms determine how the structures should be designed and optimized.

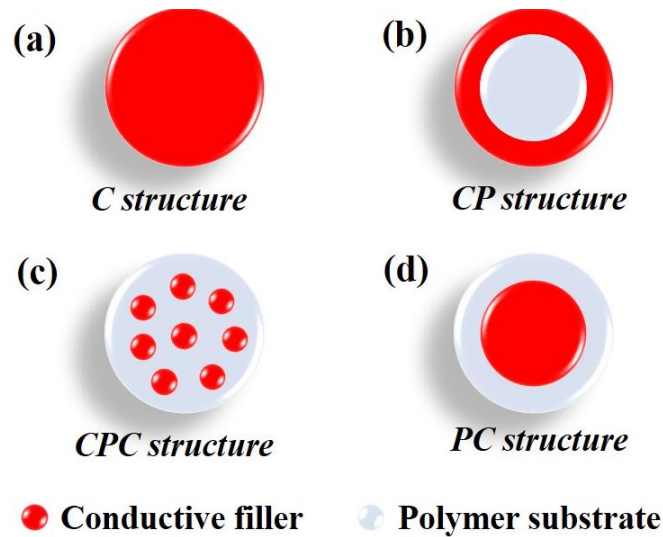


Fig 2.1 Scheme showing the four structures of strain sensors.

Among the above four structures, the CPC structure has attracted much more attention, which is very promising to be industrially prepared and practically applied in daily life mainly because of the simple fabrication process and outstanding performance. By simple metal/solution blending, the sensing micro/nanomaterials can be easily embedded into the flexible polymer matrix, and this obtained strain sensor belongs to a kind of polymer composites [6-10]. Polymer composites have been studied extensively and widely applied in our daily life over the past decades. By incorporating different fillers into the polymer matrix, the properties of the polymer can be improved and even endowed with new functions from the added fillers, such as the enhanced strength, toughness, or rigidity. If the conductive fillers are employed, one can get the well-known conductive polymer composites (CPCs), and with increasing conductive filler content to a critical value, the composites can be suddenly converted to be conductive.

This phenomenon is often named as the insulator-conductor transition [11-13]. The electrical properties of CPCs are mainly influenced by the aspect ratio and orientation of the conductive fillers, which can be studied using the theory of excluded volume. The excluded volume can be defined as the space that the center of another similar object cannot enter to ensure that these two objects will not overlap. In general, three methods, including melt blending, solution mixing and in-situ polymerization, can be employed to prepare the CPCs [11]. For the usage as a strain sensor, when stretched, the distance between the conductive fillers, such as the multi-walled carbon nanotubes (MWCNTs) and graphene in Fig 2.2, will consequently increase, which can lead to the increased distance between the fillers and destruction of the conductive paths. When the strain is small, the increment of resistance comes from the increased tunneling distance, while under large strain, the destructive conductive paths should account for the increased resistance [6-7,10,14]. As shown in Fig 2.2, the conductive fillers over a certain content, form the conductive networks, which allow the effective passage of electron. Under stretching, the distance between the MWCNTs or graphene will increase, followed by the increased tunneling resistance. With increasing strain, the tunneling effect will fail, and the destruction will occur in the conductive network, leading to the gradual reduction of conductive paths. Compared with graphene, CNTs based CPCs can stand larger strain because of the much higher aspect ratio. Furthermore, since the conductive fillers are encapsulated by the polymer matrix, it is believed that the durability of the CPCs strain sensors is prominent. However, there are few proofs

reported to support that.

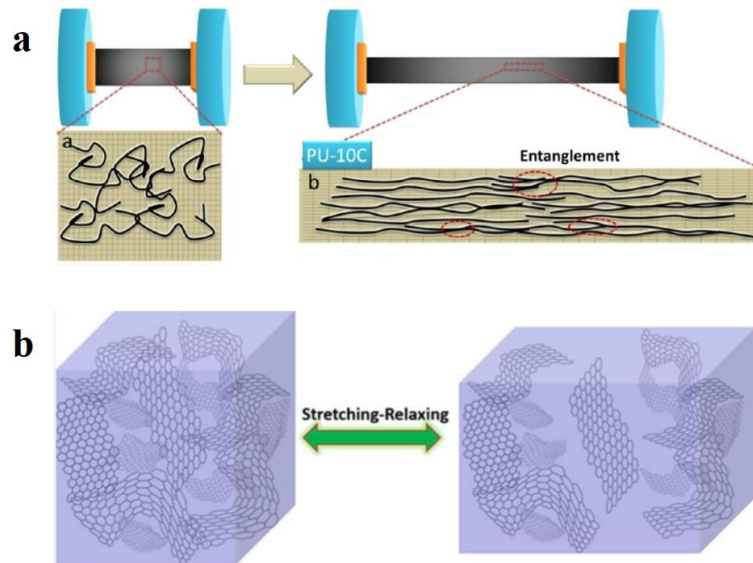


Fig 2.2 Schemes showing the deformation of conductive networks of two CPCs strain sensors: (a) MWCNT/PU [6] (b) graphene/PDMS [10].

2.1.1 Material Systems

The commonly used materials in strain sensors are briefly illustrated in Fig 2.5. To date, the reported sensing micro/nanomaterials include low-dimensional carbons (e.g., carbon blacks (CB) [6,15], CNTs (e.g. single/multi-wall CNTs (S/MWCNTs) [16-22]), and graphene [23-28]), metal nanowires or nanoparticles (e.g. Au/Ag/Cu nanowires/nanoparticles [29-32]), metal oxide (e.g. ZnO nanowires [33-34]) conductive polymers (e.g. polypyrrole (PPy) [35-36] and poly(3,4-ethylenedioxythiophene) (PEDOT) [37-39]), liquid metal (e.g. eutectic gallium indium)

[16,40], ionic liquids [41-44], and other types (e.g. MXene [45-47]). The final sensing properties of the flexible strain sensors depend heavily on the conductive micro/nanomaterials, including their geometry, dispersion, and conductivity. At first, for the mostly used carbon-based materials, CB, CNTs and graphene are characterized by the zero-dimensional (0D), one-dimensional (1D) and two-dimensional (2D) configurations, respectively. CB is a form of particles with the dimension ranges from 10^1 to 10^2 nm, and can be obtained abundantly by the combustion of heavy petroleum products. Although it is much cheaper than CNTs and graphene, the application of CBs is greatly blocked by its poor conductivity and severe aggregation. CNTs and graphene possess notable mechanical properties and excellent conductivity, thus often are used in the fabrication of flexible strain sensors. But their large-scale applications are heavily limited by the complicated, expensive, time-consuming and low-yield fabrication process, especially for the graphene. Moreover, their electrical properties are unstable and greatly influenced by many factors, such as the purity, oxidation and defects [48-50]. In contrast, metal nanowires and nanoparticles exhibit much higher conductivity. Moreover, metal nanowires, such as AgNWs, are also flexible, transparent, and able to interact with polymer substrate, while metal nanoparticles show the abilities to easily synthesize, modify with a myriad of molecular chains, and vary the geometrical size and shape, etc. With the unique combination of conventional polymers and conductive properties of metal or semiconductor, conductive polymers, polymers with highly π -conjugated polymeric chains, have aroused considerable research interest in the fields

of soft electronics, such as supercapacitors, sensors and actuators [51-53]. For the flexible strain sensors, PPy and PEDOT are the mostly used conductive polymers. These strain sensors show relatively low conductivity and sensitivity, thus need further improvement for wearable sensors application. Recently, the conductors with liquid-state, such as liquid metals and ionic liquids, have been reported to apply in stretchable strain sensors [16,23,39,42]. In particular, thanks to the special liquid state, they can deform in a limitless and instantaneous way, but unfortunately, they display severe hysteretic response because of the viscoelastic effect of polymer based fluidic channel. Moreover, the liquid conductors also require a high sealing to avoid possible leakage during the durable using, which may bring some complexity during the fabrication process.

As flexible support materials in strain sensors, the mostly used soft polymers are silicone-based elastomers, such as polydimethylsiloxane (PDMS) [22,28,30,54-55] and Ecoflex [42,56-57]. Another category includes various other rubbers [21,58-60] and thermoplastic elastomers (TPEs), and the typical one is polyurethane (PU) [7,18,31,36,61]. PDMS has been a popular flexible material for micro/nanofabrication for decades, and it displays many advantages, including stable chemical and thermal properties, good biocompatibility, notable transparency, and especially excellent elasticity. For the rubbers and TPEs, they stand out in the low-cost, high stretchability, and prominent mechanical properties, which makes them more suitable in the scalable

production of cheap strain sensors. In fact, stemming from the long chain structure the flexible polymers have the unavoidable shortage of inherent viscoelastic behavior, which will lead to the sensing hysteresis for the strain sensor especially after long-term using. Besides that, it is believed that flexible polymer types have little influence on the sensitivity of strain sensors. Recently, hydrogels have attracted many research attentions because of their ability of self-healing [44-45,62-64]. The ability of self-healing can increase the durability of strain sensors and extend their service life. Thus, it is desirable to incorporate the sensing micro/nanomaterials into the self-healing hydrogels. Until now the main challenges are from the poor stability, sensitivity, and partly the low healing efficiency.

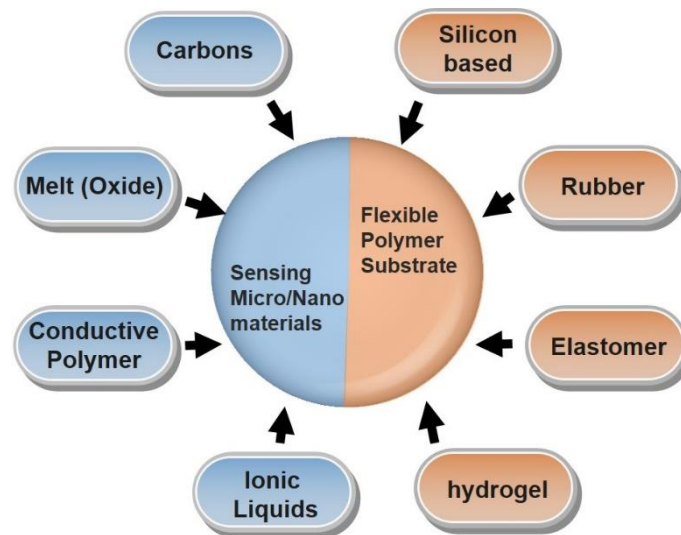


Fig 2.5 The composition of flexible strain sensors: the sensing micro/nanomaterials and flexible polymer substrate

2.1.2 Classifications

Strain sensors can be classified into different categories according to different standards. In general, on the basis of sensing mechanism, there are two main types: the resistive-type [26,30-31,46,54,57,61] and capacitive-type [16-17,22,41,55,65]. Fig 2.4A, B shows examples of a typical resistive-type and capacitive-type strain sensor, respectively. When stretched, the resistive-type strain sensor generates resistance change as a function of the applied strain because of the occurrence of cracks in the conductive network, and after fully release of the applied strain, the cracks disappear and the strain sensor can restore to its original state as well as the recovery of the resistance. For the capacitive-type, two conductive electrodes with a dielectric elastomer layer sandwiched in between form a parallel-plate capacitor, and upon stretching, the thickness of the dielectric layer will decrease, causing the increase of capacitance. Within a certain strain range, where there is no variation of Poisson's ratio, the capacitance (C) can be calculated as equation (1):

$$C = (1+\varepsilon) C_0 \quad (1)$$

where ε and C_0 represents the in-planar strain and initial capacitance, respectively. Besides these two main types, there are still some other types of strain sensor. Among them, the triboelectric nanogenerator (TENG) based sensor stands out because unique self-power ability, which can collect energy from surrounding environment or various

human motions [66-70]. The working mechanism of TENG lies in the triboelectric effect and electrostatic induction. Fig 2.4C displays a TENG based sensor and the corresponding working mechanism [66]. The TENG is composed by the electrospinning TPU and AgNWs/rGO layers, which function as triboelectric and protection layer as well as conductive electrodes, respectively. When attached on human skin, the skin will act as the positive triboelectrification layer, while the TPU will serve as negative triboelectrification layer, thus positive and negative charges will be generated on the surface of human skin and TPU. The cyclic contacting and separation between the TPU and human skin by human motion will induce charge flowing in the external circuit, finally accomplishing the transformation from the mechanical energy to electricity. As for the sensitivity, the different external deformation will result in the different contacting area between the TPU mats and human skin, leading to the varying charge and open-circuit voltage. Nevertheless, the TENG has much complex fabrication process and structure. Moreover, for the capacitive-type strain sensor, the gauge factor ($GF = (\Delta C / C_0) / \epsilon = ((1 + \epsilon)C_0 - C_0) / \epsilon C_0 = 1$) is theoretically limited to 1 [1], making it hard to detect small strain or vibration. In contrast, the resistive-type strain sensors are easier to fabricate and apply in daily life with low-cost and high working performance, hence this literature review mainly focuses on the resistive-type flexible strain sensors.

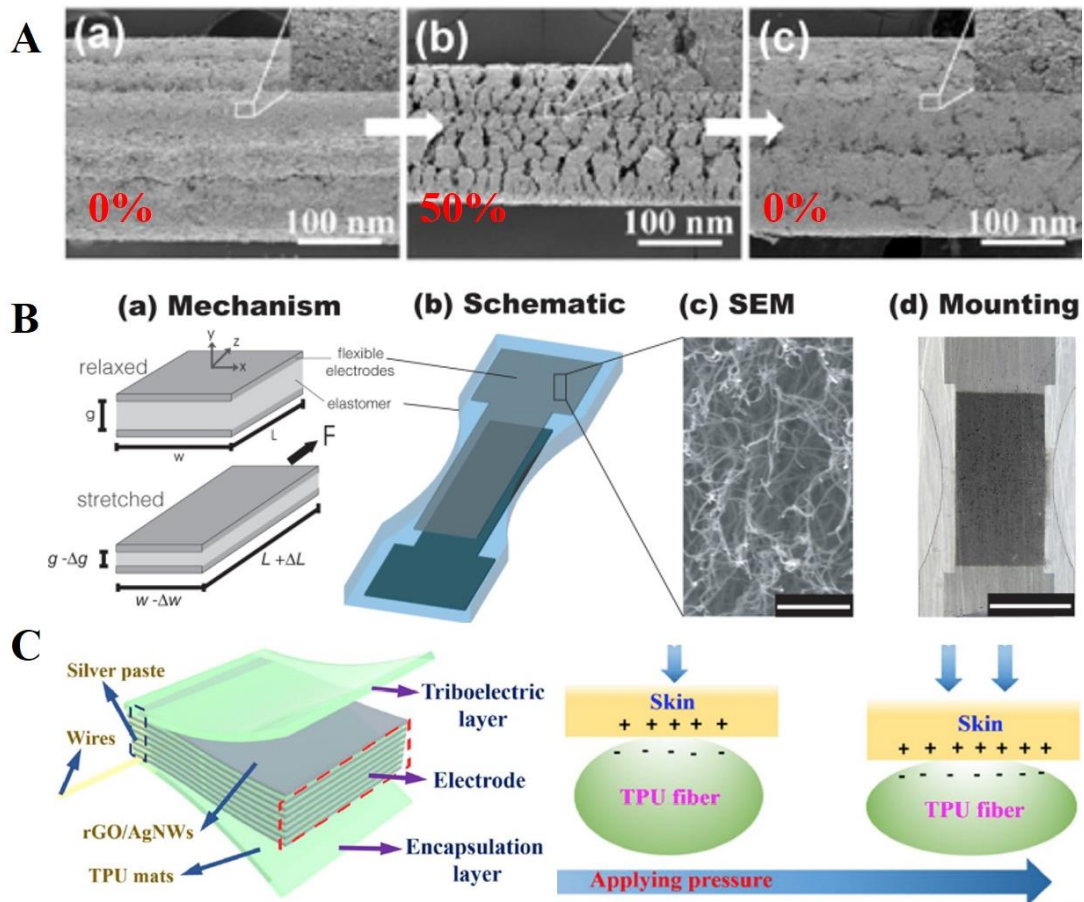


Fig 2.4 (A) The deformation of graphene network under strain of 50% of a typical graphene/PU yarn resistive-type strain sensor [31]; (B) Sensing mechanism, sample schematic, SEM image of CNT networks in the electrode, and sample mounting scheme of a typical capacitive-type strain sensor [65]. (C) Scheme showing the structure and working mechanism of a TENG based sensor [66].

Fig 2.5 shows some examples of 1D fiber/yarn, 2D film, and three-dimensional (3D) foam strain sensors. The 1D strain sensors are continuous and lightweight, and they can be fabricated by available wet spinning (Fig 2.5a), which greatly lowers the cost and facilitates the scalable production [19]. In addition, one can immediately use the

commercially available yarn, just as shown in Fig 2.5b, where the strain sensor is prepared by dip coating the PU yarn into the graphene solutions [31,61]. The easy accessibility of the materials and facile solution-based fabrication process much prefer the continuous and scalable preparation. Moreover, the 1D strain sensor is infinitely long in theory, therefore, they can be cut and deformed as required and applied in different fields. Besides that, it is believed that the 1D flexible strain sensors display advantages in some other aspects: firstly, they are flexible enough to deform under small strain, and can be stretched, bent or twisted, which makes them can detect various human motion; secondly, they own large specific surface areas and good breathability for the comfortable wearing [71]; thirdly, the 1D strain sensors can be easily integrated into various textile structures to fabricate 2D fabric-based strain sensor and wearable sensing clothing. As shown in Fig 2.5c, the 2D strain sensors always adopt a film or planar shape, and in fact, they are more suitable for pressure detecting instead of axial strain detecting [22,53,55]. Moreover, when attached on the skin, the relatively large area will influence the breathability by hindering the evaporation of sweat and passage of fresh air. Upon stretching or bending, the 2D strain sensor may also separate from the skin because of the positive Poisson's ratio, which makes them unfit for long-term using. As for the flexible strain sensors with 3D structure, the mostly common one is the foam [10,72-74]. Fig 2.5d is about an auxetic PU foam strain sensor, and the foam structure presents a re-entrant instead of the commonly honeycomb. Compared with the 1D and 2D strain sensors, the 3D strain sensors are advantageous to be prepared in any

shapes [72], hence different kinds of deformation, such as stretching, blending and shearing, can be well detected. Additionally, due to the porous structure, the foam strain sensor can also act as a safeguard by absorbing the energy from external impact or hurt.

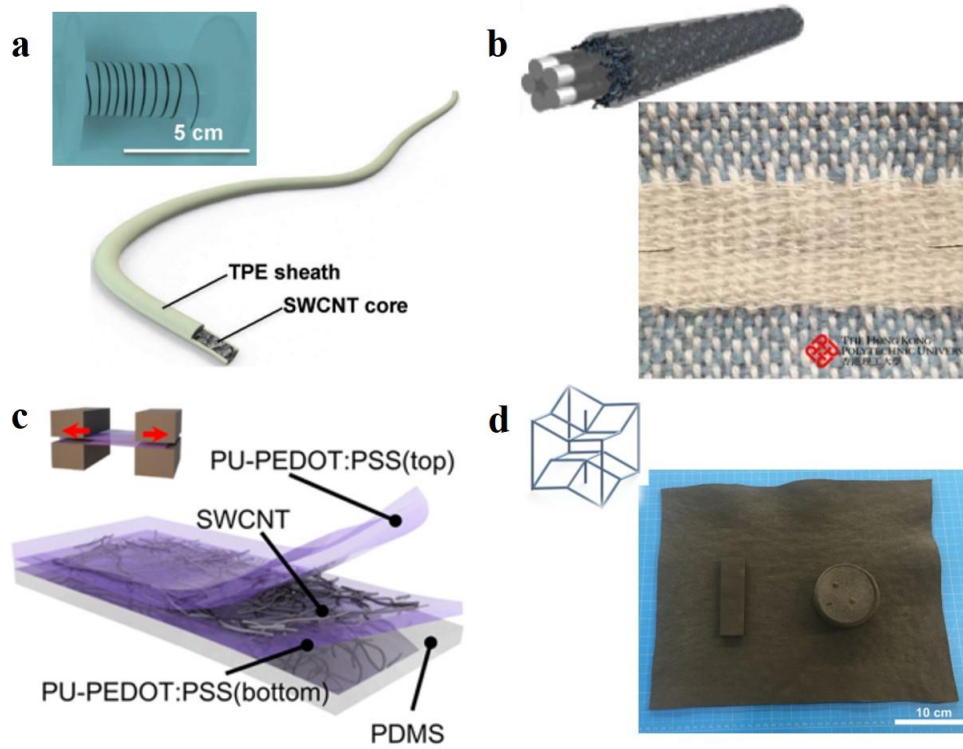


Fig 2.5 (a) 1D strain sensor of coaxial TPE-wrapped SWCNT fibers [19]; (b) 1D strain sensor of graphene/PU yarn composites [31,61]; (c) 2D strain sensor of three-layer stacked PU-PEDOT:PSS/SWCNT/PU-PEDOT:PSS on a PDMS substrate [53]; and (d) 3D strain sensor of CNT/PU auxetic foam [72].

2.2 Sensing Mechanisms of Strain Sensors

The strain sensors can detect external strain under several mechanisms, and the sensing mechanisms depend heavily on the used sensing micro/nanomaterials, assembly structures, and preparation process. In general, the mechanisms come from two parts: one is the resistance change of the materials themselves, and the other one is the interaction between the sensing fillers. For the first part, there are two types, i.e., the geometrical effect and piezoresistivity. The resistance of a conductor can be calculated by equation (2) [1]

$$R = \frac{\rho L}{A} \quad (2)$$

Where ρ , L and A represents the electrical resistivity, length and area of cross-section. When stretched, the L increases, but A shrinks, leading to the increased R . Piezoresistivity refers to the resistance change of materials caused by the change of the bandgap on inter-atomic spacing [75-76]. Although strain sensors based on mechanisms of geometrical effect and piezoresistivity can show high sensitivity, but the rigid properties and low strain detecting range ($\leq 5\%$) [77] greatly limit their application in human motion detection, which demands a large strain ($\geq 50\%$) [78] to match with the movement of human skin.

For the latter one, the resistance change comes from the distance change between the

sensing micro/nanomaterials, which can be termed as tunneling effect, disconnection, and crack origination and propagation. Firstly, tunneling is the crossing of electrons through a nonconductive barrier between two closed spaced adjacent micro/nanomaterials as shown in Fig 2.6A [20]. Under stretching, the entangled micro/nanomaterials, such as the CNTs and AgNWs, will unfold, thus causing the change of tunneling resistance. The effective tunneling space mainly rests with the types of conductive micro/nanomaterials and polymer substrates, and it is demonstrated that this effect works for the CPCs based strain sensor [14,59-60,79-80]. According to the tunneling theory developed by Simmons, the resistance R of the CPC can be expressed by equations (3) and (4):

$$R = \left(\frac{L}{N}\right) \left(\frac{8\pi h s}{3\gamma a^2 e^2}\right) \exp(\gamma s) \quad (3)$$

$$\gamma = \frac{4\pi}{h} \sqrt{2m\phi} \quad (4)$$

where L refers to the particles number in a single conducting path, N of conducting paths number, h of the Planck constant, s of the smallest distance between conductive particles, m of the electron mass, ϕ of the potential barrier height between adjacent particles, a^2 of the cross-sectional area, and e of the electron charge, respectively. When applied with external strain of ε , the distance between the conductive particles will increase from initial s_0 to s , leading to the increased resistance change from initial resistance (R_0) to resistance at strain of ε (R). At the same time, the conductive paths will also present a change from initial number (N_0) to number at strain of ε (N). The

relationship between the s , N , and R with ε can be expressed by using equations (5)-(7):

$$s = s_0(1+b\varepsilon) \quad (5)$$

$$N = \frac{N_0}{\exp[A\varepsilon+B]} \quad (6)$$

$$\frac{\Delta R}{R_0} = \frac{R-R_0}{R_0} = \left(\frac{Ns}{N_0s_0}\right) \exp[\gamma(s - s_0)] - 1 \quad (7)$$

Where in equation (6), A and B are constants. With the substitution of equations (5) and (6) into equation (7), one can obtain the equation (8) concerning the relationship between relative resistance change with ε .

$$\frac{\Delta R}{R_0} = (1 + \varepsilon) \exp[(A + \gamma s)\varepsilon + C] \quad (8)$$

As for strain sensors based on disconnection mechanism, the conductive micro/nanomaterials connect with each other to form a continuous path for electrons, and stretching can cause the slippage between the micro/nanomaterials, thus the increased resistance. Just as shown in Fig 2.6B, upon stretching, the AgNWs will disconnect with each other, and less conductive paths will be reserved [30]. Thirdly, similar to the disconnection mechanism, for some flexible strain sensors, the sensing micro/nanomaterials are assembled in the form of thin layer. When the strain is small, the conductive materials will side and disconnect with each other. With further increasing strain, due to the rigid nature of the sensing micro/nanomaterials, cracks will occur and propagate in the conductive layer, leading to the drastically increased resistance. Fig 2.6C displays the in-situ tracking of cracks development under strains

from 0% to 80%, where there appear some minor cracks under the small strain of 5%, and cracks keep growing gradually with the increasing strain. Hence the cracks induced by the stretching decreased the conductive pathways and cause the greatly increased resistance. After stress releasing, it is obvious that the conductive layer recovers to its original state, only leaving some scattered cracks [46]. Since the cracks propagation can allow the large deformation of conductive networks while the materials still remain conductive, the mechanism of cracks origination and propagation have been employed to develop a myriad of flexible strain sensors, which can work efficiently under large strains, thus especially suitable for the detection of various human motions.

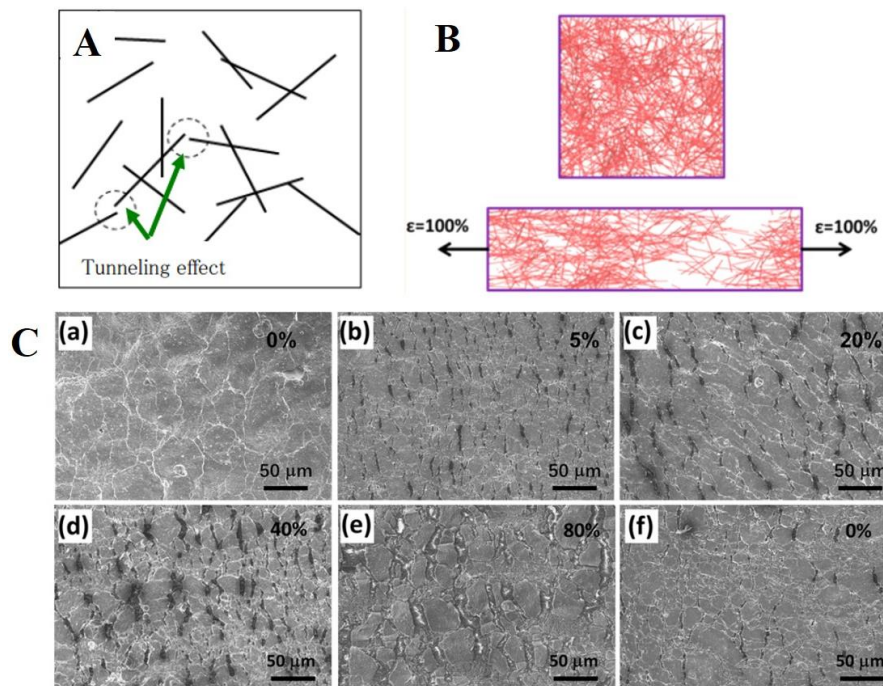


Fig 2.6 Scheme showing (A) the tunneling effect in the CPC [20] and (B) the deformation of AgNWs in the strain sensor of AgNWs/PDMS [30]; (C) the crack propagation for the MXene/CNTs/PDMS strain sensor [46].

2.3 Performances Evaluation of Strain Sensors

The performance of flexible strain sensor on human motion monitoring and other applications could be evaluated by different performance parameters, for instance, stretchability, sensitivity, linearity, hysteresis, and durability [1-3]. Besides that, in practical using, some other features are also of great importance, such as self-healing, self-powering, non-toxicity, multifunction and so forth.

2.3.1 Stretchability

Stretchability indicates the ability of a substance that can withstand extending to a certain length without permanent deformation. Stretchability of strain sensors depends on the type of material that fabricate the strain sensor. Traditional strain sensors (metal & semiconductor) usually possess low stretchability due to the rigidity of the material. To address this hurdle, many studies have devoted their effort to achieve high stretchability and sensitivity in a strain sensor. As suggested by Rogers et al [81-82], two methodologies are often employed to obtain a high stretchability, namely, “materials that stretch” and “structures that stretch”. For the materials, it is known that the strain sensors are mainly composed with the sensing micro/nanomaterials and flexible polymer substrate. Compared with the rigid sensing micro/nanomaterials, such

as CNTs, graphene, and metal nanowires, the selection of a flexible and stretchable polymer could be a facile and preferred option, and the commonly used polymers include PDMS, PU, natural rubber, and gel. Moreover, it is believed that 1D micro/nanomaterials is beneficial for the stretchability improvement, because their high aspect ratio can facilitate the formation of conductive networks and the networks can keep stable even under high strain levels. In contrast, due to the much lower aspect ratio, other conductive materials, such as graphene, CBs, and metal nanoparticles, cannot form a robust conductive network easily and the formed networks can break under a small strain. On the other hand, by proper structure design, a higher stretchability can be obtained, for example, by designing the unique open-mesh geometries (Fig 2.7a), wherein the strain sensor made of aligned SWCNTs can break into gaps and islands, but bridged by bundles. This mechanism endows the SWCNTs strain sensor a much higher work range of 280% [83]. Another example is the wrinkled CNT film strain sensor in Fig 2.7b, the wrinkled CNT networks are capable of measuring an ultrahigh strain of 750% with high sensitivity [84]. Other structures include wavy geometry [85-86], helical structure [87] etc.

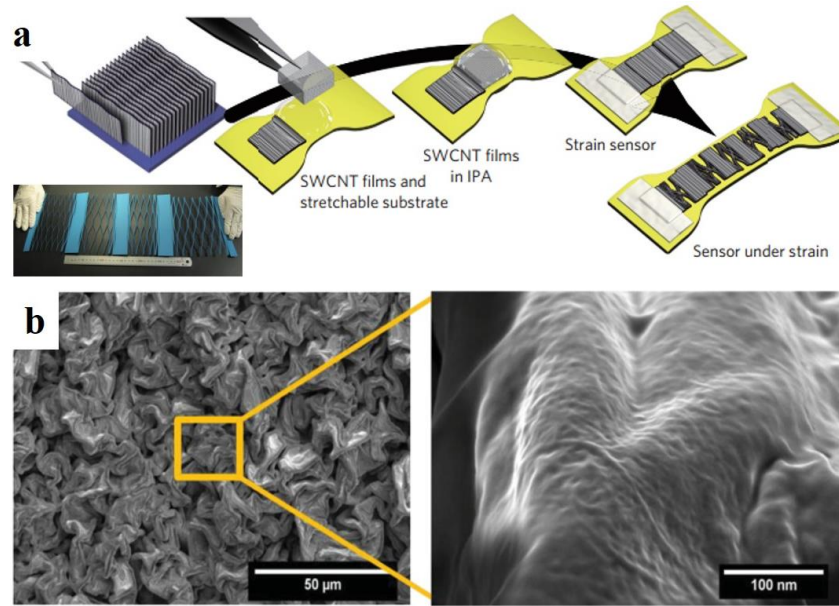


Fig 2.7 (a) Scheme showing the fabrication procedures of SWCNT strain sensor with open-mesh geometries [83], and (b) wrinkled CNT thin film on Ecoflex substrate [84].

2.3.2 Sensitivity

Sensitivity refers to the degree of responsiveness to internal and external changes. Sensitivity of a strain sensor is represented by GF, where the ratio of the changes in relative electrical resistance to the applied tensile strain. It can be calculated by the following equation (9):

$$GF = \frac{\Delta R/R_0}{\varepsilon} \quad (9)$$

Where R_0 refers to the initial resistance, ΔR represents the change between R_0 and the final resistance (R_f) when applied with a certain strain (ε). According to the equation,

the larger the change in resistance and lower the initial resistance, the more sensitive the yarn is under the same applied strain. For traditional metal-foil based strain sensor, the GF maintains at 2-5, which is incompetent to be utilized for a practical and wearable strain sensor. In contrast, the sensitivity of the flexible strain sensor can be manipulated to a very high degree. The sensitivity varies in a wide range, depending on the mechanisms, micro/nanomaterials, and structures of the strain sensor. In general, due to theoretical limitations, the capacitive strain sensors display a very small GF (≤ 1) [16-17,41,65,88]. Therefore, the resistive type strain sensor is much superior to the capacitive one. For the flexible resistive type strain sensor, the sensitivity mainly depends on the conductive micro/nanomaterials, such as the fabrication methods, concentrations, and assembly structure. For example, it is found that the concentration of graphene and number of coatings on the sensors could make a huge influence on the sensitivity of a yarn-based graphene/PU strain sensor [61], and higher concentration of graphene and less amount of coatings contribute to a higher sensitivity (Fig 2.8a). Moreover, compared with the single conductive micro/nanomaterial, the hybrid structure with two different shaped conductive materials can greatly improve the sensitivity. For example, Cai and coworkers [46] demonstrated the strain sensor based on $\text{Ti}_3\text{C}_2\text{T}_x$ MXene/CNT composites could exhibit high stretchability (up to 130%) and high sensitivity (GF = 772.6), and with excellent reliability and stability. (Fig 2.8b). Moreover, the sensitivity can also be enhanced by manipulating the structure of polymer substrate, such as the spider-inspired crack sensor [89-90] in Fig 2.8c and

patterned structure in Fig 2.8d, and it is reported that the GF can be increased to an unprecedented level of 150000 [91].

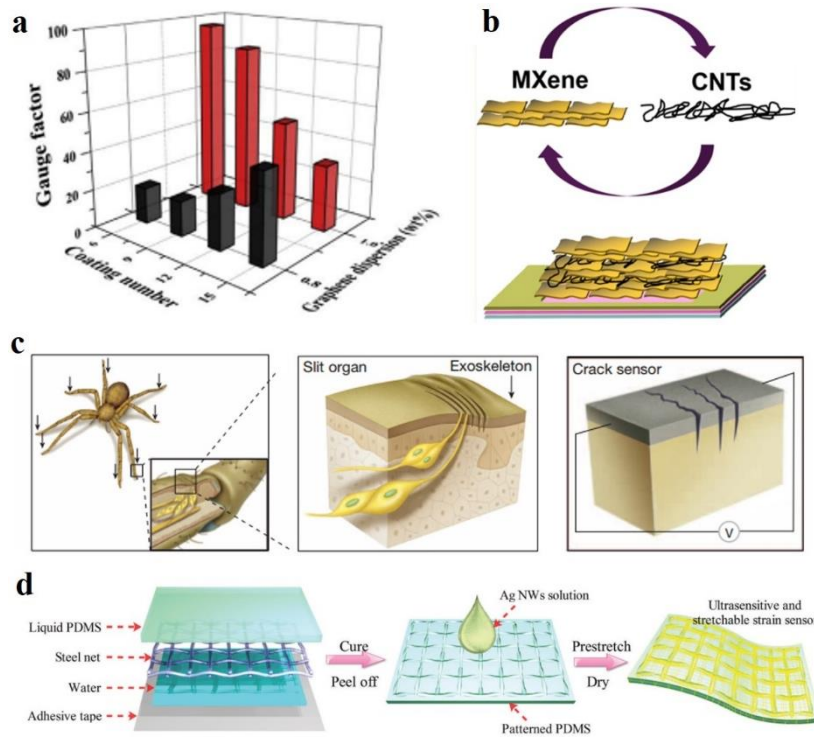


Fig 2.8 (a) Effects of graphene concentration and number of coatings on the GF of yarn based strain sensor [61], (b) strain sensor with a sandwich-like $Ti_3C_2T_x$ MXene/CNT layer [46]; (c) spider-inspired crack sensor [89]; and (d) fabrication procedures for an ultrasensitive strain sensor by the aid a steel net [91].

2.3.3 Linearity

Linearity is the property of a relationship which can be represented as a straight line. Linearity is used to determine whether the transfer function of a sensor can be approximated by using a straight line. The accuracy of device signals can be evaluated

with the correlation coefficient, that is, by measuring the slope of the straight line. As the greater the correlation coefficient of the sensor, the better the linearity sensor shows, and the easier for the calibration process. As shown in Fig 2.9, although limited by the low sensitivity, the capacitive strain sensors are typically characterized by the high linearity (a correlation coefficient of 0.99) [16-17,41,65,92-93]. However, majority of the resistive strain sensors exhibit linearity at low strains, but nonlinearity at high strain, which comes from the nonhomogeneous deformation of the conductive network [1,21,46,57,61,91,94]. Some methods are proved to greatly improve the linearity, for instance, introducing Ag nanoparticles to graphene to form a hybrid structure [31], and the polydopamine (PDA) encapsulation [95]. In brief summary, the high sensitivity requires the large deformation of conductive networks upon stretching, while a stable and homogenous deformation is essential for the high linearity, hence a trade-off between the sensitivity and linearity is of great importance during the structure design of flexible strain sensors.

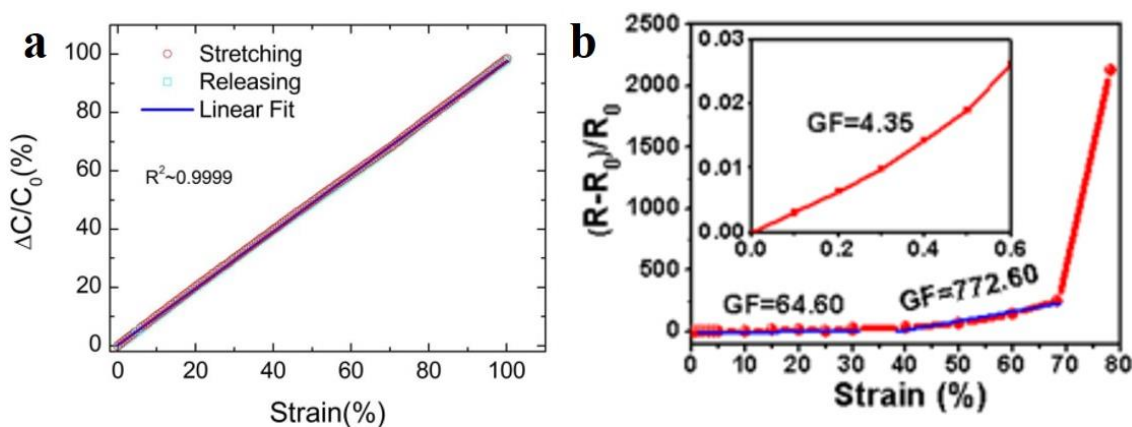


Fig 2.9 Electrical signal development upon stretching for (a) capacitive [17] and (b)

resistive [46] strain sensors, respectively.

2.3.4 Hysteresis

Hysteresis is a retardation of the effect when the forces acting upon a body are changed. A good performance in hysteresis becomes much important especially under long-term using, because the sensing properties will not restore to its original state due to severe hysteresis, which will lead to the uncertainty, weakening and longer response time of the strain sensor. The hysteresis can be evaluated by hysteresis error (δh) as following [61,96]:

$$\delta h = \frac{\Delta R_{max \text{ difference}}}{\Delta R} \times 100\% \quad (10)$$

Where $\Delta R_{max \text{ difference}}$, ΔR refers to the maximum difference between resistances as decided by the stretching and releasing stages, and the whole resistance change, respectively. In fact, it is generally believed that hysteresis is mainly caused by the viscoelastic nature of polymers [1], as internal stress of viscoelastic material tends to decrease over time and it cannot be completely recovered after releasing it from strain. One way to improve the hysteresis is the structuring design of flexible polymer substrate [54-55], for it is proven that the sensor will have enhanced mechanical properties, followed by higher sensitivity and faster response time than the unstructured one. When applied with external strain, the microstructured polymer substrate can

elastically deform, which will store and release the energy reversibly to minimize the inherent visco-elastic behavior. For example, as reported by Bao et al [55], the pyramid-structured PDMS films can relax on the millisecond timescale, and but as long as 10 s for the unstructured ones. Furthermore, the interaction between the conductive materials and the soft polymers also plays an important role [6,73], especially for the CPCs, where the conductive materials are embedded inside polymer substrate. If the interaction is strong, during releasing the conductive materials will rapidly return to their original positions with the aid of elastic polymer.

2.3.5 Durability

Durability is especially important for the practical application of flexible strain sensors, but unfortunately have not received enough attention by the academia. In daily using for human motion detection, the strain sensors will undergo large, complex, and varying strains. Besides that, the environment, including the temperature, moisture, sweat and external friction, also has profound influence on the sensing properties of the strain sensor [80,97-99]. In general, the strain sensor can fail mainly in two ways: the fatigue and plastic deformation of soft polymer substrate, and the fracture of the sensing materials. To protect the sensing materials from outside effects, the sensing materials can be encapsulated in a flexible polymer layer, and the flexible PDMS is the most popular option because of its excellent elasticity, transparency, formability and biocompatibility. With the outer protective layer, the durability of strain sensor for

dynamic stretching/releasing testing can be notably improved [31,100-101]. However, in most reported results, the durability for continuous testing stays in the level of 10^2 - 10^3 times, although some strain sensors can reach a relatively high level of 10^4 - 10^6 times [23,102-104].

2.3.6 Safety and wearing comfort

As wearable strain sensor will be mounted directly on human skin for continued motion monitoring, the using of various sensing micro/nanomaterials should be safe to human biological system [29,105-108], such as the mostly used carbon-based materials of graphene and CNTs. Because of the superior mechanical and electrical properties resulted from the unique structure, graphene and CNTs have received substantial attention among other nanoscale carbon materials for the fabrication of strain sensor. Despite the uncertain toxicity from conflicting test results, they will inevitably expose to human beings in the increasing demand of wearable electronics. Moreover, when the micro/nanomaterials are released to the environment, toxicity may be accumulated and travel up food chains, thus threatening both the health of human beings and ecosystem. In order to minimize any poisonous or inflammatory responses, studies have been conducted for evaluating possible factors that influence the toxicity. Taking the CNTs as a typical example, it is reported that impurities is one of the most crucial factors contributing to the toxicity of CNTs [106-107]. Although purification is believed to be an effective way for the improvement of CNTs biocompatibility, it is unfeasible to clear

the impurities completely while keeping the intact structure of CNTs. In addition, SWNTs have shown higher toxicity than MWNTs, which is associated with the different size, diameter and layer number. Since there are various factors affecting CNTs toxicity, a standard prototype is necessary for accurate and reliable toxicity analysis. Otherwise, the potential application of CNTs for wearable strain sensors will be greatly limited.

As for the wearable application of strain sensors, wearing comfort is another critical factor to be addressed. In particular, small-sized and lightweight strain sensors are preferred, since air permeability and ventilation will be better for perspiration. If the strain sensors are in large size, it will be difficult for sweat and air to pass through human body freely, which may also cause discomfort in wearing. Therefore, compared with the common 2D/3D strain sensors, the 1D configuration is superior in lightweight, scaled size and wearing comfort. Furthermore, the contours of the human skin are really complex with varying curvatures, especially in the head, ankle and elbow. Hence it is important to take the outer shape of certain human skin into consideration during the design of strain sensors, so that the strain sensor can keep tight contact with the human skin, thus make sure the precise detection of human motion, as well as the comfortable wearing. However, most polymer materials have a positive Poisson's ratio[109-110]. It is unavoidable that the strain sensor will detach from the skin under bending. To solve the problems, an auxetic structure can be employed, which will be described in details

hereinafter. Taking comfortable wearing into consideration, wearable electronics should be flexible and soft enough for the accommodation with body motion. Otherwise, the user will feel uncomfortable for monitoring health in the long run.

2.4 Structure Design Strategies Towards Desired Strain Sensors

To obtain a desired strain sensor, some methodologies can be applied to improve the sensing performance of strain sensor, so that the flexible strain sensors can be applied successfully in different fields with effective motion detecting and stable working durability. This part will briefly introduce some commonly strategies for strain sensors design. Since the strain sensors mainly involve two parts: the soft polymer substrate and conductive sensing micro/nanomaterials, the design strategy for the polymer substrate, i.e., the patterned and auxetic structure, will be clarified firstly, and then the second part is about the manipulation about the conductive network by using hybrid conductive fillers and prestretching. Moreover, the special function of self-cleaning capability is also be briefly introduced.

2.4.1 Patterned structure

Introducing some unique surface pattern on the polymer substrate is considered to be another efficient methodology to enhance the deformation of flexible polymer, followed by increased resistance and sensitivity. The mechanism lies in the magnified deformation induced by strain concentration. In general, the pattern design is often applied in the 2D plantar strain sensor because of its easy operability. Most of this featured 2D strain sensors can also be named as electronic skins. In recent years, the design of flexible and skin-attachable electronic skins has become a research hot. Electronic skins are considered as capable of detecting subtle pressure changes with high sensitivity and rapid response, thus showing huge potential application in wearable electronics, healthcare monitor, and biomedical devices [22,54,78,111-114]. Hereinafter, some examples regarding on the electronic skins with special surface patterns will be given and elucidated. By replicating from a silicon master and followed by a Pt deposition process, Pang et al reported a highly sensitive sensor, which could detect different deformation, including pressure, shear and torsion [112]. The structure of their sensor was characterized by two interlocked arrays of high-aspect-ratio Pt-coated nanofibers, just as shown in Fig 2.10a. When applied with different external stimuli, the connection between the nanofibers will change, leading to the change of electrical resistance. Using a simple solution-based hydrothermal method, Ha et al fabricated micropillar arrays coated with ZnO nanowires as shown in Fig 2.10b [113]. With this

unique interlocked hierarchical structures, the contact area between the ZnO nanowires will change and also the nanowires will bend under external pressure, endowing the electronic skin a high sensitivity, low detection limit, and ultrafast response time. Similar to the nanofillar and pillar architectures, electronic skins with microdome arrays were further prepared as shown in Fig 2.10c [114]. This special structure can be achieved by casting a viscous solution containing CNTs and PDMS onto a silicon micromold or using monodispersed polystyrene microsphere as sacrificial template. Fig 2.10d depicts a microprism-structured strain sensor, which was prepared by a combined process of AgNWs and soft-lithographic replication [115]. Since strain will concentrate in the valley regions during stretching, the deformation of the conductive AgNWs network will be greatly enhanced, thus showing notably improved sensitivity. In fact, the special structure design of polymer substrate film is the most important element of electronic skins, which will exhibit much better performance than the unstructured ones.

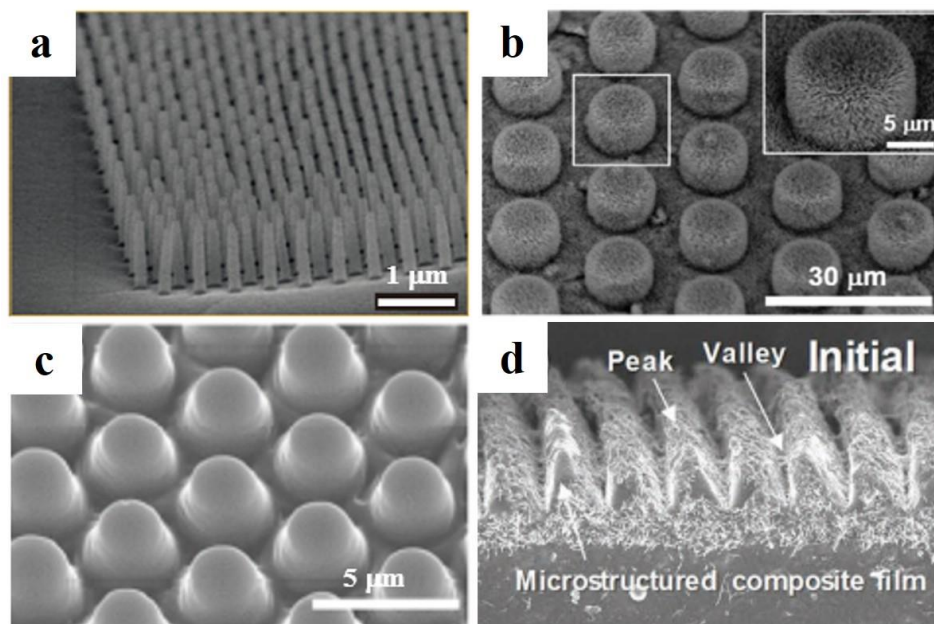


Fig 2.10 (a) SEM image of a dense array of 50-nm radius Pt coated nanohairs [112]; (b) SEM image of ZnO nanowires on the PDMS micropillars [113]; (c) SEM image of a composite film with microdome arrays [114]; (d) SEM images of AgNWs/PDMS film strain sensor with a densely packed microprism-array architecture [115].

To obtain a patterned structure, some materials with special surface structure can also be immediately utilized as template for simplicity. For example, using a steel net as template (Fig 2.11A), PDMS was coated onto the template to replicate the pattern after thermally curing. Followed by the coating of conductive AgNWs, one can fabricate the ultrasensitive strain sensor [91]. Compared with the common flat PDMS film, the pattern endows the strain sensor a greatly increased sensitivity, with four orders of magnitude for GF value. Similarly Zhang et al found that the silk textile possesses microstructured surface, which can be used as effective moulds to construct a patterned film (Fig 2.11B) [54]. The liquid PDMS base and cross-linker was mixed and coated onto the silk surface. After solidifying and peeling off, one can get a flexible PDMS film with the same surface pattern of the silk used. The sensing performance tests have proved that the formed pattern greatly improved the sensitivity of the strain sensors to be competent to detect very subtle movement, such as the weight of an ant and bee. Compared with other methods, the direct use of existing materials in our daily life, such as the steel net and silk textiles, is much cost-effective and easier.

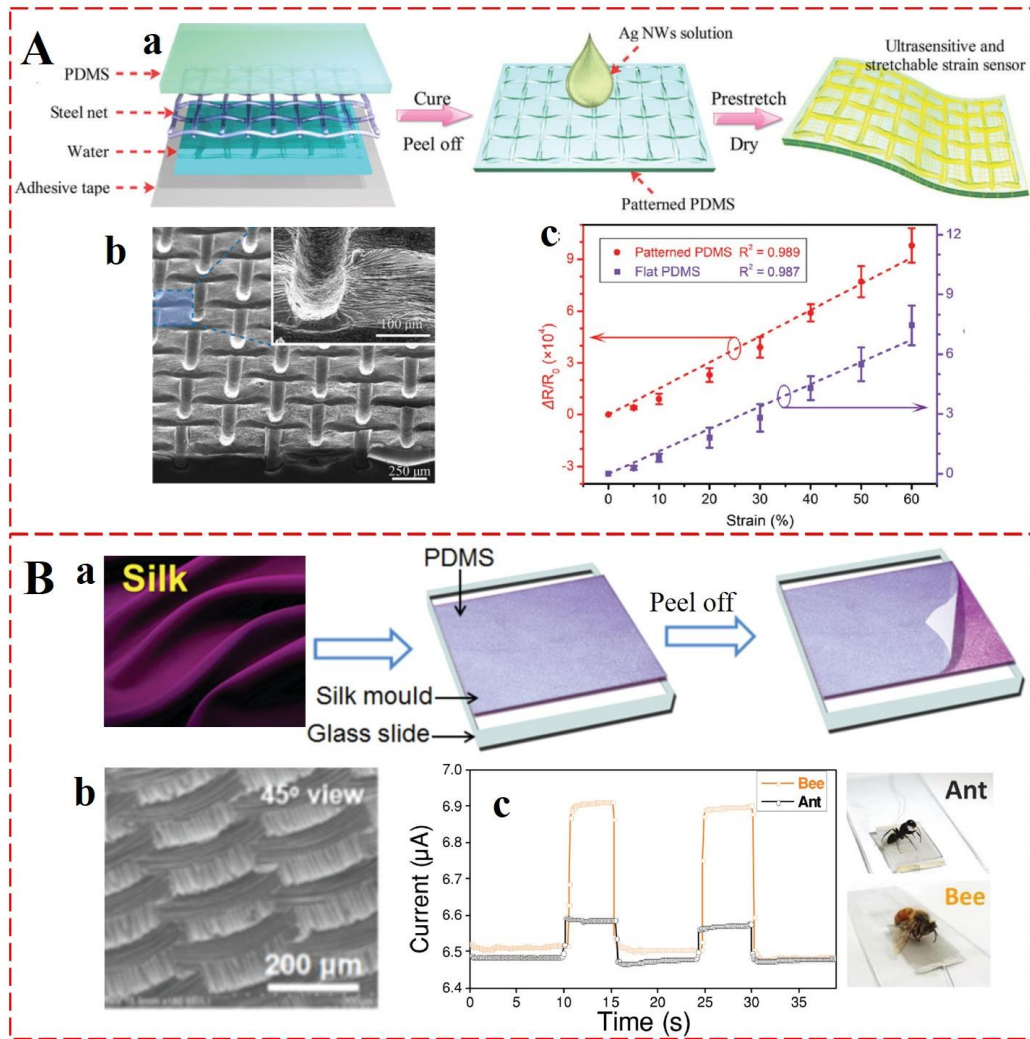


Fig 2.11 Schematic illustration of the fabrication process of (A) AgNWs/PDMS strain sensor moulded by steel net [91]; and (B) SWCNTs/PDMS strain sensor moulded by silk [54].

In contrast, the small size of 1D strain sensors make it much harder to design certain pattern on the circular surfaces. Ideally, with a patterned or uneven surface, the strain distribution will not be uniform, and the accumulation of strain at certain positions will generate much enlarged cracks on the conductive layer, followed by greatly increased sensitivity. To this end, Liu et al utilized the natural phenomenon of Plateau-Rayleigh

instability to form regular microbeads on the PDMS fibers as shown in Fig 2.12a [116]. The PDMS fibers were firstly prepared by tracting and immersing the PDMS precursor into hot oil bath. Due to the high temperature, the thermal curing of PDMS can be completed in several seconds. Secondly, the PDMS microbeads can automatically form once the viscous PDMS liquid flows along the as-made vertically aligned fibers. With this special structure, when applied with strain, the gold layer deposited on the surface displays different crack morphologies on different positions, where strain concentrates obviously between the adjacent microbeads, thus forming much denser and bigger cracks. More recently, Choi et al reported the preparation of a hierarchical microhairy conductive fiber [117]. As shown in Fig 2.12b, the Ag coated conductive fiber was firstly fabricated by chemical deposition of AgNPs on the PU fiber, and then the compounds with mixture of PU, CB and AgNWs were further coated and patterned using a beforehand molds, which own microscale cylinder-shaped surfaces on top and bottom, finally obtaining the microhairy conductive fibers. The unique fibers can not only function alone as strain sensor to repond axial stretching as high as 200%, but also twist with another one fiber as multimodal sensor to detect bending and pressure. Despite the sensing performance from the unique structure, it is worth noting that the fabrication process by molding is complex and not suitable for scalable production. Fig 2.12c is about a segmental hierarchical fiber surface structure, which is inspired by the arthropod's body and lobster's tail [118]. The key point is the modulus mismatch between soft PU and rigid polystyrene (PS). By coaxial electrospinning, the aligned

fibers with PU core and PS sheath were prepared, and with applying a pre-strain, the relatively rigid PS sheath breaks into many segments. Then after the absorption of Ag precursor and following chemical reduction, dense AgNPs will wrap around the fibers. Similar with the conductive PDMS fibers with microbeads, this segmental structure is capable of inducing more crack because of strain concentration. As seen in Fig 2.12C, bigger pre-strain can greatly increase the GF, but unfortunately with decreased linearity because of the increased nonuniformity of strain distribution.

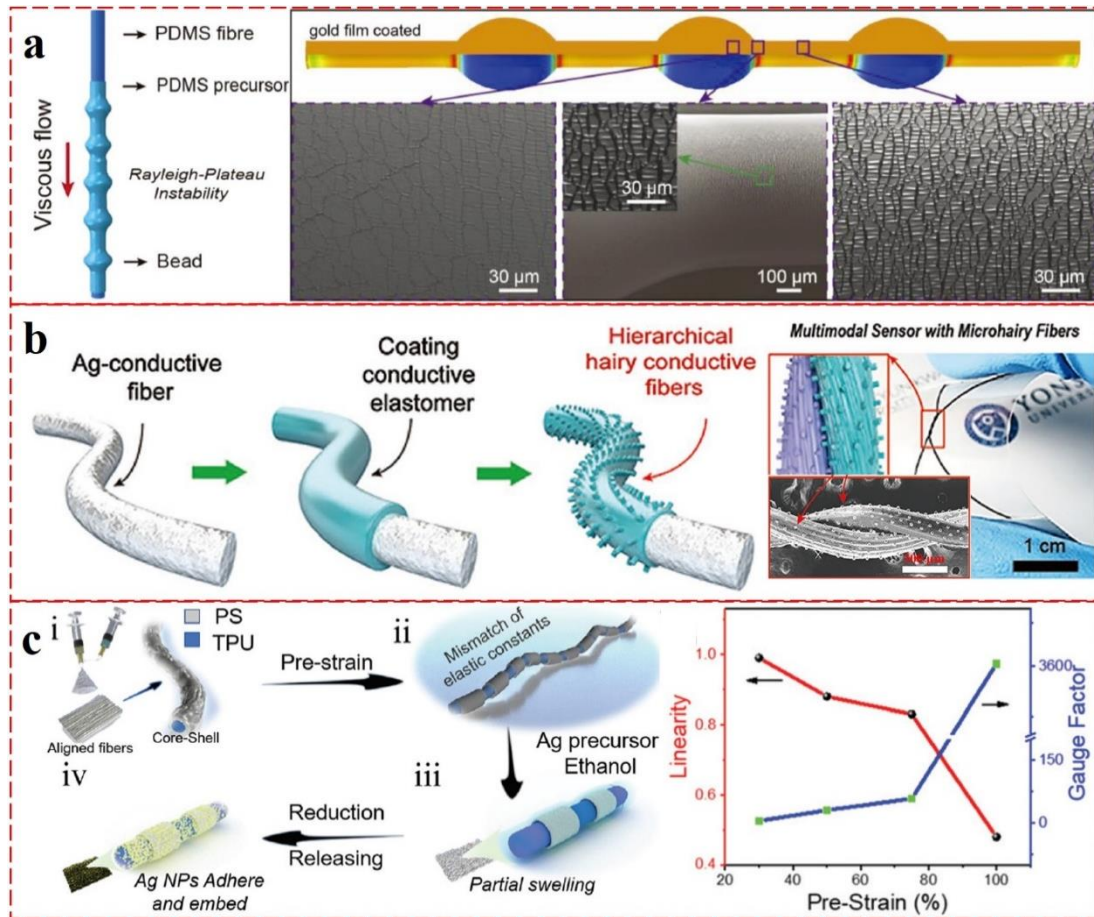


Fig 2.12 (a) Scheme showing the formation of beads on PDMS fiber based on the phenomenon of Plateau-Rayleigh, and the SEM images of the gold layer at different

positions along the PDMS fiber [116]; (b) fabrication flowchart of the microhairy fibers, and the structural scheme as well as SEM image of the microhairy conductive fibers twisted to another one fiber [117]; (c) scheme showing the fabrication process of micro-nanoscale segmental soft-hard fibers, and the relationship between the pre-strain with the linearity and GF of the conductive fibers [118].

2.4.2 Auxetic structure

In this part the applications of auxetic structure in the design of strain sensors are introduced. The strain sensors are attracting more research attention because of their great potential in monitoring various human motions, human-machine interface, and robots controlling. However, the practical application of strain sensor is still on the way, which can stem from the limited sensing performance, uncomfortable wearability and so on. It is well known that the auxetic structure is characterized with the negative Poisson's ratio, which makes the material expand/compress in the longitudinal and transverse directions at the same time. On this basis, the auxetic structure displays two notable advantages in the field of strain sensor: the increased sensitivity and conformal contact with the human skin. Some examples are shown to illustrate them in details. For the increased sensitivity, it is believed that the negative Poisson's ratio is the main reason and the strain concentration is a secondary reason, which both can promote the separation degree of sensing materials whether in 2D flat film or 3D foam. Moreover, because its negative Poisson's ratio, the auxetic strain sensor can deform in both the

longitudinal and transverse directions, thus displaying a unique dome-shape curvature under bending. This special bending behavior can assure the conformal contact between the strain sensor and the complex human body. At last, since the auxetic strategy is independent with sensing materials employed thus can be utilized for other flexible strain sensors.

In general, when a material is stretched, such as the elastic rubber, the material will become longer, but shorter in the transverse direction (Fig 2.13a). The deformation behavior is governed by the Poisson's ratio, which is defined as the ratio of the transverse strain to the longitudinal strain. Compared with the conventional situation, the auxetic material/structure exhibits a unique expansion behavior in both two directions, just as shown in Fig 2.13b. This abnormal deformation behavior endows the auxetic material a negative Poisson's ratio [29,109-110]. Hence, the bidirectional expansion in auxetic material can be utilized to promote the separation degree of sensing materials in strain sensor, thus is promising to increase its sensitivity. On the other hand, since human skin expands in two directions during daily bending and tension, the Poisson's ratio of the human skin is negative depending on the body parts, such as the ankle and knee. The wearable strain sensor should also deform in two directions to keep tight contact with the skin. In this regard, the auxetic material is much preferable, because it will present a dome-shape curve under bending due to negative Poisson's ratio as shown in Fig 2.13c.

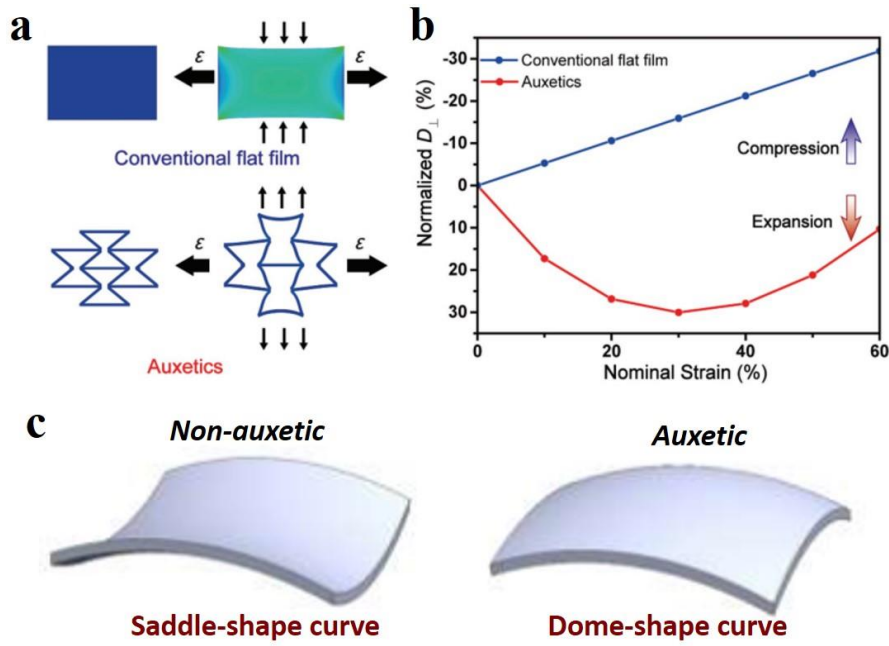


Fig 2.13 Scheme showing the deformation of (a) conventional flat film, and auxetics; (b) normalized displacement in transverse direction under nominal axial strain; and (c) bending behaviors of non-auxetic material and auxetic material, showing the saddle-shape and dome-shape curve, respectively [119].

According to the type of sensing materials and micro/nanostructures, the strain sensor detect strain with different mechanisms, such as the geometrical effect, tunneling effect, piezoresistive effect, and crack propagation. In general, for the flexible strain sensor, to obtain a higher stretchability (>50%), the most used one is the crack propagation, that is, when stretched cracks will originate and propagate in the thin films of sensing materials on the surface of soft polymer substrate. Under this mechanism, the sensitivity of a strain sensor depends heavily on the separation degree of the sensing materials. Compared with conventional material with positive Poisson's ratio, the auxetic material

can expand in longitudinal and lateral directions at the same time. Therefore, the auxetic strategy can be used to promote the crack of sensing materials and further increase the sensitivity of a strain sensor.

Fig 2.14a exhibits a flexible strain sensor incorporated with an auxetic structure, where the conductive SWCNT network was coated on PDMS film, and an auxetic frame prepared by 3D printing was employed to regulate the deformation central PDMS film [119]. As shown in Fig 2.14b, three control strain sensors, including pillar, square, and flat types, were used to their sensitivity with the auxetic one. Firstly, the finite element analysis (FEA) results show that both strain sensors with pillar and auxetic structures exhibit strain redistribution and concentration in the sensing area of SWCNT. In contrast, the strain distribution for flat and square strain sensors is nearly uniform. Fig 2.14c demonstrates that the strain concentration of auxetic and pillar sensors is over 30%, which is much higher those of flat and square ones. Definitely, the strain concentration can cause much larger crack of the sensing SWCNT networks, finally leading to the greatly increased GF in Fig 2.14c. In addition, the GF of auxetic strain sensor is about 8 times of the pillar one, hence it can be concluded that the sensitivity improvement by auxetic structure can be attributed to two factors: negative Poisson's ratio as a main reason and strain concentration as a secondary reason. The SEM images in Fig 2.14d proves that the sensitivity comes from the microcrack within the SWCNT network, and under the same strain, the auxetic strain sensor presents more and longer

microcracks compared with the conventional flat one. In microstructural point of view, these SWCNT islands contact with each other when relaxed, and thus provide a free conductive pathway. When applied with a longitudinal strain, for the flat strain sensor, transverse compression will squeeze the SWCNT islands together and thus makes short microcracks, while expansion in both the longitudinal and transverse directions will occur, which will facilitate the separation of SWCNT islands and thus causes much longer microcracks. Therefore, auxetic strain sensors would provide larger deformation and shorter current pathway than the flat ones, finally resulting in large relative resistance change and sensitivity. As shown in Fig 2.14e, for the radial pulse detection, due to the increased sensitivity, the auxetic strain sensor shows a much higher signal-to-noise ratio, and exhibits discernible medical details within one pulse, including forward wave, peak systolic pressure, discrotic notch, and tricuspid valve opening [119].

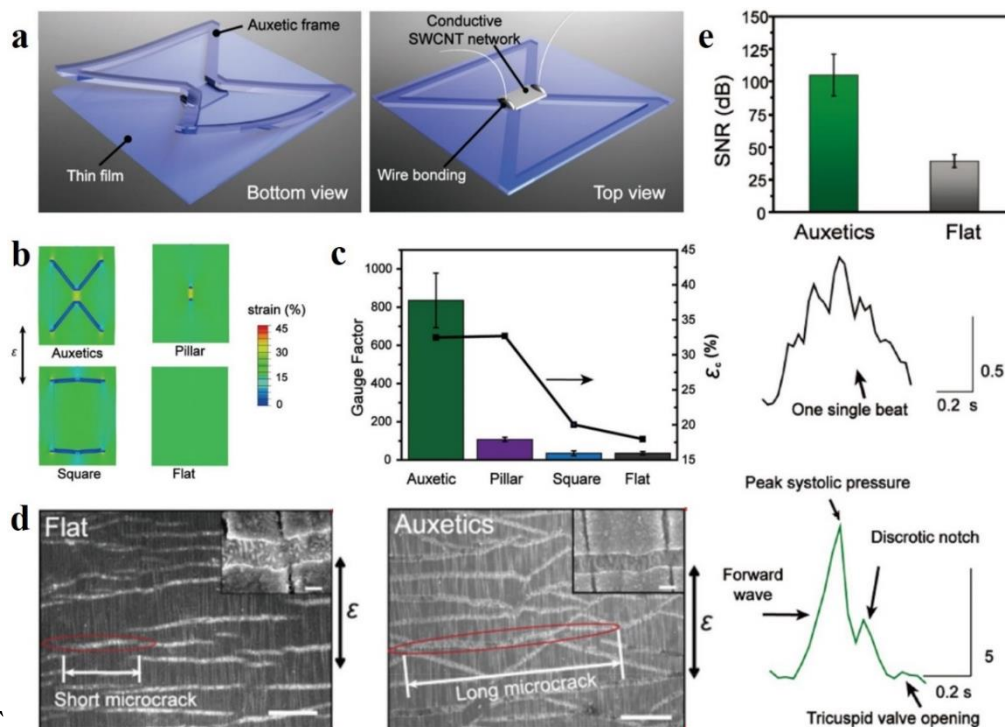


Fig 2.14 (a) Diagram of a strain sensor based on auxetic structure in bottom and top views. The strain sensor is composed of an auxetic PDMS frame prepared by 3D printing, PDMS film, and SWCNT network; (b) strain distribution from FEA simulation under a nominal strain of 15%; (c) GF and strain concentration ε_c comparison; (d) SEM images of microcracks distribution within the auxetic and flat strain sensors under a nominal strain of 15%; (e) applications of the sensor in the radial pulse detection [119].

Auxetic structure can also be used in the foam sensor [72]. As shown in Fig 2.15a, the conventional foam is characterized by a honeycomb structure with a positive Poisson's ratio, but after the treatment of triaxial compression, the re-entrant structure with negative Poisson's ratio can be generated. In this way, an auxetic foam can be easily obtained. Further coated with a layer of conductive micro/nanomaterials, such as graphene, CNTs, and metal nanofillers, the auxetic foam will be endowed with strain sensing ability. Compared with the conventional foam, it is evident the auxetic foam will expand in the transverse direction, which can be attributed to the bidirectional expansion behavior of the re-entrant cell (Fig 2.15b). In Fig 2.15c, for both stretching and compression, the resistance change of auxetic foam sensor is higher than that of conventional foam sensor. The reason can be schematically illustrated by the insets in Fig 2.15c, that is, the deformations and resistances of auxetic foam sensor in both directions increased, whereas for conventional one the deformation and resistance in the transverse direction decreased along with the increase of the deformation and

resistance in the stress direction. Besides the common resistive-typed strain sensor, the auxetic structure can also be applied to prepare a contact-mode triboelectric self-powered strain sensor [120], which is composed of an auxetic polyurethane foam, conductive fabric, and polytetrafluoroethylene (PTFE) (Fig 2.15d). Due to its auxetic properties, the auxetic polyurethane foam can expand into the PTFE during stretching, leading to contact electrification, and a larger contact area between the PTFE and the foam will help the device work effectively as a strain sensor. Moreover, it is proved that this auxetic sensor has the highest sensitivity in all triboelectric nanogenerator devices that are used previously as a strain sensor.

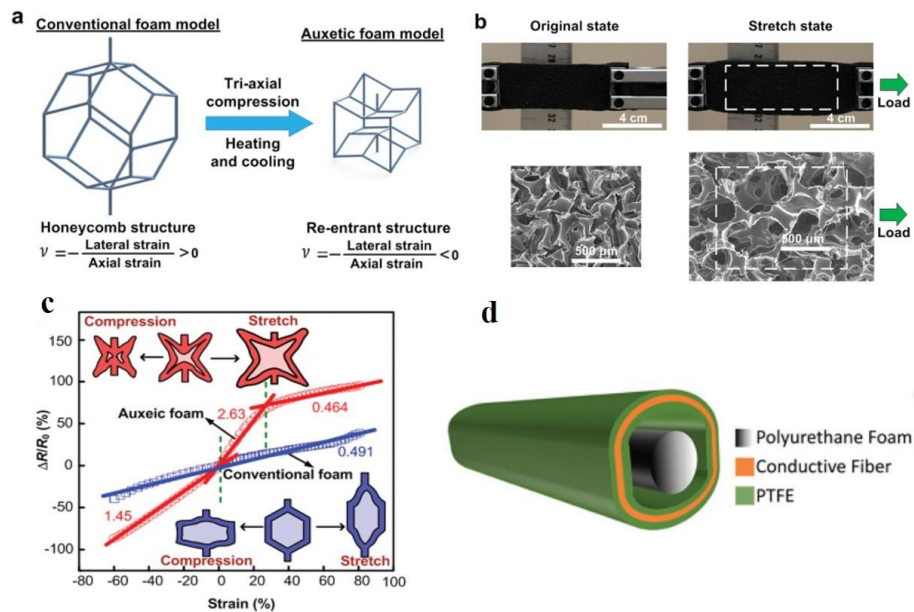


Fig 2.15 (a) Scheme of the structure conversion from conventional foams to auxetic foams [72]; (b) photographs and corresponding SEM images of auxetic foam before and after stretching [72]; (c) relative resistance change with respect to both tensile and compressive strain for conventional foam and auxetic foam sensors [72]; and (d) illustration

of the auxetic triboelectric nanogenerator [120].

2.4.3 Hybrid structure

By combining two different sensing micro/nanomaterials, the conductive network in the strain sensors will show advantages from both two materials, and it has been well proved that this strategy is an effective to construct a distinct conductive network because of the synergistic effect [7,24,31,121-124]. For example, 1D conductive materials, such as CNTs and metal nanowires, are actually flexible and their conductive networks are strong to undergo large strain without destruction. However, because of the flexibility and large aspect ratio, they can also bend and buckle after the releasing of stretching, and the generated buckles will prevent the full recovery of the conductive network. In contrast, the 0D particle-like (e.g. metal particles, CBs) and 2D film-like (e.g. graphene, MXene) conductive micro/nanomaterials can separate with each other quickly even at very small strain, but their stretchability are greatly limited by the rigid properties, where the strain sensors will quickly become nonconductive under a relatively strain. To solve the above problem, the hybrid combination of two different conductive micro/nanomaterials, such as 0D and 1D, 0D and 2D, and 1D and 2D, provides an effective way.

Taking the hybrid structure of CNTs/graphene as a typical example, as shown in Fig 2.16a, the mix of CNTs and graphene prevent the restacking of graphene and

agglomeration of CNTs, and on the other hand, the contact resistance are reduced by the effective formation of interconnection, thus the sensor will have an improved conductivity under lower filler concentration. For the sensing properties during stretching, the pure CNTs network will align along the stretching direction and buckle after releasing, finally showing a periodic and wavy structure in Fig 2.16b. Moreover, the buckled CNTs will not recover by itself after cyclic stretching and releasing. In clear contrast, for the hybrid strain sensor of CNTs/graphene in Fig 2.16c, it is believed that graphene can increase and reinforce the junctions between the single CNTs from the FEA results [121]. As a result, the hybrid conductive network becomes strong, and the buckling of CNTs was suppressed. In addition, as reported by Liu et al [7], in the flexible strain sensor of graphene/CNTs/PU CPCs, the 2D graphene sheet can serve as “spacers” to separate the entangled CNTs, and the CNTs will bridge the gap between individual graphene sheets. In this way, the percolation threshold of the strain sensor will be evidently reduced. As shown in Fig 2.16d, under a small strain, the hybrid conductive networks are not easy to be broken because of the interconnection between CNTs and graphene, thus the strain sensor will show good reversibility and reproductivity. But the hybrid conductive networks will be destroyed under large strain, and this phenomenon can be regulated by pre-straining. Moreover, the incorporation of metal nanoparticles and nanowires into graphene can greatly decrease the initial resistance [24,31,125-127], and as shown in Fig 2.16e, the resistance change of the strain sensor mainly comes from the overlapping area decrease under strain. The small

and uniformly distributed AgNPs bridge the neighboring graphene flakes, thus forming a 3D conductive network and decreasing the contact resistance between the graphene flakes. On the other hand, under strain, the AgNPs are able to fill the generated microcracks and bridge the separated graphene flakes, resulting in the enhanced uniformity of generated microcracks, which is beneficial to a wider working strain range and linearity.

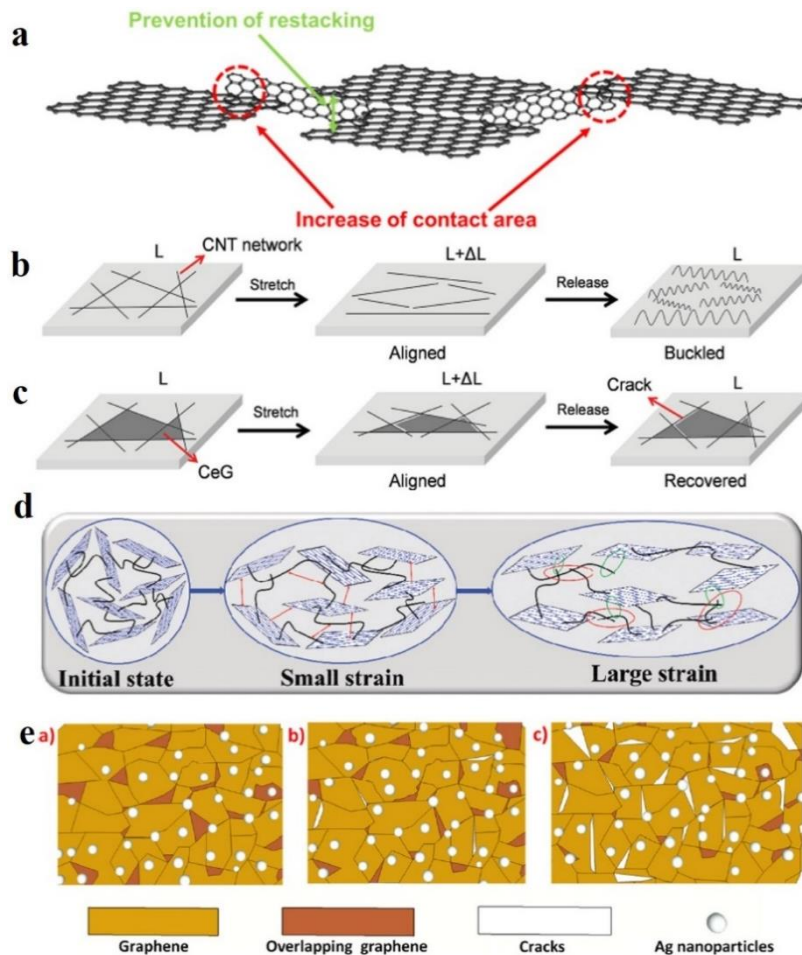


Fig 2.16 Schematic illustration of (a) the interaction between CNTs and graphenes [123], and the microstructural change of (b) CNTs thin film; (c) CNTs/graphene hybrid thin film under stretching and releasing [121]; (d) hybrid networks in the

graphene/CNTs/PU CPCs under different strains [7]; (e) Scheme showing the structure change of AgNPs/graphene strain sensor in the three states of strain free, small strain, and large strain [24].

2.4.4 Prestretching

Prestretching has been well proved to be an efficient methodology to manipulate the structure of conductive layer for different objectives [125,128-132]. First of all, as shown in Fig 2.17a, the rubber fiber was prestretched and wrapped with CNTs layers, and the orientation of conductive CNTs layer can be reserved [128]. Then after releasing the strain, the unique short and long buckling periods reversibly appear out of phase in the fiber axial and belt directions, which endow the conductive rubber fiber a much stable resistance of less than 5% under strain up to 1000%. Besides the application of stretchable and resistance stable electrode, the conductive fibers with wavy or wrinkled can also be used in the design of pressure sensor. As shown in Fig 2.17b, applied with the similar strategy of prestretching the PU fiber, after the coating of conductive AgNWs and releasing strain, core-shell conductive fiber with wrinkled microstructures can be obtained [131]. Then the piezoresistive fibers with helix structure can be further built by twisting the two wrinkled conductive fibers together. The conductive wrinkles on the surface can greatly increase the number of contact points between the two fibers, thus inducing higher sensitivity than the commonly planar one to applied pressure. Moreover, in the design of stretchable strain sensor, prestretching can be utilized to

form certain configurations on the conductive layer in advance [125,132-133]. As displayed in Fig 2.17c, the conductive TPU film coated with AgNWs/graphene layer is originally uniform and flat. Due to the weak adhesion between conductive fillers and weak interface between the conductive layer and TPU, prestretching will induce the formation of crack on the conductive layer. After releasing, the TPU film recovers to the initial state because of its excellent flexibility. The resilience of the top conductive layer is relatively poor, thus leading to the typical overlap morphology. As a result, when applied as strain sensor, the prestretched conductive film shows a nearly unchanged resistance at the initial strain range. Only with further increased strain, the overlapped parts separate and cracks will appear, generating greatly larger resistance increase. Therefore, by controlling the portion of overlapped area, it is considered that higher prestretching strain will bring larger working strain range, but together with decreased sensitivity.

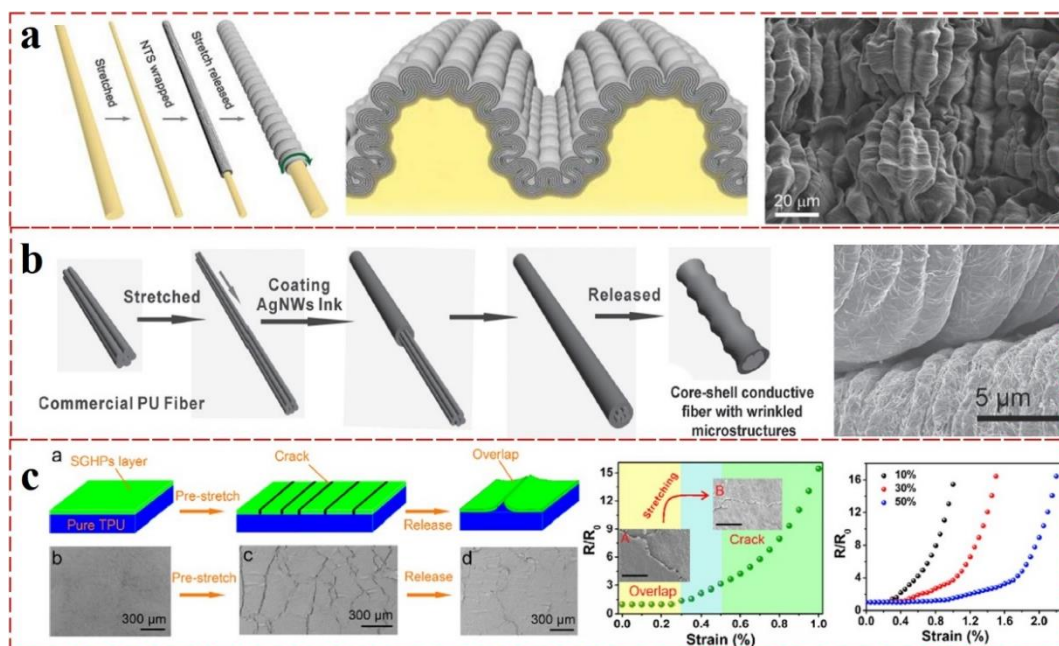


Fig 2.17 (a) Schematic illustration of fabrication process, structure and SEM image about the hierarchically buckled CNT sheath-rubber core fibers [128]. (b) fabrication of conductive AgNWs shell-PU core fibers with wrinkled microstructures, and SEM image of piezoresistive fibers by twisting two fibers as pressure sensor [131]. (c) Scheme and SEM images of conductive TPU films coated with AgNWs/graphene layer after prestretching and releasing, and the resistance change versus strain curves of the conductive films treated by different pre-stretching strains [125].

2.4.5 Self-cleaning

The self-cleaning of a strain sensor means the property of repelling water and the tendency of not absorbing water. Being an important interface between human bodies and the environments for long-term healthcare monitoring, the strain sensor should protect the mankind against invasion from surroundings. However, biodegradation of textile can be caused by the growth of microbes which are promoted especially in the presence of humidity, heat and organic matter [134]. As the microbes may not be removed by laundering, it can even be carried and transmitted to individuals. Therefore, hydrophobicity is a favorable feature for preventing the transmission of microbes from the sensor to the user. The need of laundering could also be minimized if self-cleaning could be achieved. Besides, when the invasion of external liquids is prevented, the operation stability of the strain sensor can be guaranteed and its lifetime can be extended. Therefore, researchers have proposed different techniques for the

incorporation of waterproof surface or self-cleaning function into wearable strain sensors. When roughness is produced on the fabric surface, superhydrophobicity is resulted and dirt particles could hardly be accumulated [135-136]. By repelling peripheral liquids such as human sweat and rainwater, the strain sensors could also resist to corrosion. Furthermore, via additional PDMS encapsulation, it was reported that the surface energy can be greatly reduced, thus forming a superhydrophobic surface [99,137]. Similarly, Yang et al. fabricated a waterproof supercapacitor fabric by encapsulation with hydrophobic polyester fabrics and further spraying with a polytetrafluorethylene agent [92]. Nonetheless, the method of encapsulation is not suitable for e-textiles because of the weakened breathability and comfort for long-term wearing. On the other hand, water repellency could also be obtained by creating nanowhiskers on fabrics, as the small spaces between whiskers is able to generate a high surface tension, allowing the retention of water on the top of the nanowhiskers, which can be termed as peack fuzz effect or Lotus effect [135,138]. Since whiskers also permeate gases, the breathability of textile could be maintained at the same time. However, liquid can pass through the fabric when there is an exertion of pressure [131]. As the hydrophobicity of stretchable strain sensor should be maintained even at severe stretching, other suitable methods should be adopted for flexible electronics, such that the hydrophobicity performance would not be affected by the application of pressure.

2.5 Fabrication Technologies

The fabrication technologies depend on the materials types, structure and application fields of the strain sensors. Herein the fabrication technologies of strain sensors will be briefly introduced according to the configurations of strain sensors, i.e., 1D fiber-like, 2D film-like, and 3D foam-like structures.

The strain sensor is composed with the soft polymer and conductive sensing materials. Therefore, the fabrication process of 1D strain sensors include the fabrication of 1D polymer and sensing materials, and their combination to form the final strain sensors. For brevity, one can immediately use some available fibers or fibrous materials, such as the PU yarn (Fig 2.18A) [139] and even the common elastic band (Fig 2.18C) [58], or prepare the continuous fiber by spinning (Fig 2.18B) [18]. Then by simple dipping in the conductive graphene/CNTs solution, the graphene/CNTs will be coated on the surface or embedded into the substrate, thus the polymer fiber will acquire their sensing capability. Moreover, the conductive CNTs fiber can also be prepared by spinning [140]. The CNTs fibers will align along a certain direction and the highly oriented CNTs arrays will be obtained on the soft polymer substrate. Recently, Zhou and coworkers developed a coaxial wet spinning technology [19], where the CNT/CH₃SO₃H dope from the inner channel and the TPE/CH₂Cl₂ solution from the outer channel were introduced into the ethanol coagulation bath simultaneously. The strain sensor with a (TPE) core–(CNTs) sheath structure can be formed directly by only one simple step,

which shows great potential in continuous and scalable fabrication.

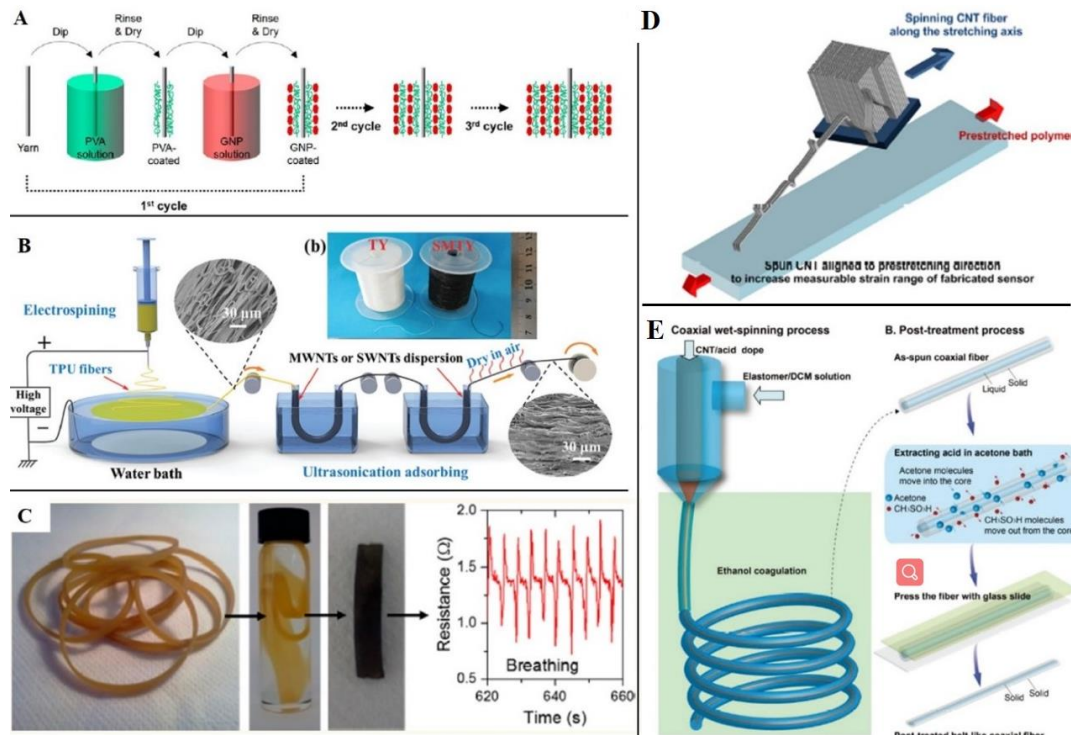


Fig 2.18 Preparation steps of 1D strain sensors by (A) dip coating the PU yarn in graphene solution [139] (B) electro spinning of PU fibers, followed by dipping in CNTs solution [18] (C) infusing graphene into elastic bands [58] (D) dry-spinning CNT fiber on Ecoflex substrate [140], (E) coaxial wet-spinning of the CNT/PU sensing fibers [19]

For the 2D film strain sensors, the soft PDMS is always the first choice for polymer substrate because of its easy operability and excellent properties as transparent rubber.

Based on PDMS, many different methods have been developed as shown in Fig 2.19 [5,107,141], which include filtration method (Fig 2.19A), transferring and micromolding method (Fig 2.19B), printing technology (Fig 2.19C), solution mixing

(Fig 2.19D), coating technique (Fig 2.19E), and chemical vapor deposition (Fig 2.19F). Through filtration method, the uniform film of conductive fillers can be obtained and combined with the soft polymer substrate. Printing technology allows the deposition of arbitrary pattern on the polymer substrate by a controlled printing nozzle. The transferring and micromolding method is usually used to replicate some special patterns from a template. The coating technique can deposit the conductive fillers on the surface of polymer substrate by physical or chemical methods. The solution mixing is simple and fast to get a CPCs strain sensor. At last, by the chemical vapor deposition, one can obtain a uniform, thin and intact graphene/CNTs layer by in-situ growing.

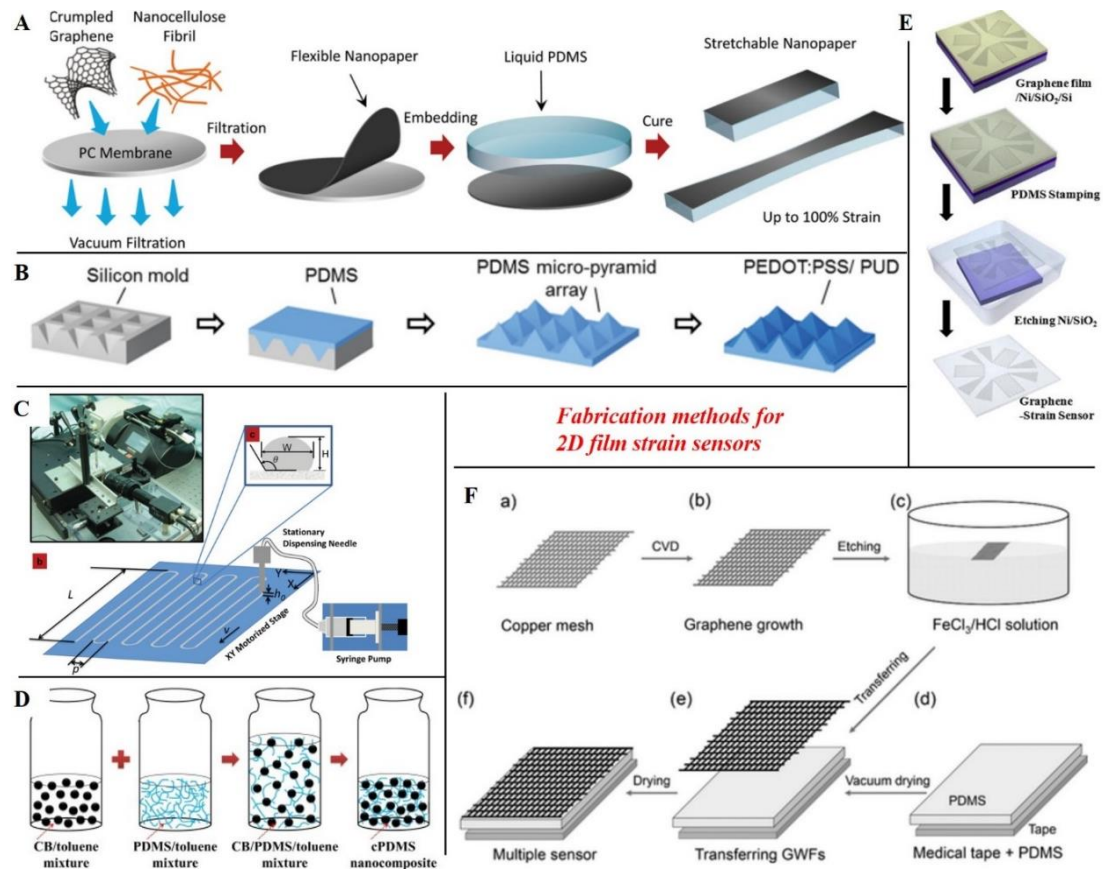


Fig 2.19 Examples showing the different fabrication methods for 2D film strain sensors

[5,107,141]: (A) filtration method, (B) transferring and micromolding method, (C) printing technology, (D) solution mixing, (E) coating techniques, and (F) chemical vapor deposition.

Due to the merits of high porosity, lightweight, and mechanical flexibility, conductive porous foams are considered as an ideal candidate in the application of strain sensors for pressure detecting. Until now, the performance of 3D foam-based strain sensor has been greatly improved, and many highly conductive foams have been developed and used as flexible pressure strain sensors. For example, as shown in Fig2.20a, by solution coating on commercial PU foam, Yao et.al coated the graphene oxide nanosheets on the backbone of PU foam. After reduction by hydrogen iodide, hydrothermal treatment and strong pre-compression at 95% strain was further applied to create a dense and fractured microstructure, respectively [142]. Moreover, due to the simple method, the foam-based pressure sensors can be easily scaled up to allow the fabrication of artificial electronic skin with a complicated sensor pixel array [142]. With such a structure, the spatial pressure distribution on the electronic skin can be precisely measured. Besides the direct usage of commercially available foam, lightweight conductive porous foams can also be fabricated by other method. For example, Dai et al, prepared a variety of foam based conductive polymer composites by thermal induced phase separation, i.e., the freeze-drying method [143-145]. Meanwhile, graphene and CNTs were selected as the conducting fillers. The addition of graphene or CNTs greatly improve the strength of

the cell wall, resulting in a robust porous structure with notable compression and stability. With the addition of only 3 wt% graphene, the foam's compression strength and modulus can be enhanced by about 110% and 185%, respectively [144]. After the stabilization effect of cyclic compression process, the pressure sensors can exhibit a good recoverability and reproducibility. In addition, via modifying the fabrication methodology, a novel aligned conductive foam was obtained by directional freezing [145]. Compared with the previous disordered foam, the compression strength and sensing properties are greatly improved. The improved performance should be attributed to the ladder-like cells with interconnected walls along the orientation direction. With the aligned structure, the foam can recover well during the compress-release testing cycles, finally leading to desirable reversibility, reproducibility and linearity. The lightweight of prepared sensor can be well illustrated by Fig 2.20b, where the sample stood on the top of flowers, while no bending of the petal can be observed.

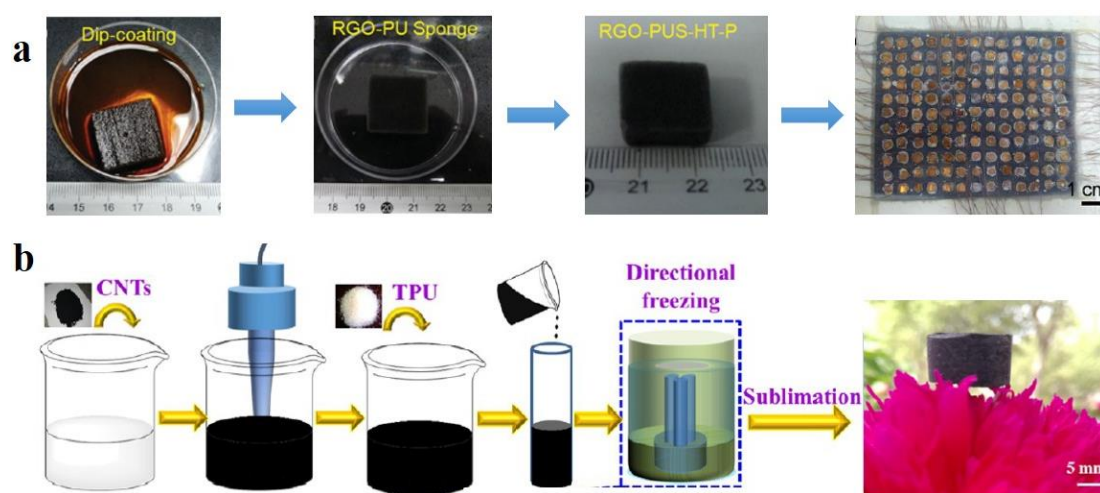


Fig 2.20 (a) Sketch showing the fabrication process of foam-based pressure sensor, and

the fabricated artificial skin based on the foam based pressure sensor [142]; (b) Scheme showing the preparation process of aligned CNT/PU foam, and photo of a lightweight foam based pressure sensor standing on a flower [145];

2.6 Summary

In summary, the flexible strain sensors can be obtained by constructing conductive network on flexible polymer substrate. Under strain, the soft substrate bear the strain and transfer it to the conductive network, leading to the generation of electrical signals. According to the categories of detected electrical signals, the flexible strain sensors can be classified into two main types: the resistive and capacitive type. Compared with the capacitive type, the resistive strain sensors display advantages including simple fabrication process and easily manipulated performance, thus attracting more and more attention recently. Usually, the sensing performance of a strain sensor is evaluated in terms of sensitivity, stretchability, linearity, hysteresis, repeatability, and durability. To improve the sensing performance, certain pattern or auxetic structure can induce strain concentration and enlarge the deformation of polymer substrate, finally leading to increased sensitivity. On the other hand, the conductive networks can also be controlled by applying hybrid conductive materials with different dimensions, and prestretching is also another effective method to manipulate the conductive network by generating

cracks and wrinkles. In order to obtain strain sensors with designed structure, many fabrication technologies have been successfully developed to prepare 1D fiber-like, 2D film-like, and 3D foam-like strain sensors.

However, the practical applications of the strain sensor are still challenging. First of all, the interface bonding between the conductive materials and polymer is always too poor to assure a good durability. Secondly, the wearing comfort is believed to play a vital role in detecting human motions, which should require the good conformal contact of the strain sensors with the human skin. To this end, as an appealing alternative, textile-based strain sensors are becoming a research hot because of its unique merits such as good breathability from the porous structure, light weight and softness for long-term wearing, low cost and full-fledged textile industry for large scale fabrication, and so forth. Last but not least, the real application of strain sensors further requires the high integration of many other parts, like the power supply, data collection, wireless communication and processing units, nevertheless, there are very few works on this point. With the unremitting efforts from scientists and engineers all over the world, a booming development and applications of wearable strain sensors is highly expected in the near future.

CHAPTER 3: Design and Fabrication of Flexible One-Dimensional Strain Sensor Based on Polyurethane Yarn, Graphene and Polydopamine Encapsulation

3.1 Introduction

In modern human life, there is a growing demand for flexible and wearable electronic systems for various applications. Flexible strain sensors with qualified performance is one of the necessary and integrant parts of such wearable electronics systems. By virtue of transforming the mechanical deformations into processible electrical signals, the flexible strain sensors are expected as an efficient device to monitor human motions and various physiological conditions, displaying huge potential in the future smart applications, including but not limited remote health monitoring, human-machine interaction, and fitness tracking. Hence, a great many flexible strain sensors with excellent sensing performance have been successfully developed through decades of technology advancement [1,73,77,101-102,146]. In general, according to the architectures, the varieties of strain sensors basically include one-dimensional (1D) fiber-like, two-dimensional (2D) film-like, and three-dimensional (3D) block-like. In contrast, the 1D strain sensors show unique advantages such as low weight, small size, low cost, and so on. Moreover, due to its good tailorability, the 1D strain sensors can

be further assembled into 2D and 3D structures. Thus, it is of great importance to develop high-performance 1D strain sensors.

Generally, two strategies are often utilized to prepare the flexible 1D strain sensors. The first strategy is to prepare fiber-like strain sensors by applying fiber-spinning method of the conductive polymer composites [19,147-148]. This strategy is advantageous in the excellent mechanical property and durability of the prepared strain sensors. Nevertheless, the limitations of this strategy of complex preparation flowchart and relatively high production cost are always unavoidable. Moreover, the increasing of electric conductivity of the such strain sensors is very challenging mainly because of the limited content of conductive materials in the soft polymer matrix, which will consequently weaken the sensing properties of the strain sensors. The second strategy which offers the fiber/yarn the strain sensing capability is to coat a conductive layer onto the surface of fiber/yarn substrates via different approaches such as dip-coating [97,104,149]. Compared with the fiber spinning strategy, this surface coating strategy has the unique merits such as the facile and low-cost preparation process. Since the continuously conductive layer can be easily formed on the surface of fiber/yarn, the high conductivity of sensor and thus its good sensing properties can be achieved. In the fabrication of such yarn-type sensors, carbon-based conductive materials such as carbon particle, carbon nanotube and graphene are commonly used to form the conductive layer due to their good conductivity and mechanical property as well as

environmental stability while the 1D elastic polymers including polyurethane and rubber are served as fiber/yarn substrates for bearing in the conductive layer. By using such material system and fabrication method for strain sensors, one of the prime issues consist in that there lacks strong adhesion between the conductive layer and soft substrate and thus a poor interface between them, resulting in weakened durability and stability of these strain sensors. Especially, in the case of nonplanar deformations like mechanical bending and torsion applied to the strain sensors, the conductive layer is prone to directly shed from the polymer substrate [150], and at last the sensing performance deteriorating of strain sensors is always inescapable. In fact, most of reported flexible strain sensors possess a relatively low durability less than 10000 testing cycles [24,46,65,119,151].

The well-known polydopamine (PDA), inspiration originating from the mussel adhesive foot proteins, has been successfully demonstrated to be a facile, low cost and versatile material to modify nearly all the existing material surfaces [152-154]. Due to the coexistence of catechol and amine functional groups, the dopamine monomer can similarly self-polymerize to produce a thin PDA film, which can adhere strongly on different surfaces based on multiply binding mechanisms of π - π stacking, coordination bonds, hydrogen bonds, electrostatic interactions, etc. The successful applications of adhesive PDA on various substrates have been well proved. In consideration of its notable adhesion, it is highly expected that the PDA can be applied to enhance the

interface adhesion between inorganic conductive materials and organic polymer materials during the fabrication of many strain sensors. Nevertheless, until now there are very few research on the reinforcement of interfacial bonding between carbon-based conductive layer and polymer substrate assisted by PDA for fabricating mechanically stable and durable strain sensors. In addition, in order to detect and monitor human motions, the flexible strain sensor and the corresponding textile-based system worn on the human body always bear the continuous mechanical deformations. However, the most reported flexible strain sensors can only detect the tensile strain, which have not exhibited the capability to detect the multi-physical deformations, particularly on the combining tensile- and bending-induced strains. The possible reason is that the poor interaction between the conductive layer and elastic substrate lowers the bendability of the strain sensor and thus limits the detection of such combining deformation. Consequently, such kind of sensor cannot meet the requirements of the recognition of multifaceted human motions.

In this chapter, to address the aforementioned issues, we developed a flexible and wearable 1D yarn-type strain sensor with outstanding weavability by employing a simple dip-coating method, making the 1D strain sensor to be easily integrated into the fabric structure. Because of its notable extensibility and elasticity, the commercially available polyurethane yarn (PUY) was selected as the flexible polymer substrate (as a sensing yarn core) to bear in the conductive layer formed by the multilayered reduced

graphene oxide (rGO) (as a sensing yarn sheath). Since the PUY is a commonly used elastic yarn for producing elastic fabrics in textile industry, the as-fabricated PUY-based sensor likes a normal yarn for making fabrics, allowing the scalable and low-cost fabrication of such yarn sensor-based wearable textiles by using the existing fabric production machinery. More importantly, in the fabrication of yarn sensors, based on the above-mentioned inspiration by mussels and excellent adhesive property and biocompatibility, the PDA was introduced as an adhesive and biocompatible package material to enhance the interface interaction between the rGO layered sheath and PUY core for fabricating mechanically robust strain sensors. Meanwhile, the introduced PDA can reinforce the connection between the rGO nanosheets for forming a strong and stable conductive sensing layer, thus greatly stabilize the conductive path in the sensing layer for undertaking the cyclic stretching-releasing on sensors, which is crucial for the sensors to obtain the outstanding performance. Additionally, the PDA layer formed on the sensor surface as a package layer can not only provide a good protection for the sensor to assume the following fabrication process of textiles and against the environment as well as a friendly contact with human skin, but also facilitate the tight wrapping of the rGO layer around the surface of PUY, thus significantly enhance the integrity of yarn sensor. Because of above-mentioned rational design of material system with reasonable strategy for structure construction, particularly the employing of PDA, the resultant yarn sensor exhibits superior durability up to 30000 cycles at 50% strain for the first time that is more than three times the durability of most reported 1D

strain sensors. The sensor also possesses a high sensitivity (a gauge factor (GF) of 131.8), a very low hysteresis (a hysteresis error (δh) of 3.6%), and an excellent linearity (a correlation coefficient of 0.999). In addition, for the similar reason, the as-prepared sensor proves a good capability to sense the multiple deformation of tensile strain and bending, showing very stable sensing performance under applied cyclic stretching-releasing (up to 5000 cycles). More importantly, the lightweight and small-sized yarn sensor is much promising to be integrated into fabric structure like common yarns for fabricating the wearable sensing fabrics, meanwhile reserving the unique merits of fabric including the wearing comfort and aesthetic beauty of clothing, thus endowing the possible applications for long-term and real-time monitoring of human motions for personal therapy and remote medical system.

3.2 Experimental Section

3.2.1 Materials

PUY (140D) was obtained from Notion Merit Limited, which comprises ten twisted monofilaments with each diameter of 40 μm . As displayed in Fig 3.1, the PUY presents a very stretchable tensile behavior with an elongation at break of ca. 460%. The high-purity rGO was purchased from Chengdu Organic Chemicals Co. Ltd., with the detailed

information including purity of >98 wt%, oxygen component of 3.52%, thickness of 1-3 nm, layers of <3 and scale of >50 μm . Sodium lauryl sulfate (SLS), polyvinyl alcohol (PVA, weigh-average molecular weight: 89000-98000), and dopamine hydrochloride were obtained from Sigma-Aldrich, Inc.,.

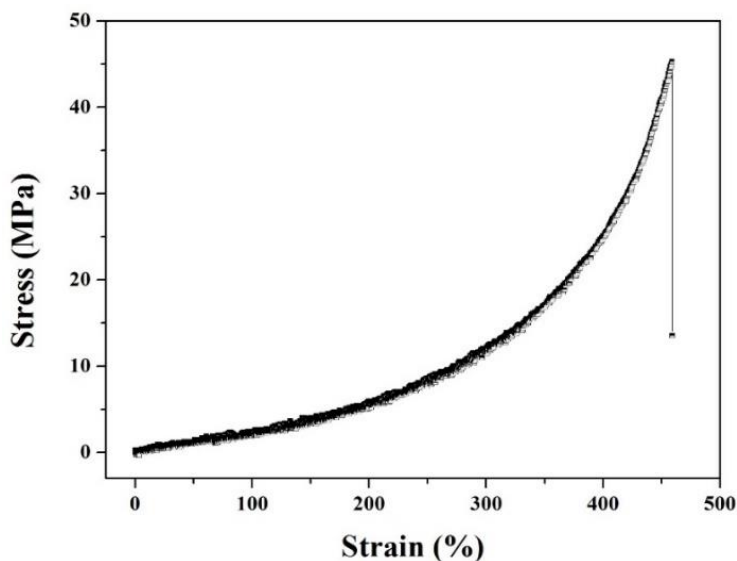


Fig 3.1 The tensile stress versus strain curve of PUY, which was conducted by the machine of Instron 5944, with the gauge length of 10 cm and speed of 100 mm/min.

3.2.2 Preparation

The PUY was cleaned in order via ultrasonication in ethanol and deionized water for 10 min respectively. Before coating, the PVA solution (0.5 wt %), which facilitates the adhering of rGO nanosheets during coating, was obtained by dissolving PVA powder in hot water of 85 °C. The rGO dispersion (0.8 wt %) was prepared by ultrasonating the rGO nanosheets into deionized water for 30 min, wherein 0.4 wt % SLS was added

to facilitate the uniform dispersion of rGO nanosheets. Then the PUY was dipped into the PVA solution for 5 min, followed by rinsing in deionized water and drying in air. The PVA coated PUY was dipped into the rGO dispersion for 5 min, and deionized water was used to wash away the unabsorbed rGO. After drying in air, the above two dipping steps were repeated for another five times to obtain a thick rGO coating with 6 layers. Furthermore, dopamine solution with a concentration of 2 mg/ml was prepared by dissolving dopamine in Tris-HCl buffer solution (pH = 8.5), and the rGO coated PUY was immersed into the dopamine solution for 12 h at room temperature. At last, the yarn strain sensor was cleaned in deionized water and fully dried in air.

3.2.3 Characterization

For the morphological observation, the samples were sputter-coated with a thin gold and observed with a field-emission scanning electron microscope (SEM, JEOL JSM-6335F, Japan) at 5 KV. The molecular information was examined by Fourier transform infrared spectroscopy (FTIR, PerkinElmer, USA) in attenuated total reflection mode, with the spectra recording range of 650-4000 cm^{-1} and resolution of 4 cm^{-1} , respectively. For the electro-mechanical properties, the yarn sensor was cut into a length of 20 mm and connected with two Cu wires as electrodes at both ends. The uniaxial stretching tests were precisely controlled by using an Instron universal test instrument (Model 5944, Instron Instruments, USA), and meanwhile a Multimeter (Model 2010, Keithley, USA) was coupled to real-time record the resistance change of the strain sensor.

3.3 Results and Discussion

3.3.1 Fabrication of yarn strain sensor

Fig 3.2 illustrates the fabrication of the PUY based sensor. The process is all-solution based and operated at mild conditions, which is facile and much promising for massive production. After dipping in PVA solution (Fig 3.2a), the surface of PUY was coated by a thin PVA layer, which can serve as an adhesive layer to anchor the inorganic rGO sheets. By virtue of various noncovalent interactions, the rGO sheets were layer-by-layer assembled and attached on the surface of PUY. Followed by repeated coating in PVA and rGO solutions, a dense rGO layer can be formed around the PUY (Fig 3.2b), finally forming an effective path for electron transiting. To protect the outer rGO layer, a PDA layer was further coated around the rGO layer by reaction in dopamine solution (Fig 3.2c and d). The well-known PDA, inspiration originating from the mussel adhesive foot proteins, has been successfully demonstrated to be a facile, low cost and versatile material to modify nearly all the existing material surfaces. In details, due to the coexistence of catechol and amine functional groups, the dopamine monomer can self-polymerize to produce a thin PDA film on surfaces in a weak alkaline pH solution. The reaction mechanism is illustrated in Fig 3.3, firstly dopamine is oxidized by dissolved oxygen, leading to the production of dopamine-quinone; Secondly, via a

nucleophilic intramolecular cyclization reaction, the quinone can be converted into 5,6-dihydroxyindole (DHI). Moreover, the PDA can be generated in noncovalent and/or covalent ways [152]. For the noncovalent way, the PDA is in the form of noncovalent assemblies of dopamine, dopamine-quinone and DHI, while for the covalent way, the PDA is composed of heteropolymer or eumelanin-like oligo-indoles by covalent coupling. Despite the fact that the formation mechanism of PDA is still not thoroughly clear, the successful applications of PDA on various materials, including graphene sheets [155], have been well proved. By forming the adhesive PDA layer, the sensor can be protected from damage when subjected to various mechanical deformations during fabrication and daily using, thus ensuring the mechanical and electrical stability.

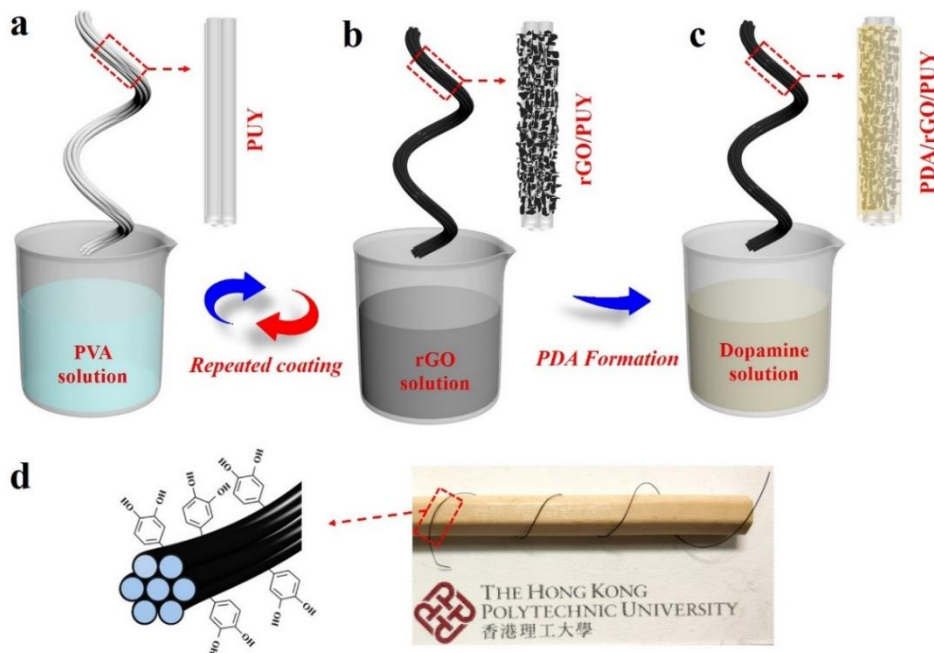


Fig 3.2 Scheme illustrating the preparation process of PDA/rGO/PUY strain sensors.

(a) Dip coating in PVA solution. (b) Dip coating in rGO solution. (c) Reaction in

dopamine solution. (d) Photo of the sensor of PDA/rGO/PUY wrapped around a pencil, showing an excellent flexibility.

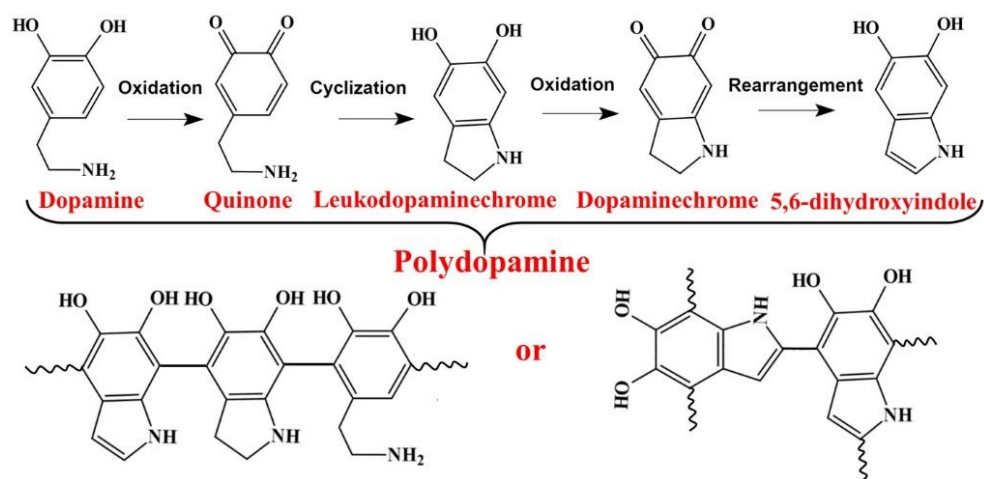


Fig 3.3 Scheme showing the chemical formation mechanism of PDA

3.3.2 Morphology and structure of yarn strain sensor

The surface morphologies of the sensor were tracked by using SEM. As shown in Fig 3.4a₁ and a₂, the PUY consists of ten uniform PU filaments, and evidently each filament presents a smooth surface (Fig 3.4a₃). The unique structure of fiber assemblies can efficiently prevent crack propagation and catastrophic failure, thus endowing the PUY an excellent fatigue resistance, which plays a crucial role in the durability of sensor. Moreover, the large surface areas and rich grooves between each filament can contribute to immobilize more rGO sheets, which is in favor of better conductivity and sensing performance. As revealed by Fig 3.4b₁ and b₂, after 6 times' coating the surface of PUY was wrapped by a uniform rGO layer with a thickness of ca. 4 μm. Thus, the

rGO layer formed a conductive sheath as electron pathway around the PUY. In the zoom-in view of Fig 3.4b₃, the 2D rGO sheets can be clearly observed, and with the aid of PVA, the rGO sheets were found to be closely interconnected with each other. Since the tunneling resistance cannot be neglected for separated rGO sheets, the tight connection between the rGO sheets is of great significance to provide effective pathway for electron. As displayed in Fig 3.4c₁ and c₂, after a reaction over 12 hours, the dopamine molecules can reach the exposed rGO surface and self-polymerize into a continuous PDA film, surrounding the sensor tightly. In a zoom-in view of Fig 3.4c₃, the outmost rGO sheets were evenly covered by PDA, and it is clear that no rGO sheets were exposed to air when compared with the uncoated one (Fig 3.4b₃), indicating that a stable microstructure of PDA/rGO/PUY has been achieved.

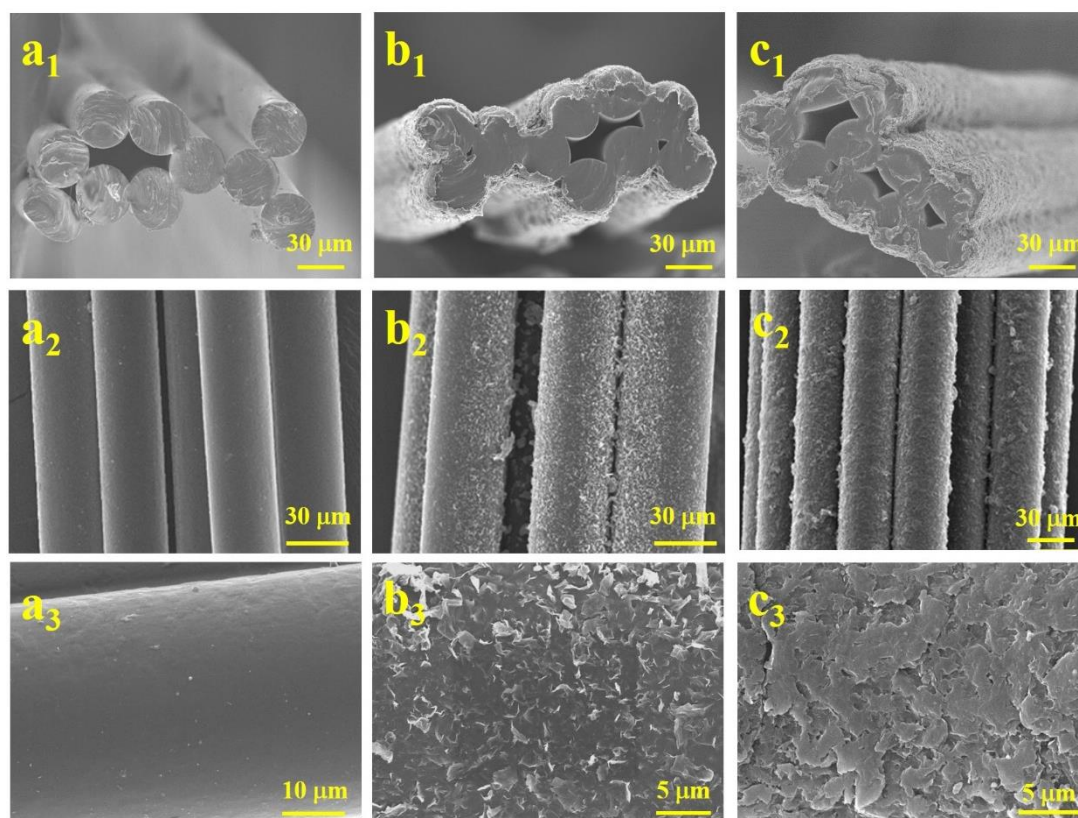


Fig 3.4 SEM morphologies of (a₁) PUY, (b₁) rGO/PUY, and (c₁) PDA/rGO/PUY strain sensor on the cross section, and SEM morphologies of (a₂, a₃) PUY, (b₂, b₃) rGO/PUY and (c₂, c₃) PDA/rGO/PUY strain sensor along the length direction respectively.

The formation of PDA layer can also be confirmed by the FTIR result. It is known that the PDA molecules are characterized by the benzene rings, phenolic hydroxyl and amido groups (Fig 3.3). As seen in Fig 3.5, one can observe the absorption peaks of PDA, including 1290 cm⁻¹ (stretching vibration of phenolic C-O) and 1505 cm⁻¹ (shearing vibration of N-H). The absorption peak of 1600 cm⁻¹ should be the overlap of C=C resonance vibration in aromatic ring (PDA) and bending vibration of N-H (PDA and PUY). The results support the presence of PDA on the rGO/PUY surface [156-157].

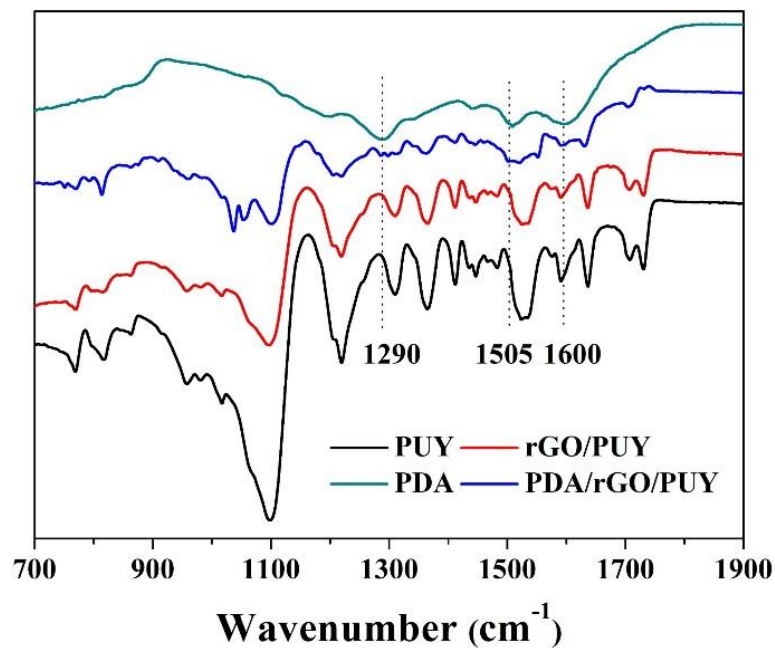


Fig 3.5 FTIR curves of PUY, rGO/PUY, PDA, and PDA/rGO/PUY strain sensor.

3.3.3 Electro-mechanical properties of yarn sensor for sensing tensile strain and PDA influence

Fig 3.6 presents the electro-mechanical properties of prepared PDA/rGO/PUY sensor. As shown in Fig 3.6, with the increase of strain, a gradually higher resistance change can be obtained, directly demonstrating the outstanding sensitivity of sensor to the external strain. To evaluate the sensing performance, parameters of GF, δh , and correlation coefficient (R^2) were utilized to evaluate the sensor's sensitivity, hysteresis and linearity, respectively. The GF can be calculated by the equation of $GF = (\Delta R/R_0)/\varepsilon$, where R_0 is the initial resistance, ΔR is the change between the initial resistance (R_0) and the final resistance (R_f) under an applied strain ε . According to this equation, under the same applied strain, the sensor shows higher sensitivity for larger resistance change, which should come from the big change of the conductive rGO networks upon the strain. As shown in Fig 3.7, the sensor can work well in a wide strain range from 0 to 90%, indicating that this yarn sensor is stretchable enough to detect the large strain. In addition, it is found that the resistance change curves depend on the applied strain. When the strain is smaller than 50%, the GF of sensor exhibits a consistent value of 50.0, and further increasing the strain from 60% to 90%, the GF displays an increasing trend. At a large strain of 90%, the GF reaches a high value of 131.8. Besides, hysteresis and linearity are two important sensing properties. The hysteresis error can be evaluated by δh as following [96]:

$$\delta h = \frac{\Delta R_{max\ difference}}{\Delta R} \times 100\% \quad (1)$$

where $\Delta R_{max\ difference}$ and ΔR represents the maximum difference between resistances as determined by two strain stages (stretching and releasing), the total change of the resistance, respectively. Fig 3.7 illustrates the relationship between the δh and the applied strain. As shown in Fig 3.7, the sensor exhibits a very low value of hysteresis below 5% in the strain range from 0 to 60% due to the excellent elastic recovery ability of PUY substrate and the stabilized rGO conductive layer by using PDA. With the further increase of strain, the δh value displays an increasing trend, which is probably attributed to the inherent viscoelastic nature of polymer substrate when the applied strain is beyond its elastic range. As for the linearity represented by the R^2 shown in Fig 3.7, it can be seen that the values of R^2 for the strain below 60% is as high as 0.999, which nearly presents a complete linear relationship. The high linearity makes the calibration process of data much easier, which is comparable with the capacitive-type strain sensors.^{1, 33, 40} Based on the above sensor performance, an appropriate working range of strain from 0 to 50% can be identified for the sensor wherein the sensor exhibits good sensitivity, very low hysteresis and almost complete linearity.

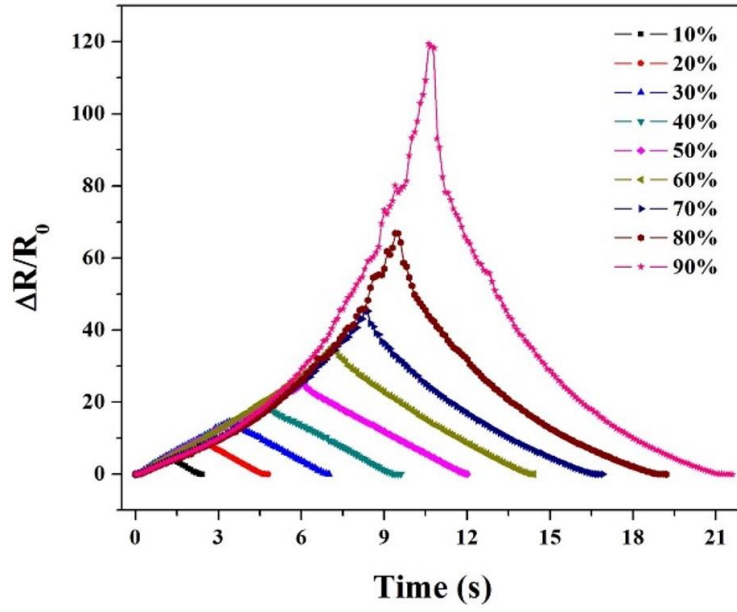


Fig 3.6 Electro-mechanical properties of the PDA/rGO/PUY strain sensor under different strains.

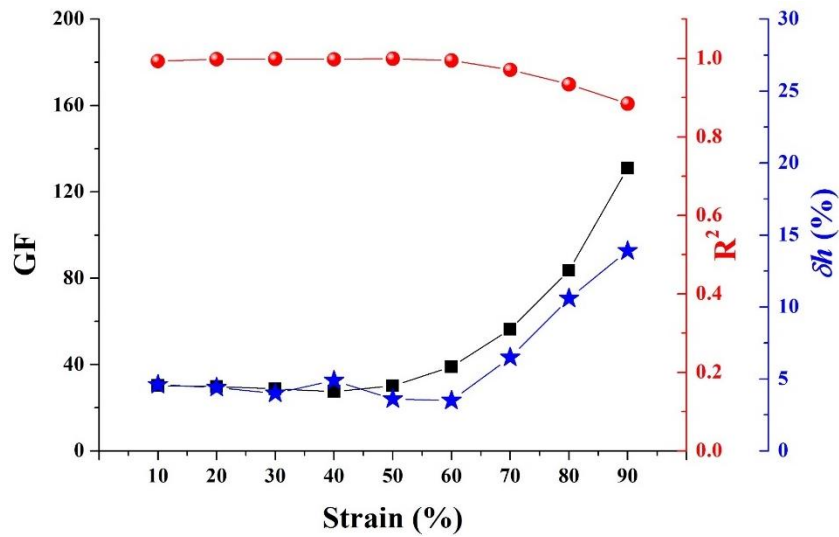


Fig 3.7 The development of GF, R^2 , and δh of the strain sensor under strains from 10% to 90%.

Fig 3.8 depicts the change of SEM morphologies of the sensor and the resultant strain-relative resistance change curve under the strain of 50%. It is clear that the resistance change comes from the cracks origination and propagation of the rGO layer. Owing to the different moduli between the rGO layer and elastic PUY, the outer rGO layer cannot deform in line with the PUY, thus cracks appear and their size and number increase with the increase of strain, leading to the increase of resistance. Based on the equivalent circuit unit of the model in Fig 3.9, a simple model can be applied to clarify this sensing behavior. The sensor is composed by numerous circuit units, and the total resistance of one circuit unit can be calculated as below:

$$R = \frac{R_a R_c + 2R_a R_b + R_b R_c}{R_a + 2R_c + R_b} \quad (2)$$

where R_a , R_b , and R_c represents the resistances of the rGO island, gap, and connection between two contacting rGO islands, respectively. The increased resistance upon stretching should come from the increased values of R_a , R_b , and R_c . Moreover, at a large strain, R_b is greatly increased, and the equation (2) can be simplified as $R = 2R_a + R_c$. Because of the excellent elasticity of PUY substrate, the enhanced interaction between PUY core and conductive rGO sheath, stability of sensing layer and integrality of sensor, the cracks originate and propagate uniformly in a linear relationship in the stretching process and return to its original pattern almost in the releasing course. Consequently, in the strain range of 0-50%, the sensor presents a very high linearity and slight hysteresis behavior.

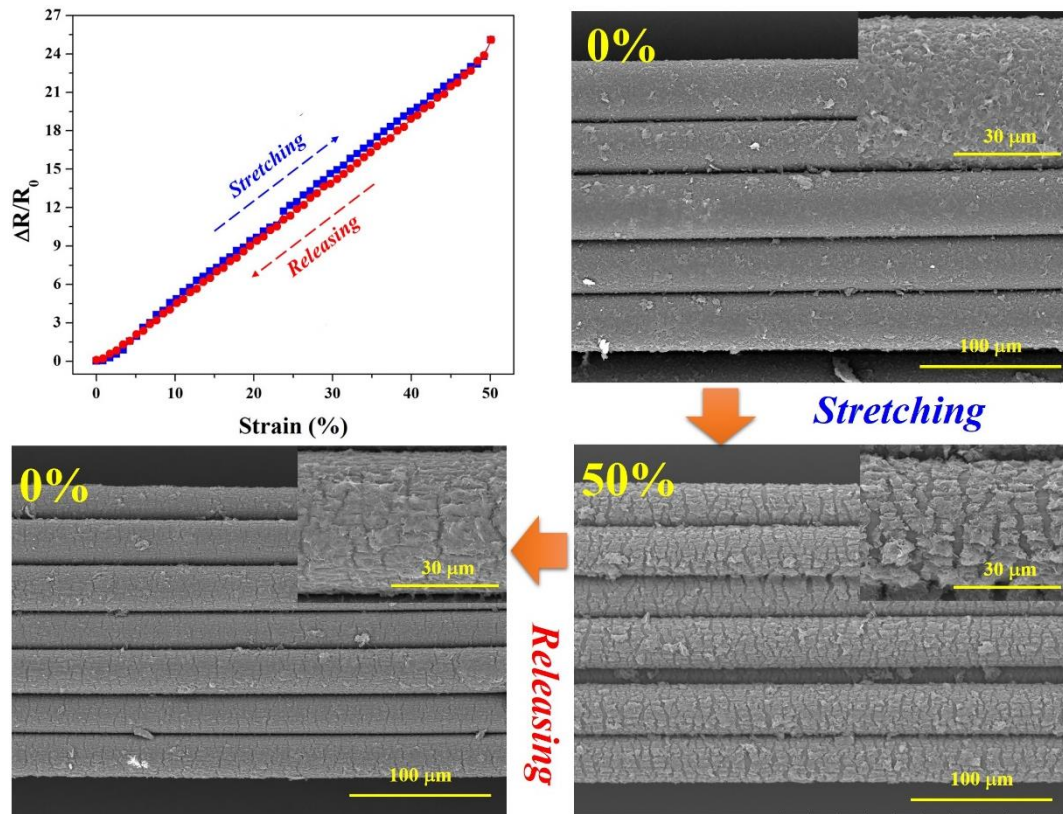


Fig 3.8 Resistance change versus a strain of 50%, and SEM images showing the surface morphologies' change during the stretching and releasing of the sensor.

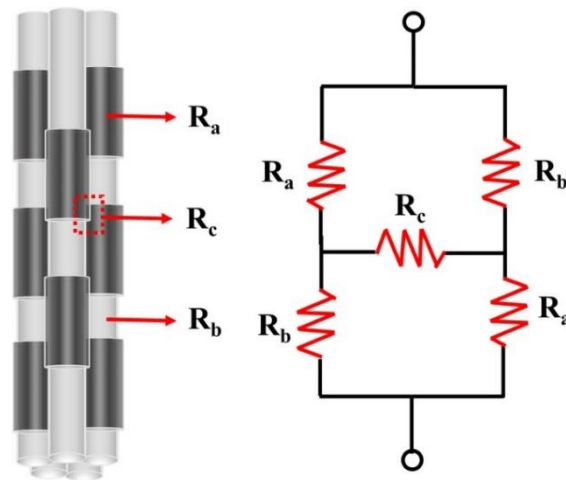


Fig 3.9 Schematic illustrations showing the resistance model of the sensor and the equivalent circuit.

CHAPTER 3

In addition, the improvement effect of PDA on the stability and durability of the sensor was demonstrated. It is known that the cyclic durability is of great importance for practical application, particularly for long-term monitoring. Thereby, considering the critical movement strain of human motion to be about 50% [158], the stability and durability of as-prepared sensor was evaluated under the applied strain of 50% and stretching speed of 100 mm min^{-1} . As displayed in Fig 3.10, it is obvious that the PDA/rGO/PUY sensor exhibits very stable and reliable performance even after 30000 stretching-releasing cycles. Such excellent durability greatly assures the effective working of the sensor in the potential applications. As reported in most literatures, the durability testing always stays at the level of only 10^3 [24,46,65,119,151]. However, the introduction of PDA as a strong adhesive and good wrapping package material for sensor fabrication in this study substantially enhanced the connection between PUY core and rGO sheath as well as multiple-layered rGO sheath itself of the sensor, thus ensuring to obtain a much higher durability than that of most reported strain sensors.

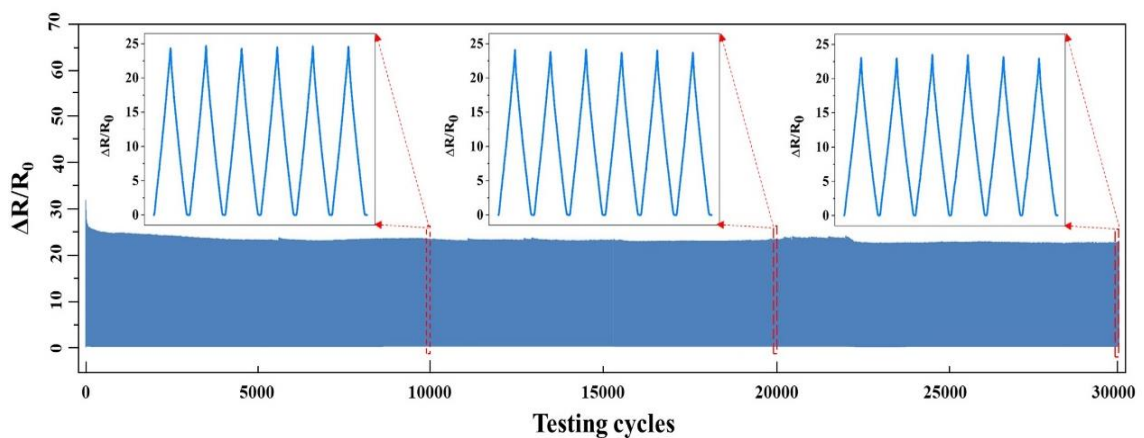


Fig 3.10 Durability of the PDA/rGO/PUY sensor undergoing the stretching-releasing cycles of 30000 (under the strain of 50% and stretching-releasing speed of 100 mm min⁻¹).

The electro-mechanical properties of sensor were further evaluated in terms of the response to stretching-releasing speed of applied strain. Fig 3.11 presents the resistance change-strain relationship and the response to the different stretching-releasing speeds at a strain of 50%. It can be seen that the sensor exhibits very stable sensing performance from low to high stretching-releasing speeds ranging from 10 mm/min to 400 mm/min. The peak variations of the electrical resistance are almost the same despite the increase of speed. Fig 3.12 shows that the response and recovery time of the two yarn sensors, which are 57 ms and 175 ms for rGO/PUY, and 60 ms and 168 ms for PDA/rGO/PUY, respectively. The results prove that the sensor can respond precisely and rapidly to the external strain with varied speeds. Moreover, the PDA encapsulation has little effect on the response/recovery time. The significantly improved durability and stability come from the good elasticity of PUY and strong stabilization of PDA layer. The good elasticity makes the PUY can keep abreast of the external strain, while the tight package of PDA guarantees the synchronous deformation of rGO layer with the PUY without notable delay.

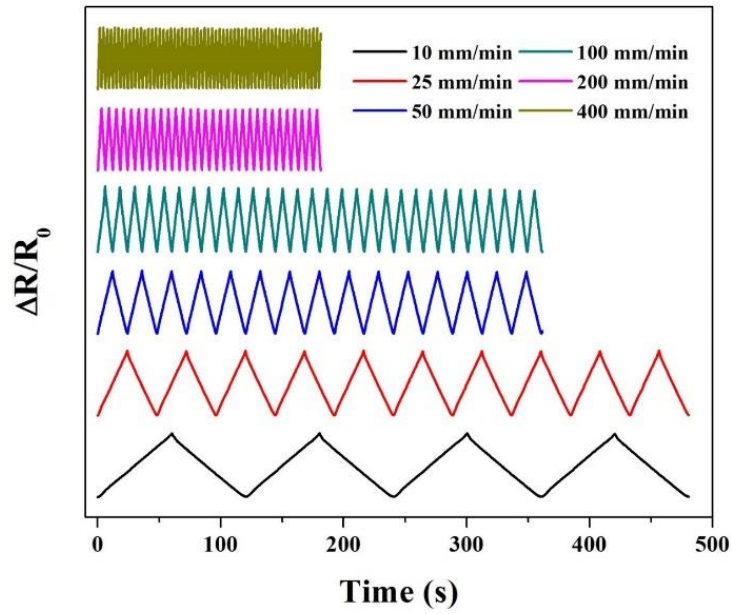


Fig 3.11 The electro-mechanical properties of the PDA/rGO/PUY sensor under varied stretching-releasing speeds at a strain of 50%.

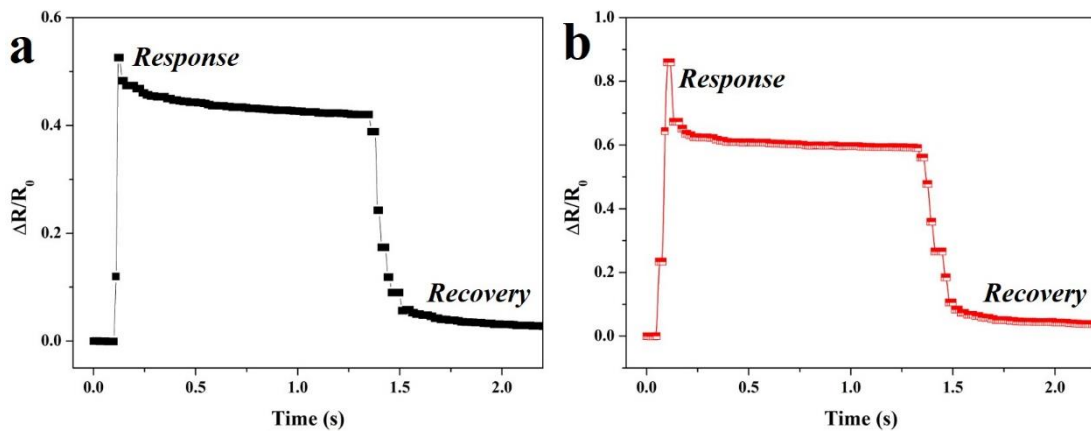


Fig 3.12 The response and recovery curves of (a) rGO/PUY and (b) PDA/rGO/PUY under a small strain of 5% and a testing speed of 600 mm/min.

The importance of the PDA layer can also be well proved in contrast with the unpacked rGO/PUY sensor. As shown in Fig 3.13a the relative resistance change of the

PDA/rGO/PUY sensor is considerably greater than that of rGO/PUY sensor, indicating a much higher sensitivity. Moreover, the former shows a linear relationship between the resistance-change and applied strain but the latter displays a nonlinear sensing behavior.

Fig 3.13b compares the sensing performance of these two sensors. Clearly, the properties of the PDA enhanced sensor are much superior to the untreated one, in terms of sensitivity, linearity, hysteresis and durability. The influence of sweat on the sensing performance of the yarn sensor was preliminarily examined, as shown in Fig 3.14. It is

easy to see that after dipping in sweat, the sensing yarn can still perform well and stably (Fig 3.14a). In Fig 3.14b, a slight GF decrement of 7.5% can be observed after the sweat dipping. This phenomenon may arise from the possible corrosion of urea, NaCl, and lactic acid in the sweat on the used Cu wires.

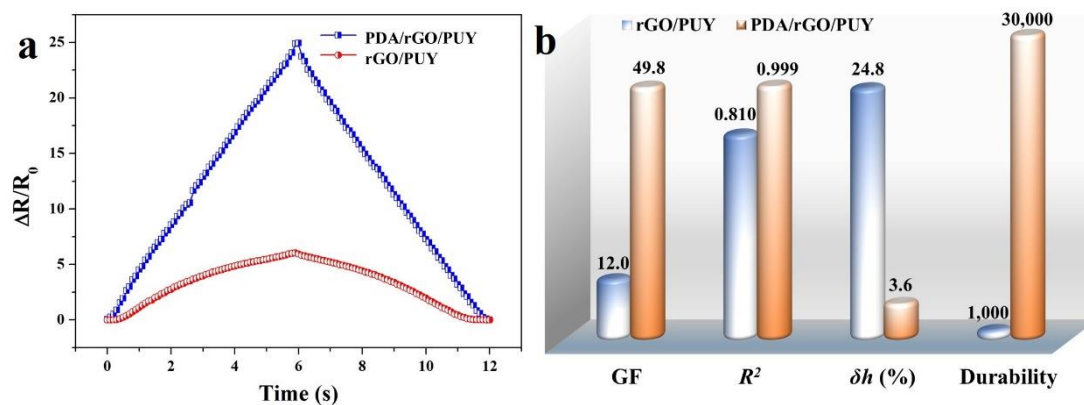


Fig 3.13 (a) Comparison on the resistance-strain curves between rGO/PUY and PDA/rGO/PUY sensors. (b) Comparison of sensing properties, in terms of GF, R^2 , δh , and durability between rGO/PUY and PDA/rGO/PUY sensors.

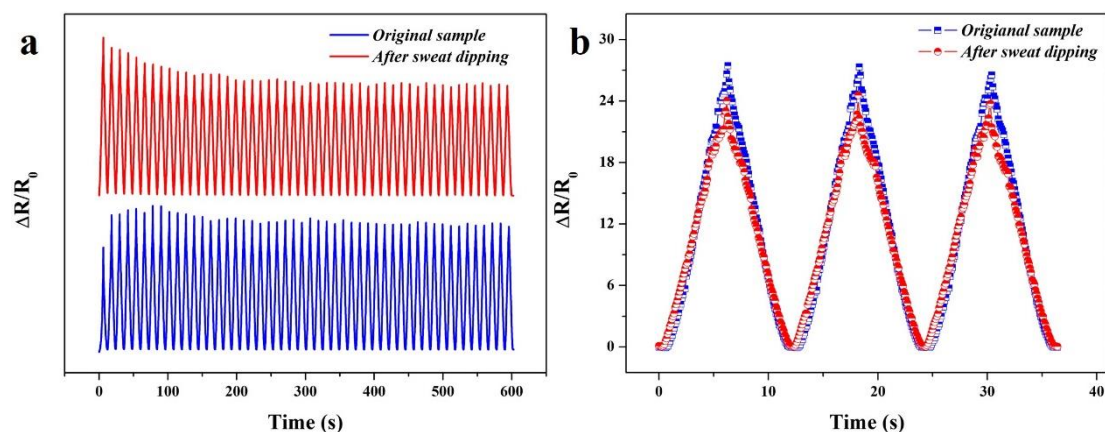


Fig 3.14 Electro-mechanical curves of the sensing yarn before and after sweat dipping.

(a) 50 cycles. (b) 3 cycles. (For the effect of sweat, the sensing yarn was dipped into an artificial sweat (pH 8.0) for 30 min at room temperature, and then the sensor was cleaned by deionized water and fully dried in the air.)

3.4 Conclusions

In this chapter, a new 1D coaxial yarn strain sensor was successfully prepared, which consists of elastic PUY core, rGO conductive sheath and PDA package layers. The SEM and FTIR results demonstrate that the dopamine molecules can reach the exposed rGO surface and self-polymerize into a continuous PDA film, thus greatly enhance the interfacial adhesion between PUY core and rGO sheath, stability of sensing layer as well as integrity of sensor. Consequently, the yarn sensor exhibits high sensitivity, excellent linearity and very low hysteresis behavior, especially the superior durability up to 30000 stretching-releasing cycles.

CHAPTER 4: Study of the Sensing Mechanism and Effects of Prestretching and Applied Bending on the Sensing Properties of One-Dimensional Strain Sensor

4.1 Introduction

It is known that the sensing mechanism plays a vital role in determining the sensing performance of a strain sensor. According to the above-mentioned review in chapter 2, the sensing mechanism varies with the different structures, which mainly includes the tunneling effect, piezoresistive effect, geometrical change and crack propagation [1,159]. However, due to limitations and difficulties of corresponding experimental equipment, the in-situ tracking and observation of the conductive networks under stretching is still quite challenging, which makes it hard to fully understand the sensing mechanism of strain sensors. As an alternative, computational simulation provides another effective way to further explore the inherent sensing mechanism behind the sensing behavior of flexible strain sensors.

Until now, different computational simulations have been reported to study the strain-response behavior of different flexible strain sensors. Three typical examples will be introduced to simulate the sensing behavior of zero-dimensional (0D) silver nanoparticles (AgNPs), one-dimensional (1D) silver nanowires (AgNWs), and two-

dimensional (2D) graphene based flexible strain sensors. First, Lee et al [160] studied the sensing behavior of AgNPs coated PDMS film by molecular dynamics based numerical simulation. In details, the adhesion between two AgNPs, and adhesion between AgNPs and PDMS substrate was assumed as elastic bonds with a maximum allowable strain, hence the disconnection between AgNPs will occur under increasing strain, resulting in the generation of cracks on the conductive layer and resistance change. The molecular could well predict the opening and closing of cracks on the conductive layer during stretching and releasing tests, and it was further demonstrated that initially generated cracks in advance can help facilitate the following cracks generation, benefiting higher sensitivity. Second, Amjadi et al [30] prepared conductive composites based on AgNWs filled polydimethylsiloxane (PDMS), and numerical simulation was further applied to study the piezoresistivity of the strain sensor. By setting up a three-dimensional (3D) resistor model with randomly distributed AgNWs in PDMS, the junctions between two adjacent AgNWs were classified as complete connection, fully disconnected, and partly connected by tunneling current. The simulation results agreed well with the experimental results, and proved that the emergency of bottleneck are responsible for the resistance change and nonlinear behavior. On this basis, the aspect ratio of AgNWs could be used to manipulate the conductive network by controlling the AgNWs junctions. Third, Hempel et al [77] fabricated a graphene-based strain sensor by spraying coating. By calculating the contact resistance between overlapped graphene flakes and in-flake resistance, the

voltage drop across the percolating graphene network was successfully simulated at different strains, verifying that lower graphene density prefers higher sensitivity.

In this chapter, the effect of cracks on the resistance change of the yarn strain sensor was studied and simulated by a finite element analysis (FEA) model. It is known that the sensing mechanism of the as-made 1D polydopamine/reduced graphene oxide/polyurethane yarn (PDA/rGO/PUY) strain sensor lies in the crack formation of the conductive graphene layer under the applied strain. However, a direct relation or proof is still missing between the cracks and resistance of the strain sensor. Therefore, the cracks of the yarn strain sensor under different strains were recorded by scanning electron microscope (SEM), and then a voltage drop was simulated based on the binarized SEM images to investigate the effects of cracks on the current flow. Furthermore, prestretching was applied to generate the cracks in the conductive layer and further stabilize the resultant conductive path, and thus enhance the electro-mechanical properties of the yarn strain sensor. At last, the capability of the yarn strain sensor to detect bending-induced strain was also successfully demonstrated.

4.2 Experimental Section

4.2.1 Characterization

Scanning electron microscope (SEM, TM3000, Hitachi, Japan) was used to track the cracks morphology change of the yarn sensor under different strain. The uniaxial

stretching and bending tests were precisely controlled by using an Instron universal test instrument (Model 5944, Instron Instruments, USA), and meanwhile a multimeter (Model 2010, Keithley, USA) was coupled to real-time record the resistance change of the yarn sensor. Moreover, for the bending test, the yarn strain sensor was clamped by a home-made fixture, and a polyformaldehyde pressure head with radius of 15 mm was used to apply pressure to the yarn strain sensor, thus generating bending.

4.2.2 Finite element analysis

To analyze the effect of cracks on resistance change, a finite element analysis (FEA) model based on COMSOL Multiphysics software was put forward to simulate the voltage distribution, where a voltage of 1V was applied on both sides of the binarized SEM images of the yarn strain sensor at different strains.

4.3 Results and Discussion

4.3.1 Sensing mechanism of one-dimensional yarn strain sensor

As displayed in Fig 4.1, the surface morphology of conductive rGO layer of the yarn strain sensor, under different strain from 0% to 50%, was tracked to clarify the evolution of the conductive rGO network, as well as the crack-based strain sensing mechanism.

At the initial state of 0% strain, the rGO flakes overlap with each other and wrap tightly on the PUY surface with the aid of PDA encapsulation, constituting a perfect and uniform conductive network. Nevertheless, damage or deformation will appear on the rGO conductive network when applied with stretching strain. When the applied strain is relatively small as 10%, the separation between the rGO flakes can be clearly observed, leading to the formation of long and narrow crack strips perpendicular to the stretching direction. When the strain is further increased to 20%, the number of cracks greatly increase, and at the same time, the width of the cracks also present an enlargement. At a middle strain of 30%, one can find that the deformation of the rGO conductive layer mainly lies in the increasing of cracks width along the stretching direction, while the density of cracks almost keeps unchanged. When the strain is further increased to 40% and 50%, it can be observed that there is little change of the crack dimension along the stretching direction, but the cracks grow in the perpendicular direction. As a result, some cracks will merge together to form much bigger cracks, with the width of about 2.3 μm . Moreover, it is of great interest to find that wavy wrinkles also occur on the remaining rGO island, with groove horizontal to the stretching direction. This special phenomenon should come from the positive Poisson's ratio of flexible PUY substrate. Generally, when a material with a positive Poisson's ratio is stretched, such as the PUY herein, the material will be stretched to longer along the stretching direction, but compressed to be shorter in the transverse direction. Therefore, at large strains $\geq 40\%$, the compression in the transverse direction becomes

large enough to induce the folding of conductive rGO layer. The gradually increased cracks under strain will definitely reduce the conducting path for current flow, leading to increased resistance as electrical signal for the strain detection.

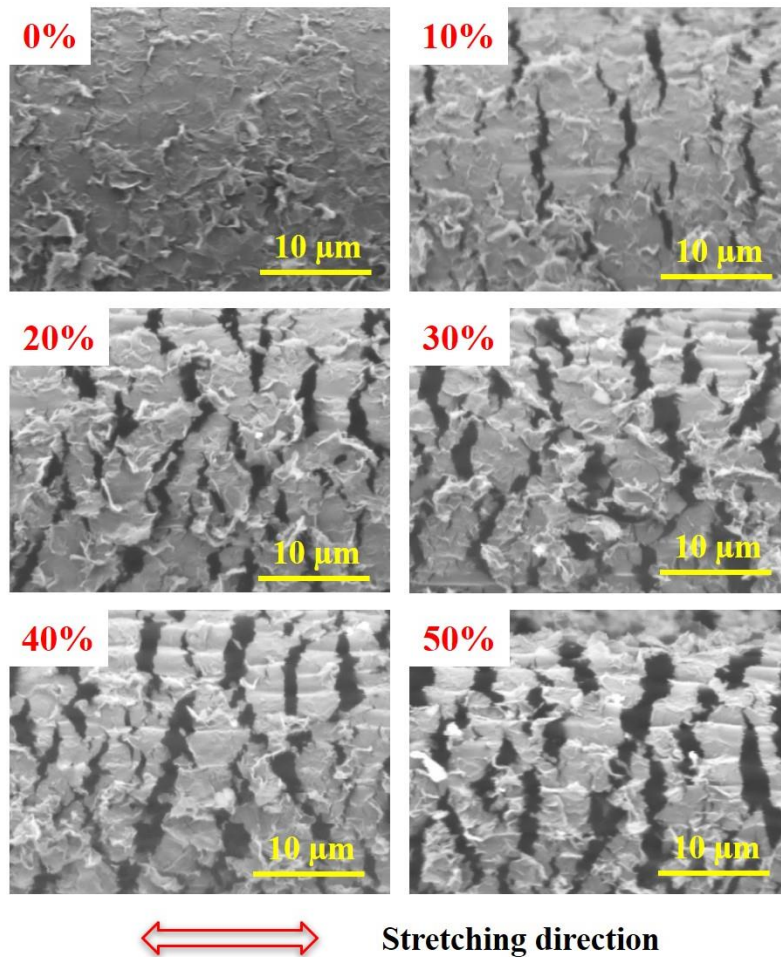


Fig 4.1 SEM images of the yarn strain sensor at strains from 0% to 50%, and the stretching direction is horizontal.

Fig 4.2 further illustrates the crack percentage under different strains, and meanwhile the relative resistance change versus strain was compared to verify the crack-based

sensing mechanism. It can be seen that with the increasing of applied strain, both the crack percentage and resistance present an increasing trend, suggesting that the inherent relationship between the resistance change and cracks. However, the crack percentage versus strain curve displays two stages with different slopes, i.e., the cracks area increase quickly at the strain of 0-20%, but slowly at the bigger strain of 20-50%, while the curve of relative resistance change keeps an almost linear behavior. This discrepancy was also reported by some other research works [133,161]. For example, Zhou et al fabricated a strain sensor by spray-coating carbon nanotubes (CNTs) onto electrospun PU mat, and it was found that the cracks increase linearly at strains of 0-300%, but the resistance change curve showed three distinct stages with gauge factor of 428.5 at strains of 0-100%, 9268.8 at strains of 100-225%, and 83982.8 at strains of 220-300%.

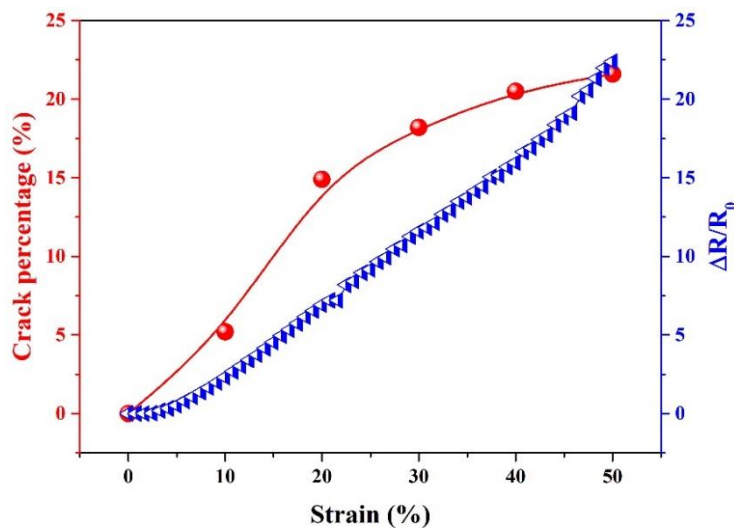


Fig 4.2 The relationship curves between the crack percentage and relative resistance change with the applied strain.

In combination with the SEM morphologies in Fig 4.1, three possible reasons may account for the discrepancy. First, the view range of the SEM maybe a little small to present the whole morphology of the yarn strain sensor. Second, the yarn used actually consists multi fibers, and the influence of contact resistance between neighboring conductive fibers are not taken into consideration for the resistance change. Third, it is worth noting that the growth of the cracks is not fully ideal to propagate only along the stretching direction. In fact, as shown in Fig 4.1, the angle between the crack outlines with the stretching direction deviates from hypothetical 90°. Besides the percentages of cracks, it is believed that the distribution of cracks also plays an important role in determining the resistance change. As illustrated by equation (1), under a certain length (L) and electrical resistivity (ρ), the resistance (R) of the conductive rGO layer is inversely proportional to the area in cross-section (S), where bigger S means wider path for current flow and thus lower R .

$$R = \rho \frac{L}{S} \quad (1)$$

Fig 4.3 illustrates the effect of different cracks distribution on the current flow, in which the crack percentage keeps same of 33% for all the cases. Ideally, without cracks in Fig 4.3a, the current can flow smoothly through the conductive layer without any obstruction. As seen in Fig 4.3b, when the cracks are distributed uniformly along both the horizontal and vertical directions, the current will pass through the spaces between the cracks, but the zigzag path will increase the passing time, which also suggests larger

resistance. However, if the cracks mainly appear along the vertical direction, the spaces between the cracks for current flow become narrower, indicating that the different distribution of cracks along the horizontal and vertical directions will also affect the current flow path. Fig 4.3d and 4.3e are two extreme situations, where the cracks ideally align along the horizontal or vertical direction, respectively. In the case of horizontal distribution in Fig 4.3d, only the cross-sectional area is decreased, while the flow path is still the shortest. In clear contrast, when the cracks occupy the whole vertical direction, the current flow is completely blocked. Fig 4.3f is the situation of cracks distribution, which is the most similar to the real SEM morphologies as shown in Fig 4.1. The cracks prefer propagating along the vertical direction, but at the same time with some degree inclination. Based on the above discussion, it can be concluded that the crack percentage is not the only impact factor to determine the resistance change, and some more factors like the cracks distribution should also be taken into consideration.

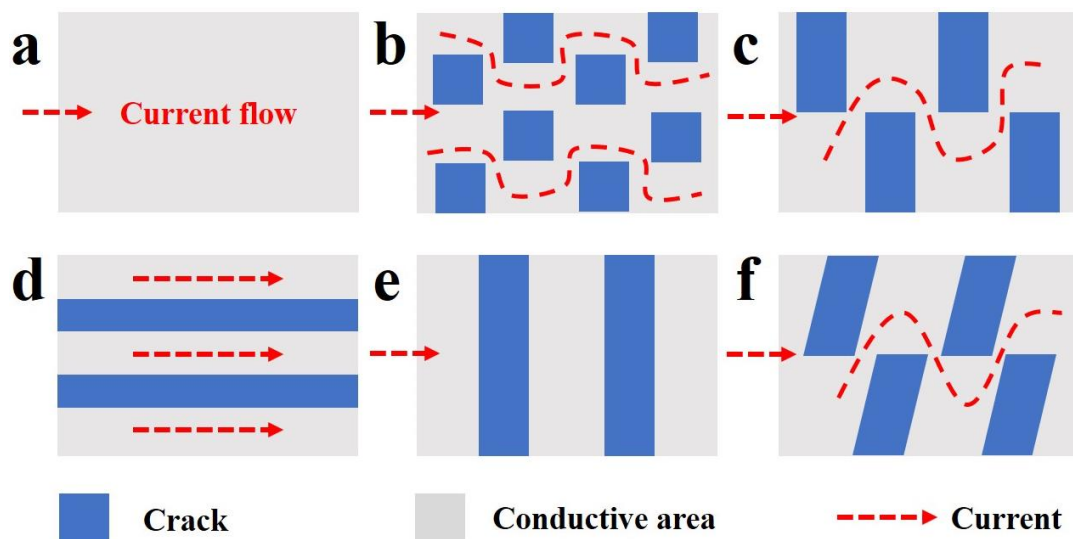


Fig 4.3 Scheme showing the effect of different crack models on the current flow of conductive rGO layer.

To obtain a direct result of the cracks effect on the current flow or electrical resistance.

A FEA was further put forward to simulate the voltage drop based on the SEM images.

Fig 4.4 shows the detailed procedures of FEA simulation. At first, the original SEM image is vectorized and transformed to a binary image, where the cracks profiles are abstracted for further simulation as shown in Fig 4.4b. Fig 4.4c shows the applied boundary conditions, where the voltages of the left side and right side are defined as 1V and 0V, and the up and down sides are considered as insulative. The continuity condition or calculation method is based on node current law (KCL) proposed by Kirchhoff, that is the current flowing into one unit is equal to the current flowing out as shown in Fig 4.4d. The method details can be found in Fig 4.5. The voltage and current for unit (i,j) is defined as $V_{i,j}$ and $I_{i,j}$. In accordance with KCL, $I_{i,j}$ can be expressed by equation (2) and (3) as follows:

$$I_{i,j} = \left(\sigma_{i,j-1} \frac{V_{i,j-1} - V_{i,j}}{\Delta x} + \sigma_{i,j+1} \frac{V_{i,j+1} - V_{i,j}}{\Delta x} \right) (\Delta y \times d) + \left(\sigma_{i-1,j} \frac{V_{i-1,j} - V_{i,j}}{\Delta y} + \sigma_{i+1,j} \frac{V_{i+1,j} - V_{i,j}}{\Delta y} \right) (\Delta x \times d) = 0 \quad (2)$$

$$\sigma_{i,j} = \begin{cases} 1000 \text{ S/m, if unit}(i,j) \text{ is rGO} \\ 10^{-6} \text{ S/m, if unit}(i,j) \text{ is a crack} \end{cases} \quad (3)$$

Where σ refers to the electrical conductivity, Δx and Δy are the unit dimensions, d

presents the thickness of rGO layer, respectively. Moreover, the conductivity of the rGO island and crack is defined as 1000 S/m and 10^{-6} S/m, respectively. By solving this equation, the value of $V_{i,j}$ can be obtained. Since the current is considered as uniform, the resistance distribution can be reflected from the voltage distribution or drop according to the ohm's law. After meshing in Fig4.4e, one can obtain the final simulation results that show the voltage drop.

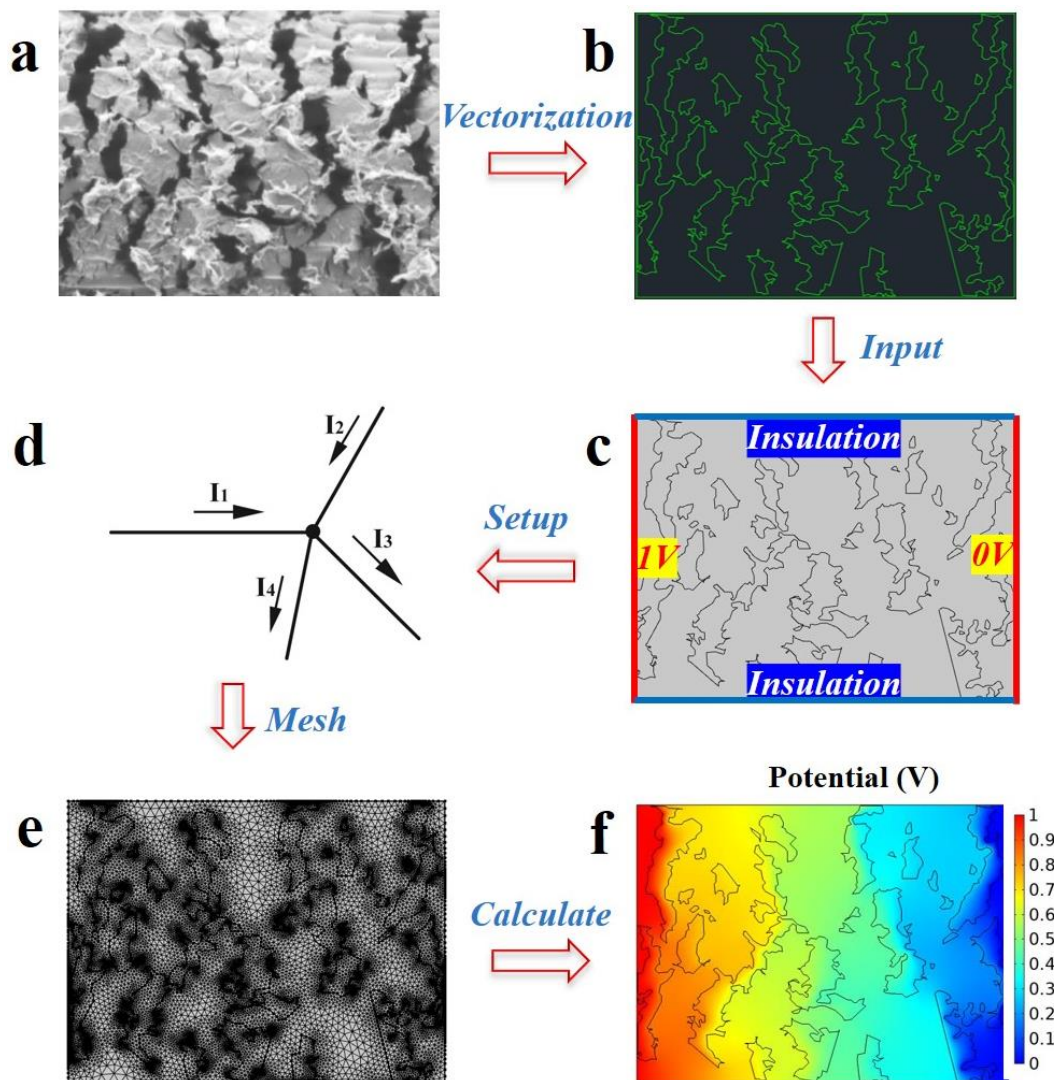


Fig 4.4 Flow chart of the voltage drop simulation process: (a) original SEM image. (b)

binarized SEM image by vectorization. (c) boundary conditions applied. (d) simulation method of KCL. (e) image after meshing. (f) calculated results of potential distribution.

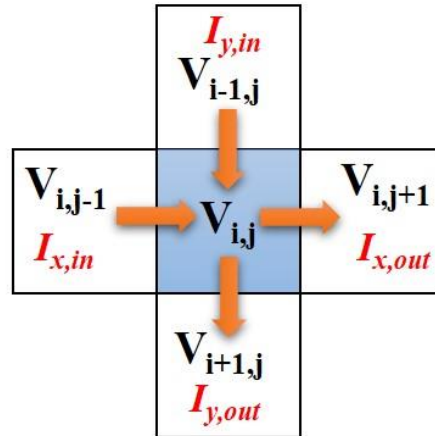


Fig 4.5 Current flow of unit $V_{i,j}$ with the neighboring units.

Fig 4.6 displays the simulated results of conductive rGO layer under different strains.

At the initial state of zero cracks, the voltage drop is gradual and uniform from left to right, indicating the homogenous resistance. When applied with strain, cracks appear and it is clear that the voltage distribution around the cracks drops much faster than the uniform parts, suggesting a larger resistance of the generated cracks under stretching.

Moreover, with the further increasing of strain, there occur more cracks, and the voltage distribution becomes more nonuniform, further proving the great effect of crack on electrical resistance of the conductive rGO layer. The effect of cracks on resistance can be intuitively understood as follows: under stretching larger cracks in the conductive rGO networks greatly reduce the pathway for current flow and thus increase the

resistance. Therefore, from these simulation results it can be safely concluded that the cracks generated under stretching strain can greatly reduce the current flow path, leading to the resistance change, which is in perfect agreement with the experimental results of resistance change as shown in Fig 4.1.

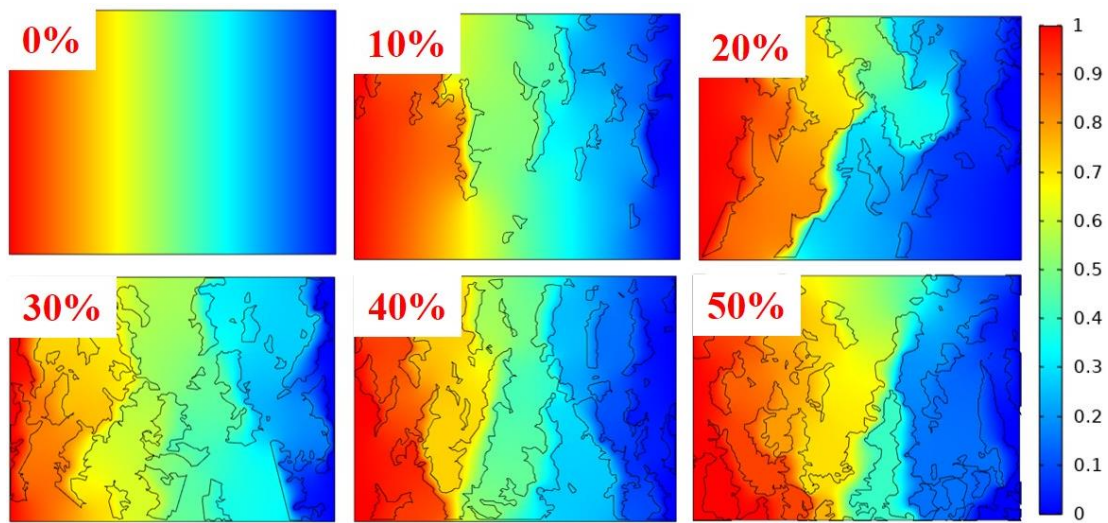


Fig 4.6 Simulated potential distribution of the SEM images in Fig 4.1.

4.3.2 Effect of prestretching on the electro-mechanical properties of yarn sensor

From the findings of past studies [1,46,83,133,151], the crack open-close is one of the main sensing mechanisms for as-fabricated piezoresistive sensor wherein its sensing mechanism lies on the relationship between the formation and propagation of microcracks within the conductive yarn sheath layer and the corresponding change of electronic resistance of the sensor with the variation of applied strain. Therefore, how to create a stable and recoverable microcrack pattern in the conductive layer, i.e. the

conductive path, plays a crucial role in generating the desired properties of sensor. One of the feasible and effective approaches are to carry out a prestretching treatment on the sensor to facilitate the formation of microcrack pattern, in which the applied strain and number of applied stretching-releasing cycles are two main parameters. In this study, based on our preliminary experiments, the pre-stretching-releasing cycle was fixed at 100 cycles. Then the effect of applied strain on the electro-mechanical properties was investigated in order to identify an appropriate applied strain on the sensor for this prestretching treatment. As shown in Fig 4.7a, without prestretching, the resistance-time curve of sensor displays a declining trend with the increase of testing cycles. The possible reason is that the microcracks appear and propagate within the sensing layer when the initial stretching-releasing cycles is applied on the sensor but the fixed crack pattern is probably not formed in the initial a number of stretching-releasing cycles. Fig 4.7b show the relative resistance change curves during the stretching-releasing cycle under different applied prestretching strains and the resultant sensing properties-strain curves, respectively.

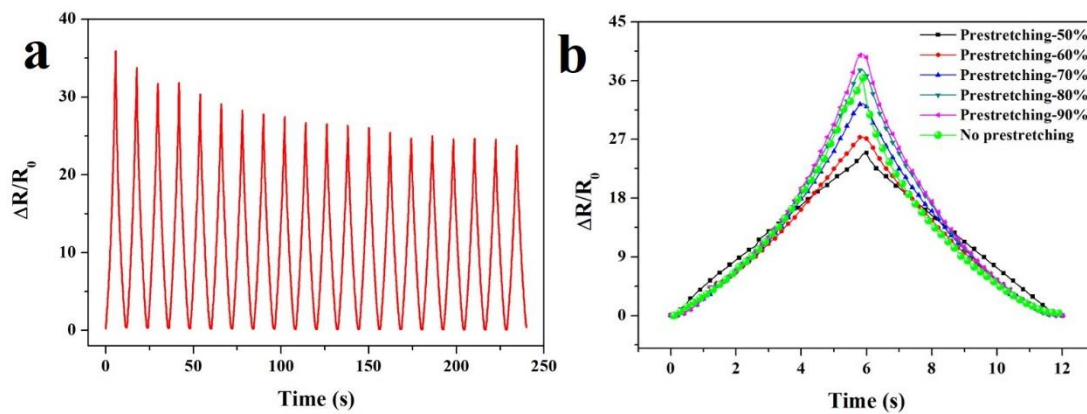
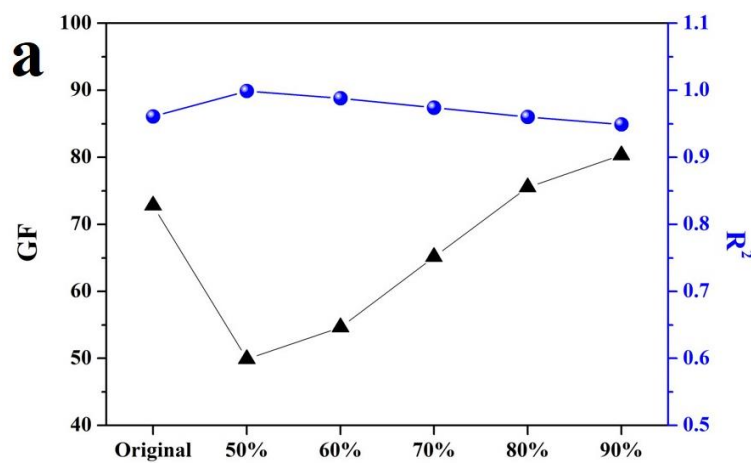


Fig 4.7 (a) Initial resistance change curve of 20 cycles at a strain of 50% without prestretching. (b) Resistance change–strain relationship at a strain of 50% after prestretching at different strains.

Although the sensor without prestretching shows a higher resistance change and GF (Fig 4.8a), this resistance change is unstable, showing much higher hysteresis and lower repeatability compared to the prestretched sensor (Fig 4.8b), where the repeatability of a sensor can be evaluated by repeatability error [96]. Besides, it can be found that the relative resistance change of prestretched sensors increases when the applied prestretching strain increases. From Fig 4.8, it is easy to see that the applied strain for the prestretching has a significant effect on the GF of the sensor wherein the GF greatly increases with the increase of prestretching strain. In terms of linearity, the value of R^2 exhibits a slightly variation with the increase of prestretching strain applied on the yarn strain sensor.



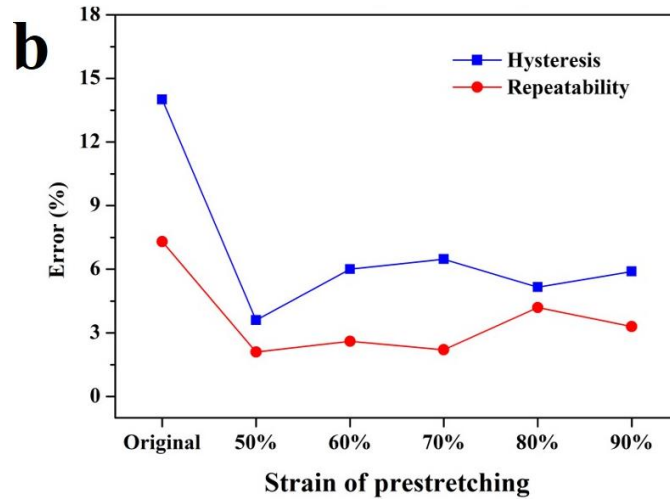


Fig 4.8 (a) GF and R^2 of the PDA/rGO/PUY sensor after prestretching at different strains. (b) Hysteresis and repeatability errors of the PDA/rGO/PUY sensor after prestretching at different strains.

In view of the crack-based sensing mechanism, the effect of prestretching can be explained by the scheme of sensing mechanism in Fig 4.9: there are three states for the rGO layer. Before stretching, the rGO layer is intact without any cracks, and the sensor possesses the minimum electronic resistance. When applied with prestretching at a designed strain, because of the positive Poisson's ratio of PUY, the sensor is stretched and compressed along the length and width direction, respectively. Due to the different modulus between the rGO layer and soft PUY, the microcracks appear and gradually grow up, resulting in denser and larger cracks with the increased strain. Meanwhile, the conductive pathway contracts and the following resistance change can be detected. After unloading the strain, the core of PUY is released to its original state, and thus the microcracks close again, meanwhile leaving some tiny cracks [46]. During the further

stretching, it becomes easier for sensing layer to expand along the previous tiny cracks. Consequently, the stable and recoverable microcrack pattern, i.e. conductive path, can be formed within the conductive layer by using such prestretching.

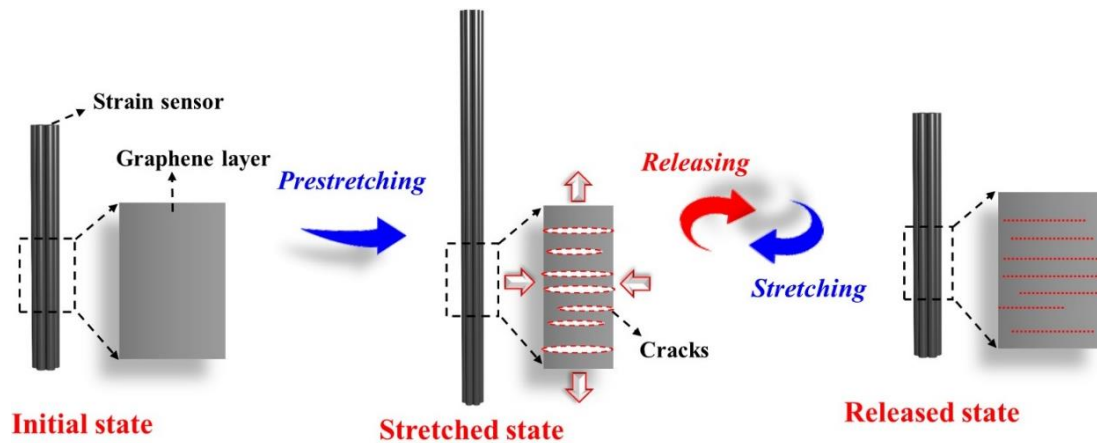


Fig 4.9 Scheme showing the sensing mechanism of the sensor.

4.3.3 Electro-mechanical properties of yarn sensor for sensing bending-induced strain

In the practical human motion detection, joint bending, such as the bending of finger, wrist, arm and leg, is one of the mostly common human movements. In this regard, the wearable sensing clothing or fabric worn on the human body as a human-worn material interface for human motion detection undergoes a combined deformation of bending and stretching. Therefore, to meet this requirement, the sensor developed should be able to sense not only the tensile strain as most reported strain sensors but also the bending-induced strain. Based on the crack open-close sensing mechanism, the as-fabricated

yarn sensor is expected to possess the capability of sensing the combining tensile- and bending-induced strains.

In order to examine the capability and performance of the sensor for sensing such multiple deformations, a test protocol was setup in our lab. As shown in Fig 4.10a, a home-made attachment was installed on an Instron machine to simulate parts of the body, where the sensor was fixed at two ends of a sample holder, and a pressure head moved down and up to generate deformation on the sensor. From Fig 4.10b, it is easy to see that the resistance-change increases dramatically and linearly with the increasing displacement of the pressure head, showing a big relative resistance change of 3.8 and a very high R^2 value of 0.993. Moreover, it is notable that the resistance change curve was recovered with very little hysteresis (δh of 3.1%) to the original state after releasing due to the PDA reinforced structure during bending.

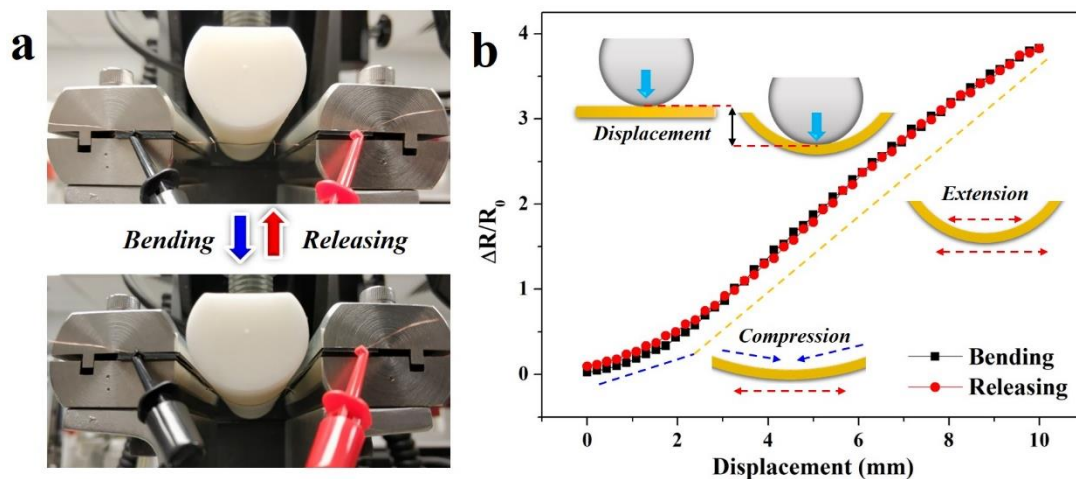


Fig 4.10 Bending properties of the sensor. (a) Photo of the experimental setup for

bending test (diameter of the pressure head is 30 mm). (b) Dependence of resistance change on displacement of the pressure head during bending and releasing (movement speed of the pressure head is 100 mm/min).

In details, it can be seen that the relative resistance change of sensor increases with the increase of the displacement of the pressure head on the sensor, i.e. the combining deformation induced by tension and bending. This phenomenon can be understood by the deformations of the two side parts of the sensor against the pressure head. When the press head moved downward, the outside part of yarn sensor bended outward, leading to the more and bigger-sized cracks formed and thus the increase of resistance. On the other side, the inside part of sensor was compressed and bended inward, which pushed the rGO of conductive layer to contact closely, thus resulting in a lowered resistance. When further increasing the displacement of press head, the cracks of outside part kept growing, while the major deformation of inside part probably turned into the extension, leading to the increase of cracks and the resultant resistance. Therefore, the resistance increase with the increased displacement is faster than that at the beginning of bending. In theory, the actual strain (ε) of the yarn sensor during bending process can be illustrated by Fig 4.11. According to the relationship between the pressure head's displacement (d) and radius (r), equations (4) and (5) can be used to describe the change of ε . The original length of the yarn strain sensor is defined as $2s$. When $d < r$, the contact length between the pressure head and strain sensor is very small, which can be

regarded as straight line for brevity. On the other hand, in the case of $d > r$, the arc angle degrees (2θ) will also contribute to the ε with increased d , thus generating higher resistance change. In Fig 4.10b, since the displacement of pressure head was 10 mm smaller than the radius of 15 mm, the resistance change of the yarn sensors present an almost linear behavior.

$$\varepsilon = \frac{\sqrt{s^2 + d^2}}{s} - 1 \quad (4)$$

$$\varepsilon = \frac{\sqrt{s^2 + d^2 - 2dr} + \theta r}{s} - 1 \quad (5)$$

The durability of sensor under such applied cyclic deformations was evaluated with the results shown in Fig 4.12. It can be seen that the resistance change curves remained stable after 5000 cycles' bending, showing a good durability of sensor.

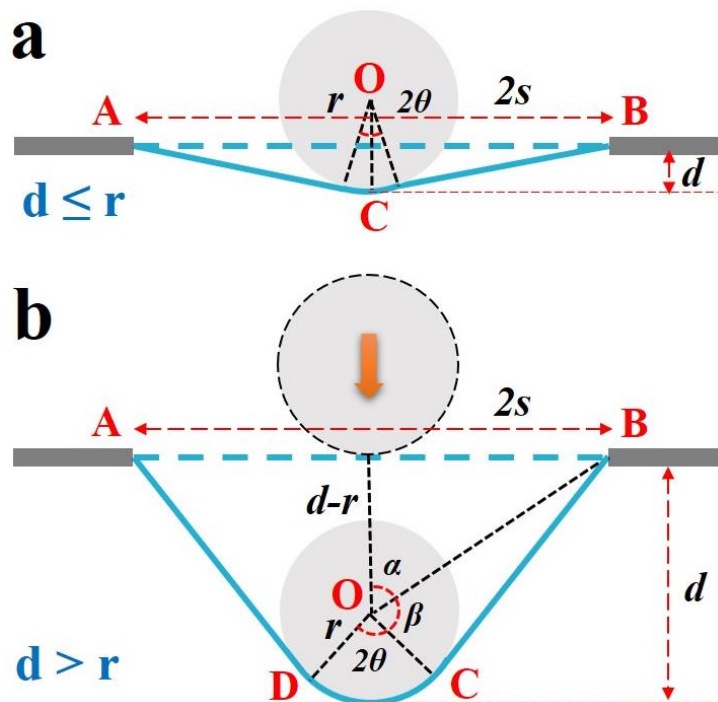


Fig 4.11 Scheme showing the two situations during the bending process of the strain sensor: (a) $d \leq r$ and (b) $d > r$.

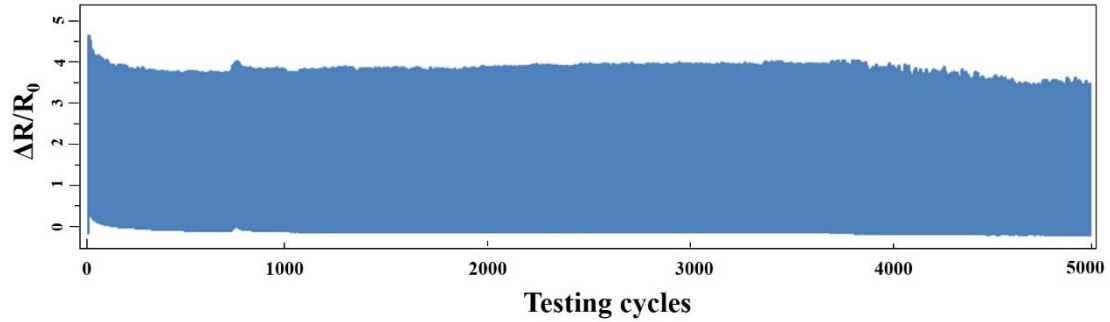


Fig 4.12 Cyclic stability test of compressive bending of the sensing (a) yarn and (b) fabric under the displacement of moving pressure head of 10 mm and the movement speed of pressure head of 100 mm/min.

Compared with other related state of the art 1D strain sensors (Table 4.1), the yarn-type strain sensor based on PDA/rGO/PUY developed in this study exhibits excellent sensing performance in terms of sensitivity, linearity, hysteresis and repeatability. Moreover, the sensor possesses superior durability up to 30000 cycles at 50% strain that is more than three times the durability of most reported 1D strain sensors. Furthermore, the PDA/rGO/PUY sensor is also capable of detecting multiple deformations.

Table 4.1 Performance comparisons to recently reported 1D strain sensors

Materials	GF @ strain	Durability (cycles @ strain)	Linearity	Hysteresis	Weavability	Sensing function	Ref
PDA/rGO/PU	50.0@50%	30000@50%	High	Low	High	Tension, Bending induced tension	This work
rGO/(PU/PE)	10@1% 3.7@50%	10000@30/50%	Nonlinear	High	N/A	Tension, bending, torsion	[97]
CNTs/PU	1.67@0-20% 1.24@20-100%	2000@50%	Nonlinear	N/A	N/A	Tension	[18]
AgNWs/ Polyolefin	13920@64%	4500@10%	Nonlinear	N/A	N/A	Tension	[149]
CNTs/PU	5@1500%	10@400%	Nonlinear	N/A	N/A	Tension	[162]
(CB/PDMS)- (AgNWs/nylon&PU)	~2.8@20% ~0.7@100%	N/A	Two linear ranges	Low	high	Tension, flexion, pressure	[163]
PEDOT/PE	0.76@20%	1000@20%	Nonlinear	N/A	N/A	Tension, pressure	[164]

Note: PE: polyester; GWF: graphene woven fabric.

4.4 Conclusions

In conclusion, the sensing mechanism of the as-made 1D PDA/rGO/PUY strain sensor was studied by recording the cracks morphologies under different strains by SEM, and then a FEA was conducted based on the SEM images to simulate the voltage drops of the strain sensors with different cracks under strains. It is confirmed that the resistance increase of the yarn strain sensor lies in the crack formation of the conductive graphene layer under applied strain. Furthermore, prestretching was demonstrated as an effective method to adjust the electro-mechanical properties of the yarn strain sensor, and larger prestretching strain benefits higher sensitivity, lower hysteresis and repeatability errors. Moreover, benefiting from the reasonable design of structure and material system, the yarn strain sensor is proved to possess a good capability to sense multiple mechanical deformations of stretching and bending.

CHAPTER 5: Wearable Fabric Sensor by Integrating the One-Dimensional Yarn Sensor into Fabric

5.1 Introduction

The history of human civilization is believed to be closely associated with the development of clothing, and the clothing technology made of various textiles is so closely contacted with the human body during the daily use and thus it is regarded as the second skin of human being. Moreover, being hierarchical fiber assemblies constituted from fiber to yarn and then fabric, the textiles possess many unique properties such as deformability, conformability, breathability, durability and washability. Therefore, the textile is considered as an ideal platform that can integrate diverse flexible electronic devices for developing textile-based wearable electronic systems to detect human motions and physiological information of human body [159,165-167].

To develop above-mentioned textile-based wearable electronic systems, sensing devices with matchable configuration and properties such as flexibility, stretchability and mechanical stability are indispensable elements for fabricating such systems, which should possess the capability to be integrated into the textile substrate, and thus endowing the systems with various sensing functions. In this regard, traditional bulky

and rigid metal- and semiconductor-based sensors are not suitable for the application due to their mismatchable conformation and poor mechanical compliance with the flexible and lightweight textiles and soft human body. With recent advances of micro/nano materials and fabrication technologies for sensors, various flexible and wearable film-based sensors with good sensing performance have been developed for the wearable applications. However, the majority of such sensing devices reported were fabricated in 2D planar configurations [24,28,119,141,151,158,168], which cannot be incorporated within the textile substrate and can only be attached on the surface of the textiles/clothing or directly pasted on the human skin. In such integrating ways with the textile/clothing or human body, even though the sensors have good flexibility, stretchability and sensing property, the integration of sensors greatly degraded not only the aesthetic appearance but also the inherent properties of textiles/clothing, including conformability, breathability and durability. Attaching the sensor to the skin may cause not only skin irritation but also the discomfort to the wearer. Especially, the wearable system fabricated by using these two approaches are unsuitable for the long-term monitoring. In contrast, 1D flexible sensor in a fiber/yarn-type configuration is a much better device for the textile-based wearable system [16,97,147,149,169], which can be easily woven and knitted into textile structures like common yarns for fabricating fabrics via existing textile technologies. Besides, the above-mentioned exceptional properties of textiles as well as comfort and aesthetic beauty of clothing can be maintained when the textile-based electronic system is fabricated through such a yarn-sensor integrating way.

In this chapter, the yarn sensor of PDA/rGO/PUY developed previously was successfully integrated into the woven structure by using a lab-based automatic weaving machine. The weaving process went smoothly, demonstrating an outstanding weavability of sensing yarns. The fabric sensor presents very good and stable sensing performance even after 10000 testing cycles, which can be achieved for the first time for such kinds of sensing textiles. Because of using such a yarn-sensor integrating way, the lightweight and small-sized yarn sensor can be incorporated into fabric structures like common weft yarns for fabricating the fabric sensors, without interfering with the unique properties of fabric as well as the comfort and aesthetic beauty of clothing. This shows great potential applications for long-term and real-time monitoring of human motions and physiological conditions.

5.2 Experimental Section

5.2.1 Preparation

The as-prepared PDA/rGO/PUY sensor was woven into the sateen structure using the weaving technology (CCI Rapier Weaving Machine). As shown in Fig 5.1a-c, the weaving machine mainly includes two parts: the weaving part and software controlling part. In consideration of its excellent stretchability, high elastic recovery, and good wearability, spandex/cotton core-spun yarn was selected as the weft yarn for producing

fabric substrates as shown in Fig 5.1d, where the spandex core provides the superior elasticity, and the cotton contributes to lengthen the service life and offer a soft hand feeling. Moreover, it is of significance that the stretchability of this yarn is comparable to that of the PUY based strain sensor of PDA/rGO/PUY, so that the PDA/rGO/PUY strain sensor can deform in step with the supporting fabric in the weft direction. Cotton ply yarn was used as the warp yarn because of its wide application, low cost, and prominent wearability. In order to easily distinguish these two yarns, different colors were applied: white for the spandex/cotton core-spun yarn, and blue for the cotton yarn. The yarn sensor was placed in the predesigned position along the weft direction as displayed in Fig 5.2, so that the 1D PDA/rGO/PUY yarn sensor can deform with the deformation of elastic fabric in weftwise. The fabric specifications can be found in Table 5.1.



Fig 5.1 Photographs showing (a) the weaving system. (b) the control software. (c) weaving process. (d) the obtained fabric during weaving.

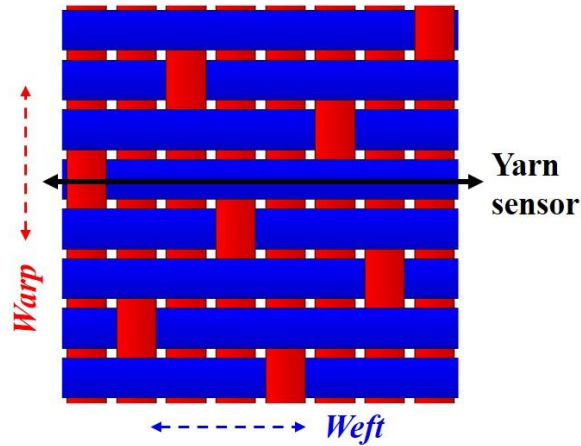


Fig 5.2 Architecture of sateen fabric with the black arrow for indicating the intended position for the yarn sensor

Table 5.1 Specifications of the sensing sateen fabric.

Weave repeat	Yarn count (Ne)		Fabric density (Threads cm ⁻¹)		Fabric cover factor (%)		
	Warp	Weft	Warp	Weft	Warp	Weft	Total
8 × 8	80/2	21	32	27	45	50.2	73

5.2.2 Characterization

For the electro-mechanical properties, the fabric strain sensor for testing has a size of about 100 mm length and 40 mm in width. The uniaxial stretching and bending tests were precisely controlled by using an Instron universal test instrument (Model 5944, Instron Instruments, USA), and meanwhile a multimeter (Model 2010, Keithley, USA) was coupled to real-time record the resistance change of the fabric strain sensor. To test the washability of the fabric sensor, the fabric sensor was firstly soaked into the

detergent solution for 2 min, where the solution contains 0.2 wt.% of 1993 AATCC Standard Reference Detergent. Then the solution was stirred at 27 °C and 200 r.p.m for 5 min to simulate the washing process. Thereafter, the fabric sensor was rinsed by cleaned water and fully dried in the ventilated hood at room temperature. The fabric cross-section for examining the yarn configuration under different strain were recorded by an optical microscope (Laica 130, Germany).

5.3 Results and Discussion

5.3.1 Fabrication of fabric sensors by weaving the 1D yarn sensor into fabric

As mentioned above, with exceptional properties and serving as a likely second human skin, the clothing made of fabrics with sensing functions is an ideal wearable electronic system for long-term monitoring of human motions and physiological conditions. In this regard, a new strain fabric sensor was fabricated by incorporating the as-prepared yarn sensor of PDA/rGO/PUY into the designed woven-based structure. During this process, the weavability of the 1D yarn sensor and the properties of the resultant 2D fabric sensor were examined. For a friendly contact with human skin, the PDA/rGO/PUY sensor was directly weaved into a fabric structure, where the sensing PUY replaced some of the weft yarns wherein the yarn sensors can be fixed by the binding points with the warps (Fig 5.3a). By using the existing weaving technologies

(Fig 5.3b), the 1D sensing yarn can be integrated into the 2D fabric along the weft direction, finally forming a fabric sensor (Fig 5.3c). As displayed in Fig 5.2, a 2D sateen structure was specially designed for the fabric sensor. This structure is characterized by the longer yarn floats and less binding points between warps and wefts, which can reduce the friction between warps, wefts and the integrated yarn sensor, thus improving the linearity, lowering the hysteresis and enhancing the repeatability of the fabric sensor. Based on this structure, the fabric sensor was fabricated by using the cotton yarn as warp and elastic cotton/spandex yarn as weft as well as the yarn sensor as a replaced weft yarn via a lab-based automatic weaving machine. Moreover, the PDA encapsulation is also considered to play an important role, which protects the rGO layer from detaching under intense mechanical striking during the weaving process, finally guaranteeing the well reserved sensing performance. In Fig 5.3c, it can be seen that the yarn sensor was successfully integrated into the fabric, meanwhile without any damage.

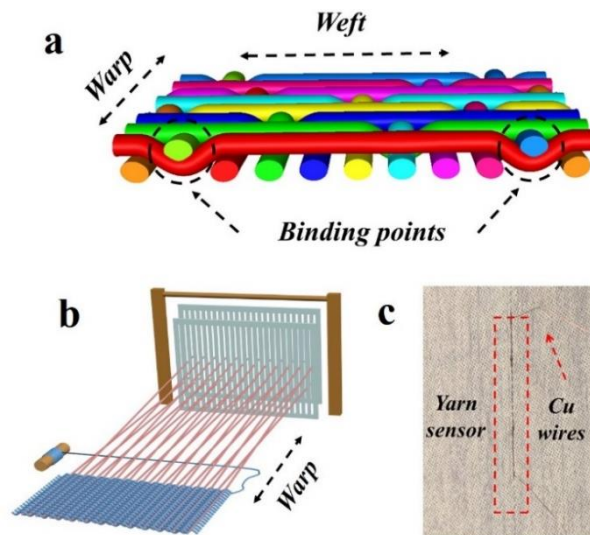


Fig 5.3 (a) Fabric structure for integrating the sensing yarn. (b) Scheme of the weaving

process. (c) Photo of the fabric sensor.

5.3.2 Electromechanical properties of the fabric sensor

Compared with the fabric, the yarn sensor is much smaller in size and lightweight with a weight of 0.15 mg/cm, showing a negligible effect on the intrinsic properties and aesthetic feeling of the fabric/clothing. The electromechanical properties were evaluated with the results shown in Fig 5.4. It can be seen that the fabric sensor can respond well to the external strain, showing a good GF of 25.3, a very high linearity with a R^2 value of 0.981 and an acceptable value of hysteresis error of 14.4%. Moreover, from Fig 5.4b, it can be observed that the response of the fabric sensor to applied strain can be divided into two parts: at strains of 0-10%, the relative resistance change shows a very small value of less than 1%, suggesting that the actual extension of the inserted yarn sensor is too small to induce the crack generation of conductive rGO layer when the fabric is applied with an external strain of less than 10%. This phenomenon should come from the fixture status of the yarn sensor in the fabric structure, that is, the small external strain cannot be efficiently transferred from the fabric to the yarn sensor, which will be discussed in details hereinafter. On the other hand, when the applied strain exceeds 10%, the relative resistance change increases in a much accelerated and linear way, indicating that the inner yarn sensor start to be actually stretched and respond timely to the applied strain. The difference of sensing performance between the yarn sensor and fabric sensor is of great importance to understand and further optimize the properties of the fabric sensor.

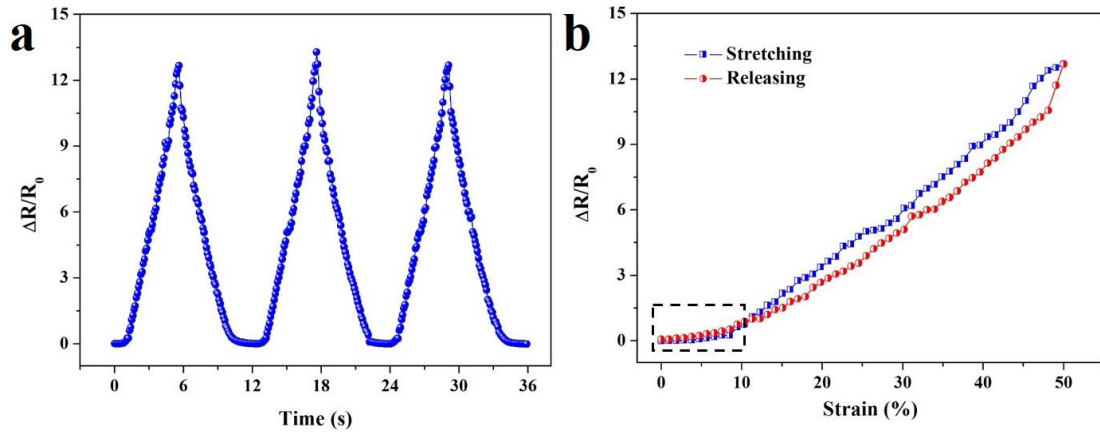


Fig 5.4 (a) Resistance change–time curve during stretching–releasing cycles. (b) Relative resistance change–strain curve of the fabric sensor.

From Fig 5.5a, it can be seen that the fabric sensor possesses a good capability to respond to the external strain, displaying a response and recovery time of 68 ms and 220 ms, respectively. The relatively short response time allows the quick response of the fabric sensor. As a good result, the fabric sensor possesses a constantly stable relative resistance change under varied stretching–releasing speeds at a strain of 50% as displayed in Fig 5.5b, indicating the superior sensing stability to different deformation speeds. As for the recovery time, although the resistance can almost recover to the initial value within only 220 ms, the complete recovery of resistance requires a longer time of ca. 400 ms. Besides the viscoelastic nature of PUY, another important reason should be the slow relaxation of the fabric structure after stress releasing.

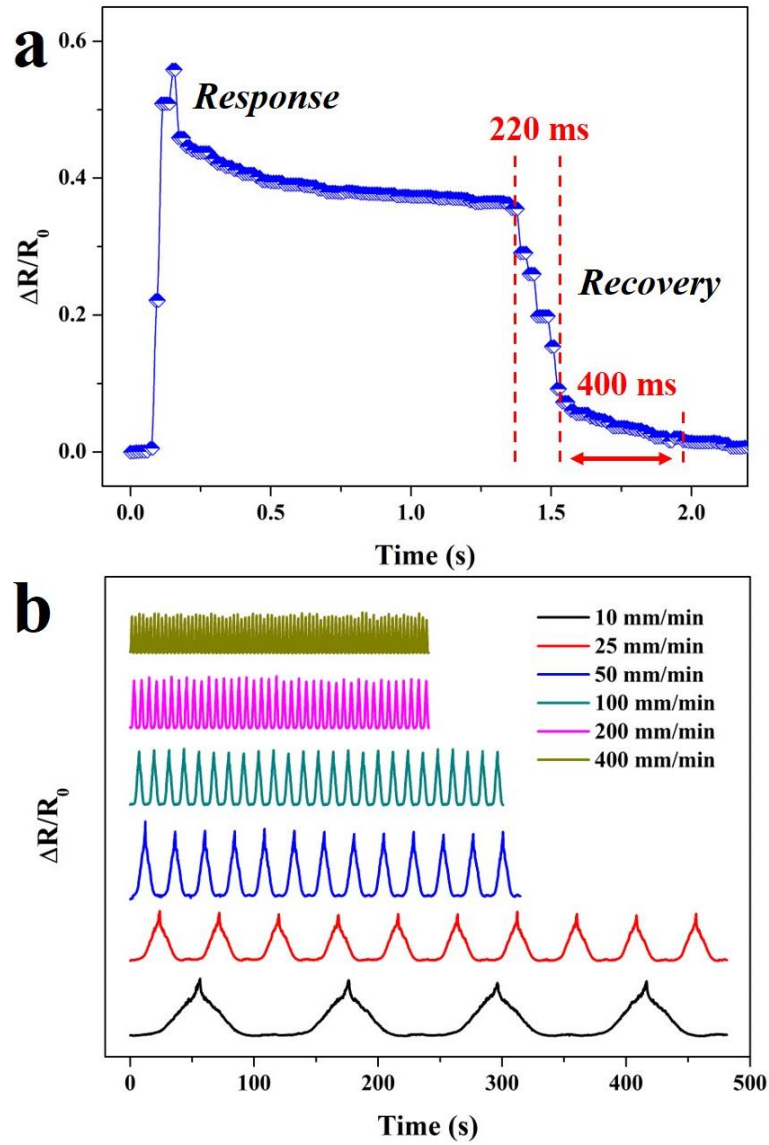


Fig 5.5 (a) The response and recovery curves the fabric sensors under a small strain of 5% and a testing speed of 600 mm/min. (b) The electromechanical properties of the fabric sensor under varied stretching–releasing speeds at a strain of 50%.

Fig 5.6 presents the durability test of the fabric sensor under continuous stretching and releasing cycles. The cyclic durability refers to the capability of the sensor to possess same sensing performance under continuous testing cycles, and the sensing response to recover to the original/unstretched value after releasing/unloading the strain. The high

durability is of vital importance for the practical application of the fabric sensor. Because in daily wearing the fabric sensor will be repeatedly deformed with varying amplitude and frequency when detecting the various human motions such as kicking, arm/finger bending and vocal-cord vibration. As shown in Fig 5.6, the fabric sensor exhibits very stable sensing performance even after 10000 stretching–releasing cycles. Furthermore, Fig 5.7 presents the result of the cyclic stability test of compressive bending of the fabric sensor, showing good performance under cyclic bending. The excellent durability and stability of the fabric sensor greatly promises the applications of wearable sensing.

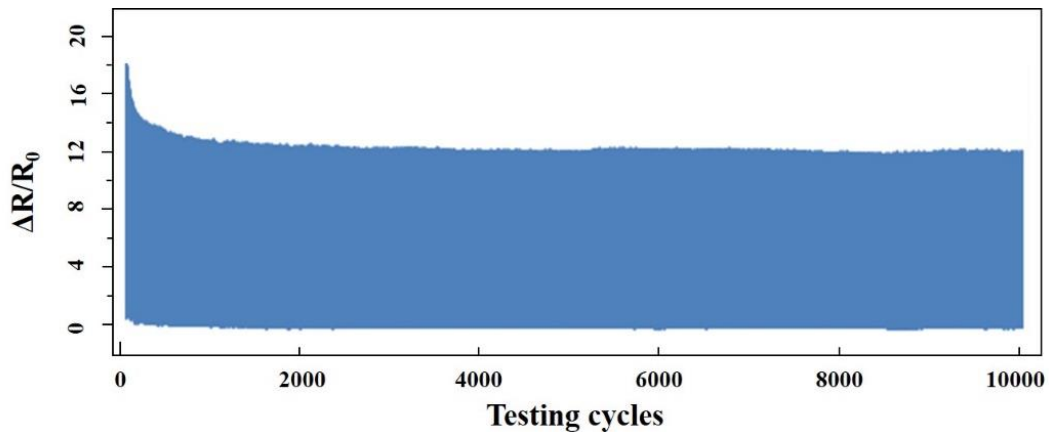


Fig 5.6 Durability test of the fabric sensor for tension.

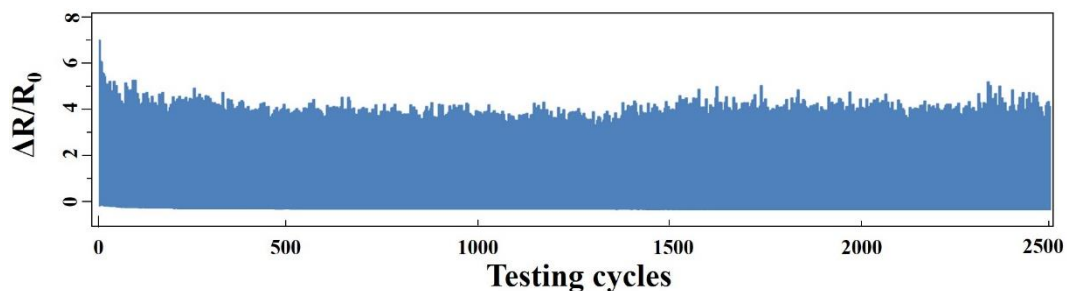


Fig 5.7 Cyclic stability test of compressive bending of the fabric sensor under the displacement of moving pressure head of 10 mm and the movement speed of pressure head of 100 mm/min.

Moreover, for the fabric sensor, the washability is another concern which need additional attention. A good washability requires the fabric sensor to be able to resisting the vigorous mechanical deformations and water invasion during washing, thus presenting unchanged and stable sensing performance after multicycles washing. To this end, the washability of the fabric sensor developed was evaluated with the results shown in Fig 5.8. It is clearly seen that after washing, the fabric sensor shows a slight decrease of GF (from 25.1 to 21.9) due to the slight shrinkage of the fabric substrate after washing but still maintains its good and stable sensing performance, indicating the good washability of the fabric sensor.

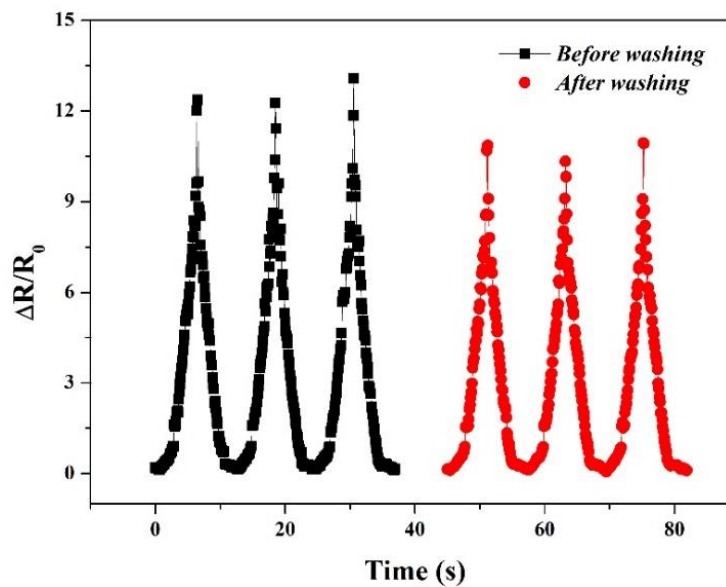


Fig 5.8 The sensing performance change of the fabric sensor before and after washing.

The sensing performances of some related state-of-the-art textile-based strain sensors are listed in Table 5.2. For these strain sensors, most of them exhibit some limits, such as low GF, poor durability, and nonlinear behavior, which cannot meet the requirements for long-term use in practical applications. In comparison, the fabric sensor based on the PDA/rGO/PUY yarn sensor attains a relative trade-off sensing performance, which displays desirable integration of good sensitivity, large stretchability, excellent durability, high linearity, and acceptable hysteresis. Additionally, compared with other fabrication methods, such as coating conductive materials on fabrics and knitting of conductive fiber/yarn, these combined fabrication protocols of simple dip-coating for 1D yarn sensor and industrial weaving technology for 2D fabric sensors offer great advantages in terms of scalable production, low consumption, negligible effect on the fabrics, and so on. The as-prepared fabric sensor/clothing fabricated by the yarn-sensor and weaving approach shows great potential for application as a real wearable system for long-term use.

CHAPTER 5

Table 5.2 Performance comparisons to related state of the art 2D textile-based strain sensors

Materials	Fabrication method	GF@strain	Durability (cycles@strain)	Linearity	Hysteresis	Effects on textile	Capability for long-term use	Ref
(PDA/rGO/PU)/elastic fabric	Weaving	25.3@50%	10000@50%	High	Low	Little	High	This work
CNT/Spandex	Knitting	0.25@100%	1000@100%	High	Low	Low	N/A	[170]
PPy/nylon lycra fabric	In situ polymerization	~ -3.3@20%	N/A	Nonlinear	Low	Low	N/A	[171]
		~ -0.7@60%						
PEDOT:PSS/PU	Wet-spinning knitting	~ -0.7@50%	500@100%	Nonlinear	N/A	High	N/A	[172]
		~ -0.3@200%						
Carbonized silk/Ecoflex	Carbonization	5.8@0-1%	6000@100%	Two linear ranges	Low	High	Low	[57]
		9.6@250%						
		37.5@250-500%						
Ag ink/PU	Printing	~13.3@30%	1000@30%	Nonlinear	High	Low	N/A	[173]

CHAPTER 5

Pen ink/cupra fabrics	Dip-coating	2.63@23%	5@2-4%	High	Low	Low	N/A	[165]
rGO/PE	Dip-coating reduction	-1.7@15% -26@8%	500@7.5/5%	High	Low	High	N/A	[101]
GWF/PDMS	CVD	500@2% 10000@8%	1000@2%	Nonlinear	N/A	High	Low	[111]
rGO/ (nylon & PU)	Dip-coating reduction	18.5@10% 12.1@10-18%	120@3%	Linear below 10%	Low	Low	N/A	[174]

5.3.3 Effect of fabric structure on the sensing performance

For the fabric strain sensor, it is worth noting that the yarn strain sensor plays the role of sensing element, and the sensing performance depends heavily on the fabric structure. Hence, in order to study the effect of fabric structure on the sensing performance of as-made fabric sensor, it is necessary to compare the sensing performance change of the strain sensor before and after weaving into the fabric. Table 5.3 lists the sensing parameters comparison between 1D yarn sensor and 2D fabric sensor. At first, the GF of the fabric strain sensor is only half of that of the yarn sensor integrated. The difference between the actual strain of the yarn sensor and the applied strain on the fabric should be responsible for this. Moreover, compared to the hysteresis error of the integrated yarn sensor (3.6%), the increased hysteresis behavior probably comes from the fabric structure factors such as the friction between yarns within the fabric during the fabric stretching and releasing. It is highly possible to further lower the hysteresis of the fabric sensor through optimizing the structural parameters in the future work. Moreover, the recovery time of the fabric sensor is 220 ms, which is much longer than that of the yarn sensor (168 ms), leading to increased interval time between two testing cycles of the fabric sensor of ca. 3s in Fig 5.4a. The possible reason is that there is a friction between sensing yarn and other yarns within the fabric when the sensing yarn was integrated into the fabric structure, which may result in a slower recovery of yarn sensor. Therefore, it can be concluded that the fabric structure has notable effects on the fabric sensor property, which will be further investigated and such parameters will be

optimized in the future work. Consequently, the fabric sensors with enhanced or even comparable sensing performance to yarn sensors are expected to be obtained.

Table 5.3 Sensing parameters comparison between 1D yarn sensor and 2D fabric sensor

Sensing parameters	1D yarn sensor	2D fabric sensor
Gauge factor @ 50% strain	50.0	25.3
Correlation coefficient	0.999	0.981
Hysteresis error (%)	5.0	14.4
Response time (ms)	60	68
Recovery time (ms)	168	220

For a better understanding of the electromechanical properties and its dependence on yarn sensor within the fabric and fabric structure, the actual yarn strain within the elastic fabric was investigated by examining yarn length using an optical microscope during the process of stretching the fabric in the weftwise as shown in Fig 5.9. At first, without strain, interlaced with the warp yarns, the weft yarn presents a curved shape within the fabric structure at the initial state. Under a small strain of 10%, the stretching of the yarn is too small to be observed. However, when applied with a strain of 20%, it can be observed that the curved weft yarn gradually reaches a straight state. Due to the less curved yarn segments of sateen structure, the curved weft yarn is transformed to an almost straight state with the strain increasing to 30%. With the further increased strain

to 50%, the straightened yarn is further extended.

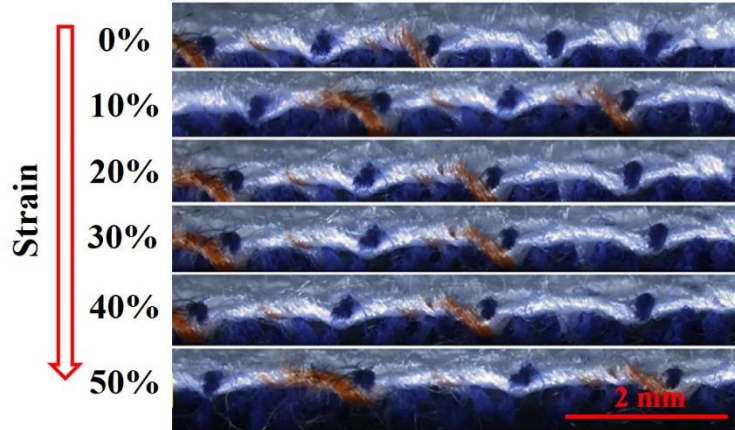


Fig 5.9 Optical image of fabric cross-section for examining the yarn configuration under increased strain from 0% to 50%.

At first, the original length (l_0) of inserted weft yarn within the fabric was measured based on the image of the initial fabric on the fabric cross-section. Then, the fabric images on the cross section were successively obtained at a step strain of 10% during the fabric stretching process from 0 to 50%. Based on these images, the length of weft yarn under increased strain was measured and recorded as l_s . The actual strain (ε) of the yarn is calculated by the following formula (1):

$$\varepsilon = l_s / l_0 \quad (1)$$

Fig 5.10a plots the relationship curve of actual yarn strain and applied strain on the fabric. It can be seen that the small strain of 10% applied on the fabric cannot induce

the stretching of the weft yarn, showing the actual yarn strain of nearly 0%, which is in accordance with the results of resistance change versus strain in Fig 5.4b. Thus, the region under small strain is called “crimp section”. When the applied strain increases to 20%, the yarn is stretched to a straight state, hence the actual yarn strain increases linearly with the applied strain, stepping into the “straightened section”.

Moreover, a finite element analysis (FEA) model was put forward to simulate the stretching of the yarn. For the FEA, it was assumed that the yarn is circular and homogeneous; the stretching of the yarn obeys Hooke’s law; there is no slide or friction between the warp and weft yarns. Fig 5.10b is about the applied boundary conditions, where the fabric was fixed on one side, and the displacement constraint is applied to another side with a tension speed of 100 mm/min, which is same with the tensile testing for the sensor. In addition, same linear periodic boundary conditions were applied for the warp yarns to simplify the simulation process. The simulated results were compared with the experimental results as plotted in Fig 5.10a. It is easy to see that the simulations results agree well with the experimental data, indicating that the FEM model is capable of predicting the mechanical behavior of the yarn within the fabric when applied with tension strain. The deformation behavior of the yarn within the sateen structure can be briefly summarized as follows: at the initial stage of small strain less than 10%, the deformation mainly occurred in the interchange region of warp and weft yarns. The curved segment of yarn is gradually stretched to a straight status, which can be called as a ‘crimp interchange’ phenomenon. At the same time, the linear segment of weft yarn

was also stretched, nevertheless the strain was much less than that of the curved segments. With the strain increasing to above 20%, the linear and curved parts of the weft yarn are stretched and straightened together, but it is believed that the deformation of the yarn primarily come from the linear parts, which are greatly extended to be almost linear condition. Therefore, the deformation behavior of the inserted yarn under the high strain can be defined as the ‘straighten’ phenomenon.

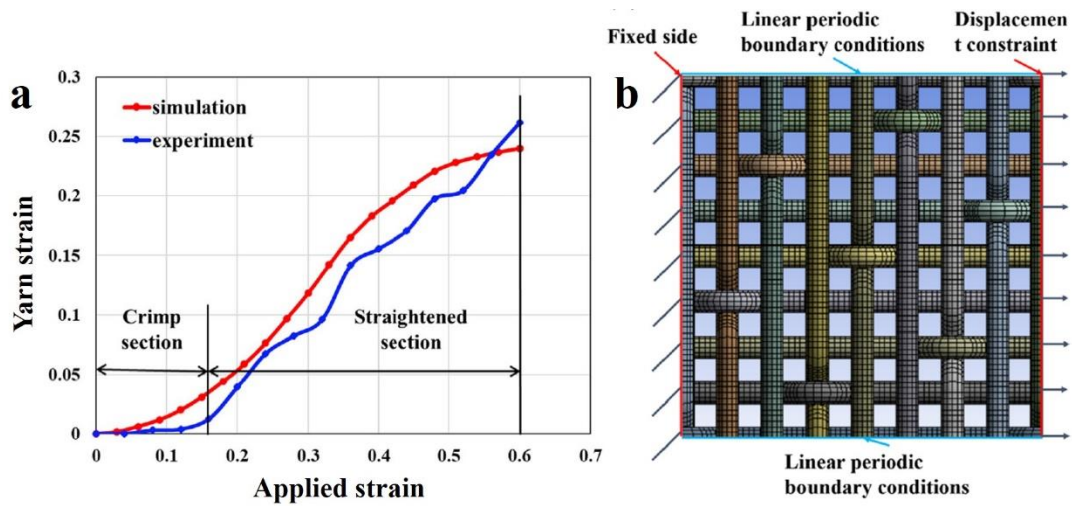


Fig 5.10 (a) Comparison between the applied strain on fabric and actual yarn strain. (b)

The applied boundary conditions for FEM.

Based on the above discussion, it becomes easy to understand the sensing behavior of the fabric sensor, which is mainly characterized by reduced sensitivity, increased recovery time and hysteresis error. When a small strain of 10% is applied on the fabric, the deformation of the yarn sensor is the transformation from curved to straightened, instead of being stretched. As a result, crack on the conductive rGO layer will not be

initiated, finally leading to the nearly zero resistance change. On the other hand, when the applied strain is bigger than 10%, the deformation of the yarn sensor steps into the “straightened section”, that is, the yarn will be stretched along with the increasing strain, and at this point, cracks on the rGO layer will quickly generate and grow to output obvious resistance change signal. Apart from the altered deformation behavior, the constraint and friction by the elastic fabric structure also prolong the recovery time of the yarn sensor. As for the increased hysteresis error, the hysteresis of the yarn sensor lies in the viscoelastic nature of the elastic polymer substrate, but in the case of fabric sensor, the relaxation of the fabric structure under stretching/releasing cycles will bring additional hysteresis, which should be in serious consideration for the design of fabric sensor by integrating yarn sensor.

5.3.4 Wearable fabric sensor prototypes for human motion detection

In order to examine the feasibility and performance of the as-fabricated yarn sensor and its fabric sensor for the practical wearable applications on the human body, a sensing bandage made of the fabric sensor was developed and wearing demonstrations were conducted to exhibit the capability of monitoring the various human motions. As shown in Fig 5.11, the yarn sensor was conformably attached on the cheek to monitor the chewing motion. It is clearly seen that the sensor can generate very obvious electrical signals due to the strain created during the chewing process, showing high sensitivity and strong ability of the yarn sensor for monitoring small motions. However, the precise

signal detecting requires the yarn sensor to be tightly adhered to the skin, which is usually completed by using adhesive tape. In fact, this contact way is not comfortable long-term wearing, which not only affect the wearing appearance but also bring discomfort to human skins.

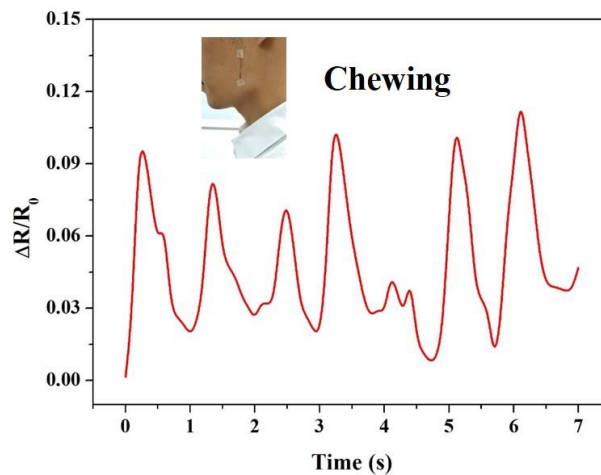


Fig 5.11 Wearing demonstrations of yarn sensor in monitoring the chewing.

For the stroke patients, the rehabilitation training is very important for the limb recovery. In this regard, the as-prepared fabric sensor-based bandage can be applied as a wearable monitoring electronic device for facilitating such rehabilitation training. For this purpose, by using the fabric sensors, three tubular fabric sensor bands, wrist-band, elbow-band and knee-band, were fabricated for detecting different limb motions. Fig 5.12a displays the strain sensing wrist-band worn on the hand wrist for monitoring the palm motion. By closely tracing the cyclic palm opening and closing actions by the sensing wrist-band, clear and stable signals generated by the wrist-band and palm

motion were captured and recorded, demonstrating a very good capability of wearable sensing textiles on monitoring subtle and dynamic motions. By using the prepared elbow-band, the monitoring of an elbow joint bending is shown in Fig 5.12b. It can be seen that the value of relative resistance change has an increase up to about 50% at the bending angle of 30 degrees and then increases to around 100% at the bending angle of 60 degrees. When the bending of the arm was further increased to 90 degrees, the increase of the relative resistance of the fabric sensor reaches 150%.

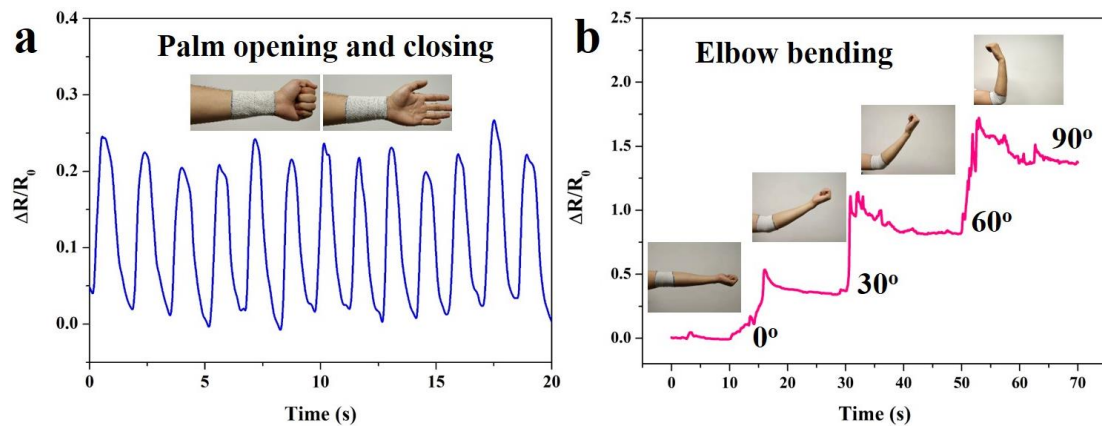


Fig 5.12 Wearing demonstrations of fabrics sensors in monitoring human motions. (a) Relative resistance change of sensing wrist-band made of fabric sensor during palm opening and closing. (b) Relative resistance change of different elbow bending degrees.

Based on such relationships between the angle and time of elbow bending and the relative resistance change, the fabric sensor can be used for monitoring the elbow motion precisely in terms of bending level and speed of the elbow joint. As shown in Fig 5.13a, benefiting from the capability of the sensor on multiple mechanical

deformation detection, the leg bending motion can be recognized by the sensing knee-band based on the transition of leg-bending-induced strain on the sensing band fabric to clear and stable signals. Furthermore, a detailed walking gait can be detected by using such a fabric-based sensing knee-band, as shown in Fig 5.13b.

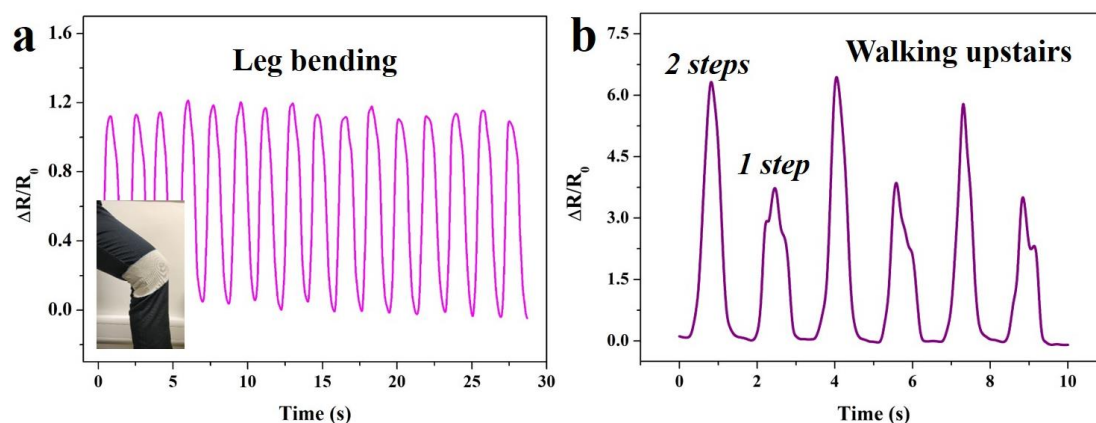


Fig 5.13 Wearing demonstrations of fabric sensors in monitoring human motions. (a) Relative resistance change of sensing knee-band in detecting leg bending and (b) gait during walking upstairs.

5.4 Conclusions

In this chapter, the 1D yarn sensor of PDA/rGO/PUY was successfully integrated into fabric structure like the common elastic yarn for fabricating strain-sensing textiles by using the mature textile technology easily. Thanks to the excellent flexibility of the PUY

and protection of the adhesive PDA layer, the strain sensor can be reserved with little damage. Furthermore, owing to its light weight and tiny size, the 1D strain sensor has negligible influence on the fabric's properties, such as the softness, breathability, and aesthetic feeling. The electro-mechanical performance of the prepared fabric strain sensor with sateen structure is tested and compared with the original 1D yarn strain sensor. The results demonstrate that the fabric sensor can rapidly respond to the applied strain, showing an excellent sensing performance in sensitivity, linearity and hysteresis behavior. Compared with the initial yarn strain sensor, the fabric sensor shows reduced sensitivity and increased hysteresis, which can be attributed to special deformation behavior of the yarn sensor within the fabric structure. As expected, the fabric sensor can be worn on human body directly like a common functional textile/clothing without discomfort or other negative effects, showing the great potential for applications as a real wearable system applied on long-term monitoring on human motion and conditions.

CHAPTER 6: Polydopamine Assisted Deposition of Silver Nanoparticles on Cotton Fabric for Highly Conductive E-Textiles as Wearable Strain Sensor and Heater

6.1 Introduction

Wearable electronics, which endow the traditional electronic devices with comfortable wearability, are attracting more and more attention because of their huge potential in various applications such as human motion detection [1,31,175], soft displays [176-177], electricity generation and storage devices [178-179], and so on. Especially, being a hierarchical fiber assembly worn on human body during the daily use, textile is considered as an ideal platform that can integrate diverse flexible electronic devices for developing textile-based wearable electronic systems, i.e. electronic textiles (e-textiles) [159,167,178]. Compared with the traditionally bulky and rigid electronics, the e-textiles present many unique advantages, such as high flexibility to accommodate the complicated body surfaces, excellent breathability and light weight for comfortable wearing, low cost for promising large-scale production, less pollution to the environment, etc. Therefore, the development of high-performance e-textiles, mainly by the ingenious convergence of textile and electronic technologies, is opening up a

new era of next-generation electronics. To achieve fully integrated electronics, the highly conductive e-textiles are believed to be indispensable, which can serve as flexible interconnects to seamlessly connect different functional parts. In general, the main strategy for preparing conductive e-textiles is to integrate various conductive materials to textile substrates. The common conductive materials are reported to include graphene [101,174,180], carbon nanotubes (CNTs) [181], conductive polymer [35,182], metal [173,183-184], the hybrids [31,34,185-186] and so on, and the main fabrication protocols involve dip coating [165,174,183,186], printing [173], vacuum filtration [187], spray coating [34], sputtering [31,185] and so forth.

Although many high-performance e-textiles have been reported until now, it is still challenging to solve the stability problem during practical applications. Since the conductive materials anchor the textile surface mainly by physical absorption, it is believed that the rigid conductive materials are prone to detach from the soft textiles because of their ductility mismatch under continuous and complex deformations during daily wearing [188], such as bending, twisting and friction, which may lead to the direct malfunction. On the other hand, for wearable applications, a good washability is also highly required, which further put forward higher stability demand for e-textiles to stand with the intense mechanical deformations and water invasion during washing [180,189]. Moreover, the shedding of some certain conductive materials may also cause adverse impact to human or environment [29,135]. To settle the aforementioned problem, encapsulation is always adopted to provide additional protection. For example,

polydimethylsiloxane (PDMS) was applied to encapsulate the graphene coated cotton fabric to function as a strain sensor, and as a result the strain sensor can display reliable and durable performance [100-101]. Wang et al prepared fabric-based strain sensors by carbonization of silk/cotton fabric, followed by the Ecoflex encapsulation, and strain sensors possess excellent sensing performance, in terms of high stretchability, fast response and especially notable durability of more than 10000 cycles [57,190-191]. However, the greatly improved durability by encapsulation sacrifices some unique advantages of textile, such as the breathability from its porous structure and low weight for comfortable and long-term wearing. Besides external encapsulation, another effective methodology is to enhance the bonding by introducing an interfacial polymer layer between conductive materials and textile substrate [192]. By tightly chemical bonding, a strong in-between adhesion can be generated to guarantee the stable conductivity. For instance, Liu et al modified the cotton yarns with polyelectrolyte brushes to tether copper particles, and the conductive yarns display outstanding mechanical and electrical stability under rubbing, bending, stretching and even washing [193]. Wu et al reported the conductive textile with high wash durability via covalently grafting polyaniline onto textile [182]. Despite the notable effect, this methodology generally requires complex chemical reactions and strict reaction conditions. Therefore, it is of significance to explore a simple and efficient strategy to prepare highly conductive and durable e-textiles.

Another issue hindering the practical applications of e-textiles is the environmental

stability. It is known that in daily life, the e-textiles will be exposed to different conditions such as humid, cold/hot temperature, and acid/alkaline environment, in which the properties of e-textiles including the conductivity and mechanical strength may be greatly deteriorated. Thus, an excellent anticorrosive feature is highly desirable. To this end, a waterproof or superhydrophobic surface offers a good solution. Via additional PDMS encapsulation, it was reported that the surface energy can be greatly reduced, thus forming a superhydrophobic surface [99,137]. Similarly, Yang et al. fabricated a waterproof supercapacitor fabric by encapsulation with hydrophobic polyester fabrics and further spraying with a polytetrafluorethylene agent [92]. Nonetheless, the method of encapsulation is not suitable for e-textiles because of the weakened breathability and comfort for long-term wearing.

In this chapter, we propose a facile and efficient method to prepare highly conductive, durable and waterproof e-textiles, by chemical deposition of silver nanoparticles (AgNPs) onto cotton fabric (CF), which was pre-modified with bioinspired polydopamine (PDA) as adhesive layer. The PDA layer, which tightly wraps the CF, was deposited by simple dipping in the dopamine solution under mild conditions. During subsequent deposition of AgNPs by reduction of Ag^+ ions, the Ag^+ ions were absorbed onto the surface of PDA modified CF, and meanwhile partially reduced to AgNPs by the catechol groups of PDA. After further reduction by glucose, a dense and continuous AgNPs layer was generated, yielding highly electrical conductivity. Importantly, the formation of interfacial PDA layer bridges the Ag/CF hierarchical

structure, providing robust electrical durability under cyclic mechanical bending, ultrasonication, and even machine washing. Additionally, after further modification with *1H,1H,2H,2H*-perfluorodecanethiol (PFDT), the e-textiles become highly waterproof, showing a water contact angle of ca. 152°. More importantly, due to fluorine containing surface, the waterproof e-textiles can work stably underwater as interconnects and exhibit outstanding self-clean ability. For wearable application, the as-prepared e-textiles demonstrate the good capability to be used as bending strain sensor and efficient wearable heater.

6.2 Experimental Section

6.2.1 Materials

The textile used is a commercially available cotton fabric (CF), with a thickness of 0.22 mm and weighing of 95.5 g/m². Chemicals of dopamine hydrochloride, silver nitrate (AgNO₃), hydrochloric acid (HCl), and sodium hydroxide (NaOH) were obtained from Sigma-Aldrich, Acros, Unichem and VWR, respectively. Ammonium hydroxide (NH₃·H₂O) and tris(hydroxymethyl) aminomethane (Tris) were bought from Alfa Aesar. *1H,1H,2H,2H*-perfluorodecanethiol (PFDT) and glucose were supplied by Aladdin. All chemicals were directly used without further purification.

6.2.2 Preparation

After successively cleaning in alcohol and deionized water by ultrasonication for 10 min, the fabric sample was firstly dipped into the dopamine solution (2 mg/mL) buffered by Tris-HCl (pH = 8.5) under magnetic stirring for 12h, followed by rinsing in deionized water to remove the residual PDA on surface. Secondly, the PDA coated fabric sample was dipped into the $\text{Ag}[\text{NH}_3]_2^+$ solution for the electroless plating of Ag, where glucose was used as the reducing agent. For the preparation of $\text{Ag}[\text{NH}_3]_2^+$ solution, a few drops of NaOH solution (5 wt.%) were added into the AgNO_3 solution, and then dilute $\text{NH}_3 \cdot \text{H}_2\text{O}$ solution (2 wt.%) was further added until the solution became transparent. The effect of $\text{Ag}[\text{NH}_3]_2^+$ content was studied by controlling the concentration of AgNO_3 solution, including 5, 10, 15, 20, 25 g/L, while the glucose kept twice of AgNO_3 to assure complete reaction. After Ag plating of 1h, the sample was thoroughly rinsed by deionized water to remove the residual chemicals and dried in oven at 60 °C. At last, to obtain a superhydrophobic surface, the as-prepared composite of Ag/PDA/CF was immersed in the PFDT solution (0.02 wt.%) for 30 min at room temperature. The final e-textiles of PFDT/Ag/PDA/CF composite were rinsed by deionized water and fully dried in oven at 60 °C before further testing.

6.2.3 Characterization

The sample morphologies were tracked by the scanning electron microscope (SEM) of

VEGA3, Tescan, Czech with an accelerating voltage of 20 KV, while energy dispersive X-ray spectroscopy (EDS) was utilized for elemental analysis. The molecular information on sample surface was studied by Fourier transform infrared spectroscopy (FTIR), PerkinElmer, USA, with a scanning number of 16 and resolution of 4 cm^{-1} . The thermal stability was studied by heating the sample from $50\text{ }^{\circ}\text{C}$ to $800\text{ }^{\circ}\text{C}$ with a heating rate of $20\text{ }^{\circ}\text{C}/\text{min}$ under N_2 atmosphere using thermogravimetric analysis (TGA), Mettler Toledo DSC/TGA1, Switzerland. The sheet resistance of the samples was tested by a 4-point probe resistivity meter (HPS2661, HELPASS, China). Water contact angle (CA) of different samples were investigated by using an optical CA measuring device (SDC-350, Sindin, China), where a water droplet of $5\text{ }\mu\text{L}$ was dropped onto the sample surface, and the CAs were calculated by averaging five measurement results on different surface positions. The tensile properties of the samples were conducted by Instron 5944 with the testing parameters of speed of $50\text{ mm}/\text{min}$ and gauge length of 30 mm .

For the electromechanical testing, the samples were cut with a testing area of $40\times 10\text{ mm}^2$ and connected by two Cu conductive tapes as testing electrodes. The stability of e-textiles was evaluated by an ultrasonic cleaner (950DAE, CREST ultrasonics, USA) and AATCC standard washing machine (3LWTW4815FW, Whirlpool, USA), respectively. The ultrasonication with a working frequency of 45 kHz was conducted for 10 min per cycle, and the washing test was conducted based on the AATCC Test Method 135. In details, the e-textiles were put into a laundry bag with the addition of

1.8 kg fabrics as ballasts and 66 g AATCC standard detergent, and the whole washing process of each cycle lasts about 40 min. After each testing cycle of ultrasonication or washing, the sample was dried by hanging in air, followed by the testing of volume resistance and surface sheet resistance. The current-voltage curve of the e-textiles was tested by a sourcemeter of Keithley 2400, USA. Moreover, the bending process was precisely controlled with testing speed of 200 mm/min by using an Instron universal test instrument, model 5944, USA, at the same time the volume resistance change was synchronously recorded by a multimeter of Keithley 2000, USA. For the electrothermal performance test, the temperature images of the sample ($40 \times 10 \text{ mm}^2$) were obtained by an infrared (IR) camera (E33, FLIR, USA).

6.3 Results and Discussion

6.3.1 Fabrication procedures

Fig 6.1a illustrates the fabrication procedures of the e-textiles, which mainly involves three steps. Firstly, as one of the textile materials used for a long history, the CF was simply dipped into the dopamine solution at room temperature for 12h, allowing the formation of adhesive PDA layer on surface. PDA is well-known as mussel inspired biomacromolecules, featuring the strong adhesion to nearly all materials' surface [153]. As shown in Fig 6.1b, by oxidation of oxygen in air, dopamine can be turned into

intermediates like quinone and 5,6-dihydroxyindole, and finally the PDA can be formed via noncovalent self-assembly and covalent coupling of these compounds [152,154]. Moreover, depending on the properties of different material surface, the adhesion mechanism can be coordination bonding, hydrogen bonding, π - π interactions, covalent reactions, van der Waals forces, and other electrostatic interactions [152,154,194]. In this case of cotton, the main adhesion force should come from the hydrogen bonding between PDA with the numerous cellulose fibers. Secondly, the PDA coated CF was immersed into the $\text{Ag}[\text{NH}_3]_2^+$ solution for the electroless deposition of conductive Ag layer. Due to existence of active catechol groups, the PDA layer can be used as reducing agent to reduce the $\text{Ag}[\text{NH}_3]_2^+$ ions, and meanwhile serving as capping agent to bind the generated AgNPs by the strong metal coordinations [195]. Moreover, glucose was introduced as additional reducing agent to accomplish the dense and continuous Ag layer. The chemical formation of AgNPs in solution is believed to initiate from the nucleating, followed by gradually growing and aggregating into large-size particles via electrostatic attraction, and finally in the way of Ostwald ripening, aggregates will be assembled into discrete and uniform particles [196]. Thirdly, to protect the Ag layer, the Ag/PDA/CF was further dipped into the PFDT solution to get a superhydrophobic surface. As displayed in Fig 6.1c, the e-textiles are characterized by a multilayered chemical structure, where the AgNPs are chemically anchored to the CF by metal coordination with PDA layer as an interface, and a thin layer of PFDT is applied to protect the AgNPs by the strong coordination between the Ag and sulfur [197].

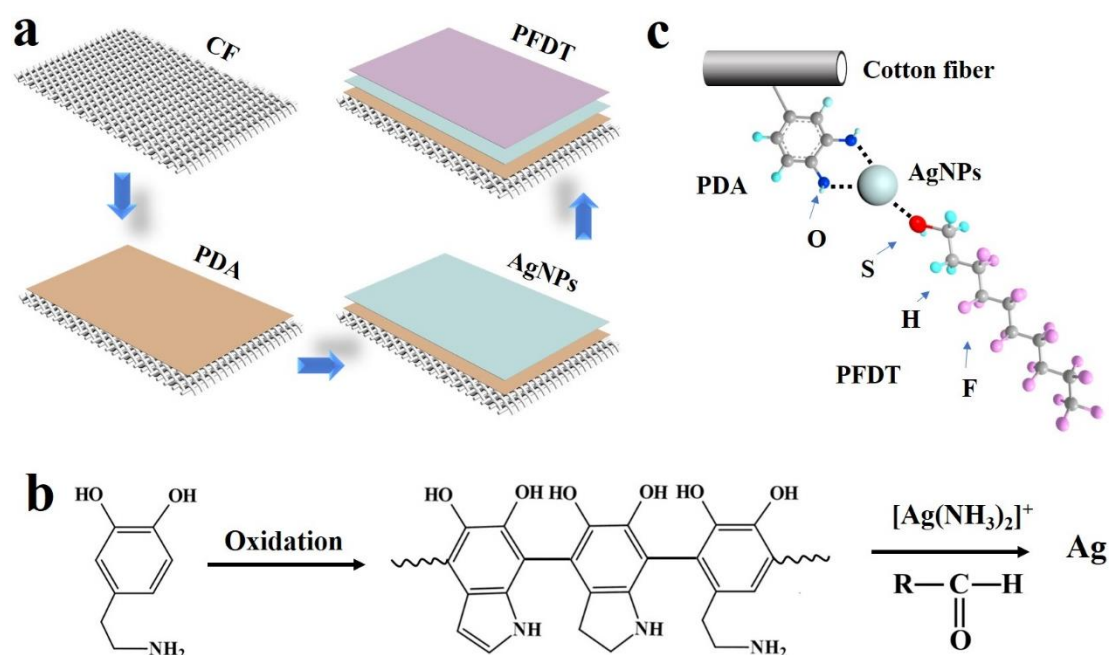


Fig 6.1 Scheme showing (a) the fabrication process and (b) chemical reactions of PFDT/Ag/PDA/CF e-textiles. (c) Scheme showing the molecular structure of PFDT/Ag/PDA/CF e-textiles.

As displayed in Fig 6.2, the sheet resistance of Ag/PDA/CF is dependent on the $AgNO_3$ concentration, and a plateau value of ca. 0.16 ohm/sq can be obtained at 25 g/L of $AgNO_3$ concentration. Based on this, the e-textiles prepared by 25 g/L were selected for the further testing. Despite the slightly increased sheet resistance from 0.16 to 0.26 ohm/sq arising from the insulating PFDT as shown in Fig 6.2, it is anticipated that the superhydrophobic surface will endow the e-textiles excellent anti-corrosion, thus guaranteeing the high stability under different harsh environments.

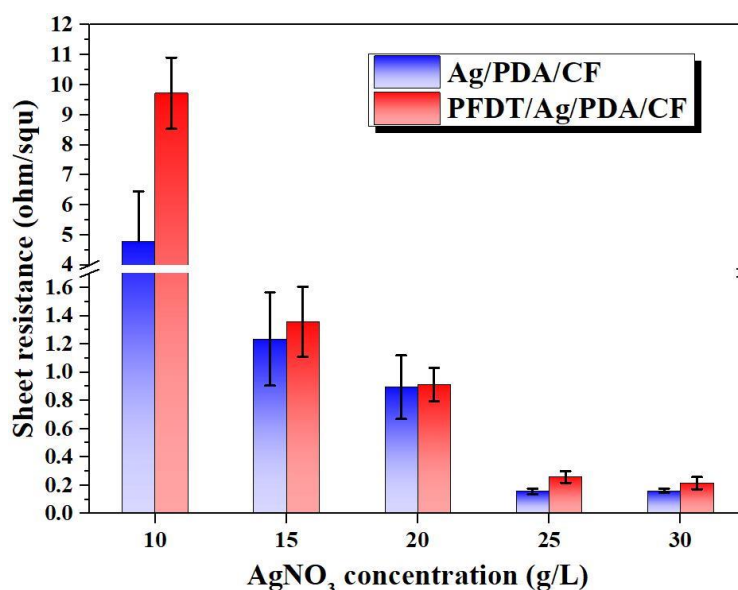


Fig 6.2 The relationship between the AgNO₃ concentration and the sheet resistance of Ag/PDA/CF and PFDT/Ag/PDA/CF.

Due to the much higher melting point, Ag can be reserved at high temperature, thus the actual Ag percentage can be obtained from the TGA results. In Fig 6.3a, the weight ratio of the CF, PDA/CF and Ag/PDA/CF after thermal degradation at 800 °C is 14.2%, 14.6% and 25.7%, respectively. Therefore, the weight percentage of AgNPs can be calculated to be approximately 13.0% [198]. Moreover, the tensile properties of the e-textiles were also examined as shown in Fig 6.3b, and it can be found that the e-textiles share a similar tensile behavior with the original fabric, with a tensile strength of 0.06 MPa, Young's modulus of 0.34 MPa, and elongation at break of 27%. The results suggest the little effect of PDA, AgNPs and PFDT coating on the tensile properties of fabric.

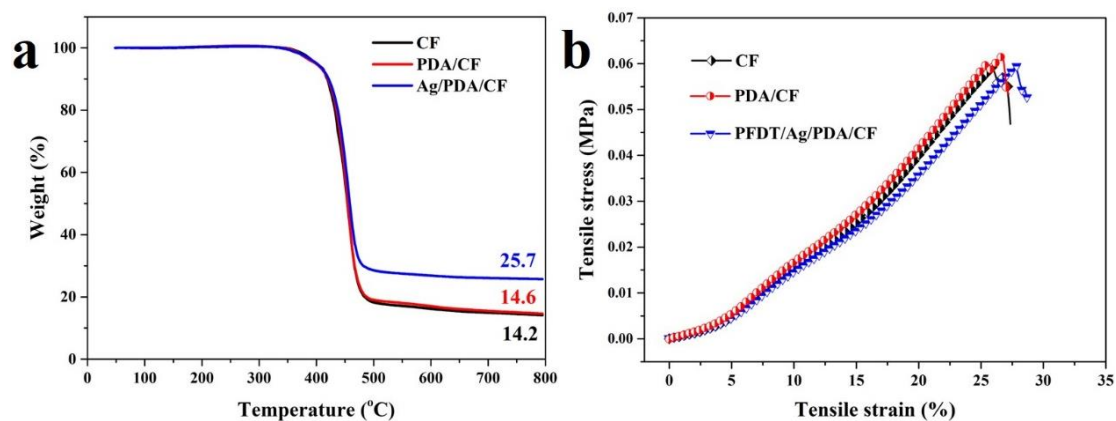


Fig 6.3 (a) TGA curves of CF, PDA/CF, and Ag/PDA/CF, respectively. (b) Tensile properties of CF, PDA/CF, and PFDT/Ag/PDA/CF.

The sample with a size of 40 mm × 10 mm in Fig 6.4a presents a low electrical resistance of 0.7779 Ω, indicating the formation of a continuous conductive network of the dense AgNPs on the fabric, and the volume conductivity (σ) was calculated to be 233.4 S/cm by the equation of $\sigma = L/SR$, where L , S and R refer to the length, area in cross-section, and volume resistance of the sample, respectively. The high conductivity of the e-textiles herein outperforms many other reported counterparts, such as e-textiles based on CNTs (125 S/cm) [199], graphene (77 S/cm) [200], PEDOT-PSS (2 S/cm) [201], polypyrrole (1 S/cm) [202], nickel (143 S/cm) [93], and copper (1 S/cm) [193]. Furthermore, of great significance is that the fabrication process is all solution based at room temperature without extreme conditions, making it facile to accomplish the large-area preparation of e-textiles as shown in Fig 6.4b.

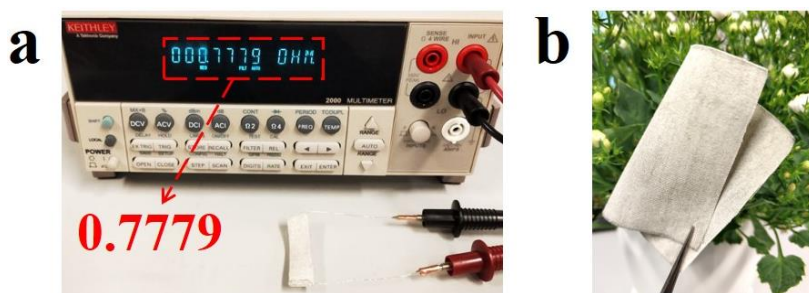


Fig 6.4 Photographs of (a) the electric resistance of a e-textile sample with dimension of 40 mm×10 mm, and (b) a large area sample.

6.3.2 Morphologies change of the e-textiles during preparation

SEM images provide a direct observation of the morphology. As shown in Fig 6.5a, the pristine CF with a plain weave structure, is composed by crosswise twisted cotton yarns, and the zoom in images show that each yarn contains dozens of cellulose fibers with a smooth surface (Fig 6.5b) and average diameter of 11 μm . After the surface modification by PDA, the color of CF changes from white to brown (Fig 6.6a), and SEM image in Fig 6.5c confirms the generation of PDA on CF surface, resulting in an uneven surface. Moreover, PDA macromolecules are characterized by the benzene rings, catechol and amido groups, and as revealed by FTIR (Fig 6.6b), two characteristic peaks of 1600 cm^{-1} and 3330 cm^{-1} can be clearly observed after the coating of PDA. The peak at 1600 cm^{-1} belongs to the C=C stretching vibration in the aromatic ring and N-H bending vibration, and the peak at 3330 cm^{-1} comes from the stretching vibration of phenolic O-H and N-H [156-157]. These results further prove the successful coating of N-containing PDA. XPS was conducted to prove the PDA interface. As shown in Fig

6.6c, compared with the pristine CF, the peak of N1s clearly proves the successful coating of PDA layer. Moreover, the molar ratio of N/C was calculated to be about 0.108, which approaches the theoretical value of PDA (0.125), further demonstrating the PDA surface. In addition, it can be observed that there is a small shift of the absorption peak at 3330 cm^{-1} for PDA/CF, compared with that of pure PDA (3291 cm^{-1}). Such variation is believed to suggest the strong interaction by hydrogen bonding between the CF and PDA [203]. The catechol and amine groups of PDA layer can help absorb the $\text{Ag}[\text{NH}_3]_2^+$ ions, and the partially reduced AgNPs by PDA can be used as catalytic sites for further growth of AgNPs.

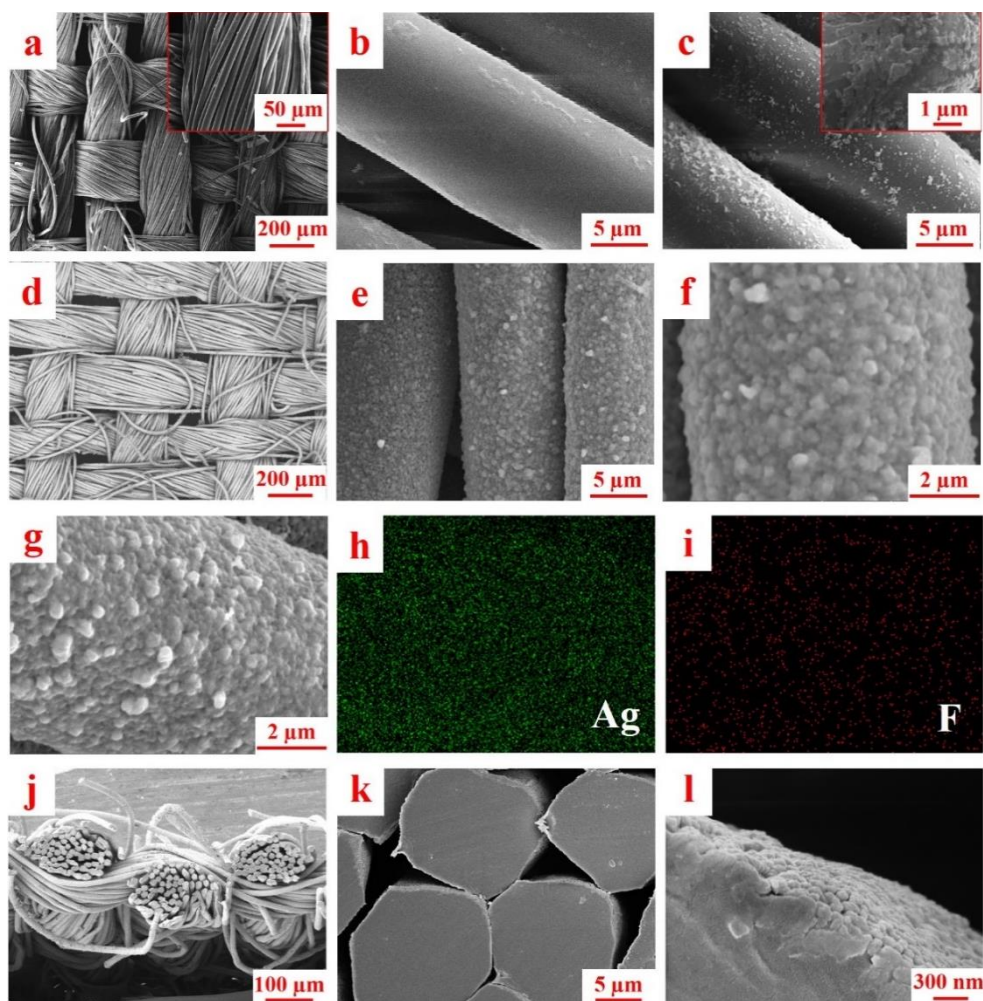


Fig 6.5 SEM images of (a, b) pristine CF with different magnifications, (c) PDA/CF, (d-f) Ag/PDA/CF with different magnifications, (g) PFDT/Ag/PDA/CF e-textiles and the relevant elemental mapping of (h) Ag and (i) F, (j-l) Cross-sectional SEM images of the e-textiles with different magnifications.

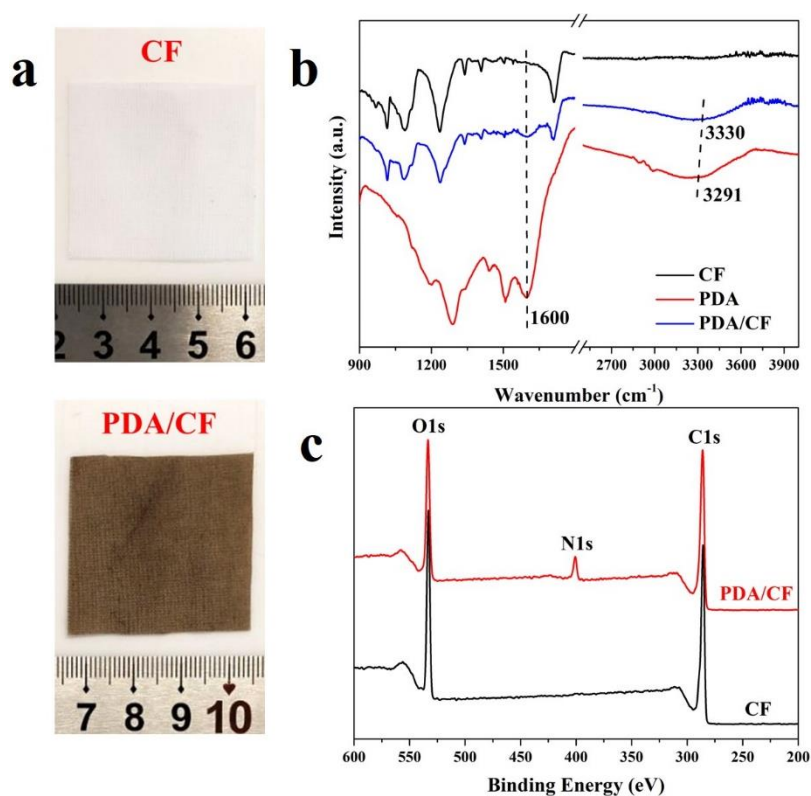


Fig 6.6 (a) Photographs of the pristine CF and PDA/CF. (b) FTIR curves of CF, PDA, and PDA/CF, respectively. (c) XPS curves of the CF and PDA/CF samples.

By adding glucose, the residual $\text{Ag}[\text{NH}_3]_2^+$ ions are completely reduced, thus producing a dense layer of AgNPs. From Fig 6.5d&e, it can be observed that numerous AgNPs, with an average diameter of ca. 250 nm, uniformly and tightly wrap around the cotton fiber. It is considered that the electrical conductivity is closely associated with the

conductive paths, and more conductive paths generate higher conductivity or lower resistance. In this study, the AgNPs-covered conductive cotton fibers constitute the conductive networks of the e-textiles, and the twisted structure favors the compact connection between each single conductive fiber. This unique three-dimensional (3D) conductive network notably increases the number of electrically conductive paths, thus guaranteeing the high and stable conductivity. The high conductivity by the dense coating of AgNPs should be attributed to the PDA modification. In comparison, the sample without PDA was prepared under same condition as shown in Fig 6.5f, and it can be clearly observed that only discrete AgNPs exist on the CF surface, meaning that without PDA, the AgNPs will prefer growing in the solution instead of on the CF surface, finally leading to a nonconductive surface. Moreover, Fig 6.5g shows the SEM image after coating with the PFDT layer. Because of the low concentration and thin thickness, there is no obvious change about the surface morphology. The EDS mapping image of the Ag (Fig 6.5h) and F (Fig 6.5i) element proves a uniform distribution of the PFDT and AgNPs on the surface of cotton fiber, indicating the successful modification of PFDT. The cross-sectional SEM images of the e-textiles are also displayed in Fig 6.5j-l. It is evident that the circular cotton fibers are wrapped with a continuous AgNPs layer, suggesting the all-around deposition of AgNPs on the surface and inside of the cotton fabric via this solution-based method. Furthermore, as shown in the zoom-in image of Fig 6.5l, the AgNPs layer with a thickness of ca. 310 nm is observed to closely adhere to the cotton fiber surface, showing an enhanced interface, which should be attributed to the assistance of the PDA interlayer.

6.3.3 Electrical response of the e-textiles to mechanical bending

Fig 6.7a displays the resistance change of the e-textiles under mechanical bending. The sample was bent from original 40 mm to 35 mm, 30 mm and 20 mm, with the increased bending length of 5 mm, 10 mm, 20 mm respectively. It can be seen that the e-textile can respond regularly to different bending length, and the bigger bending length can generate the higher resistance change. Furthermore, the degree of resistance change or sensitivity to bending can also be expressed by gauge factor (GF) as follows: [168,204]

$$GF = (\Delta R/R_0)/\Delta\varepsilon \quad (1)$$

$$\varepsilon = \pm t/2r \quad (2)$$

$$d = 2r*\sin(l/2r) \quad (3)$$

where ε represents the applied strain, t of the sample thickness, r of the bending radius, d of the distance between two ends under bending, and l of the arc length of sample, respectively. As a result, the GF is calculated to be about 7.1. The resistance change under bending is related with the fabric structure change. The conductive paths composed by the numerous conductive fibers will adjust themselves to follow the mechanical bending, thus resulting in the contact resistance change. The resistance increase should come from the relaxation of contacts between Ag coated cotton fibers during the bending. Under a stress-free condition, the AgNPs coated cotton fibers connect well with each other to form a continuous conductive network. When applied

with a stress by bending, some conductive fibers will be deformed or distorted, and gap between the fibers will appear and gradually expand with increased strain in the conductive network, leading to the decreased conductive paths and thus increased resistance. When the stress is released, the flexible conductive fibers can basically restore to the initial position, followed by recovered resistance. In addition, Fig 6.7b demonstrates the stable resistance change under the continuous bending of 500 cycles.

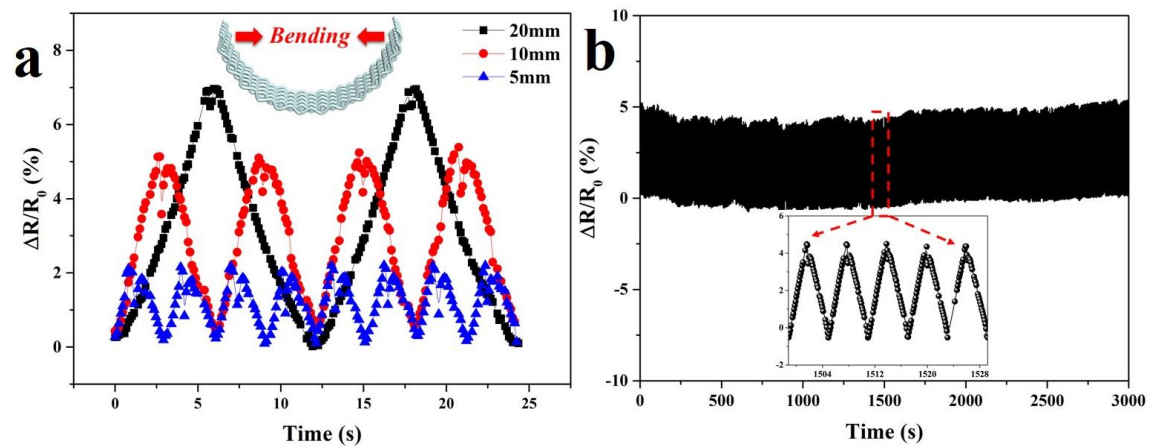


Fig 6.7 (a) Relative resistance change of the e-textiles under different bending length and (b) bending length of 10 mm for 500 cycles.

To deeply understand the electrical resistance change, a simple resistance model of the e-textiles is illustrated in Fig 6.8a. In the elementary unit, the total resistance is decided by two parts [11, 28]: the intrinsic resistance of the conductive yarns (R_l) and the contact resistance between the warp and weft conductive yarns (R_{cl}). Since the e-textiles here have same structure along the warp and weft direction, the R_l value is considered to be identical on the two directions. Furthermore, each conductive yarn is made up of numerous twisted conductive fibers, thus R_l is in fact related with the

resistance of single conductive fiber (R_2) and the contact resistance between neighboring fibers (R_{c2}). Based on this, R_2 , R_{c1} and R_{c2} are considered as the basic parameters. R_{c2} value can be controlled by the agent concentration during the electroless plating process, and the aforementioned results in Fig 6.2 testifies the resistance can be notably decreased with the AgNO_3 concentration increasing to 25 g/L. Moreover, compared with methods like metal sputtering or thermal evaporation, the solution can easily diffuse into the inner structure of the fabric, and a uniform coating can be obtained for all fibers, which benefits the formation of a perfect 3D conductive network as well as low contact resistance. As for the contact resistance, fabric structure is believed to play an important role. According to Holm's theory, the contact resistance (R_c) can be defined as follows:

$$R_c = \frac{\rho}{2} \sqrt{\frac{\pi H}{nP}} \quad (4)$$

where ρ , H , n , P represents the electrical resistivity of the conductive fiber, the material hardness, the contact points number and contact pressure between different conductive fibers, respectively. Since the values of ρ and H keep unchanged whether there is a strain, the resistance change should come from the change of n and P . Therefore, the twisting structure is in favor of higher n and P , thus a low R_{c2} , while R_{c1} can be regulated by the yarn density along the warp and weft directions. Based on the above discussion, one can know that the resistance change under mechanical bending should mainly come from the contact resistance change (R_{c1} & R_{c2}) of the fabric structure, while the PDA

enhanced interface and superhydrophobic surface assures the stable surface resistance (R_1 & R_2) under external interference such as ultrasonication and machine washing. Moreover, it is worth noting that, compared with the mostly reported film-based flexible electrodes, the 3D conductive structure of e-textiles assembled by numerous fibers not only owns superior breathability, but also particular advantage of preventing crack propagation and catastrophic failure. The relatively resistance change under mechanical bending is also beneficial for wearable electronics as conductive interconnects. As a proof in Fig 6.8, three light emitting diodes (LEDs) were fixed on the e-textiles by silver paste. Owing to the low resistance of e-textiles, the LEDs can be lit with a low voltage of 2.5 V. More importantly, the brightness of LEDs keeps unchanged under bending compared with that of flat, proving the stable electrical resistance.

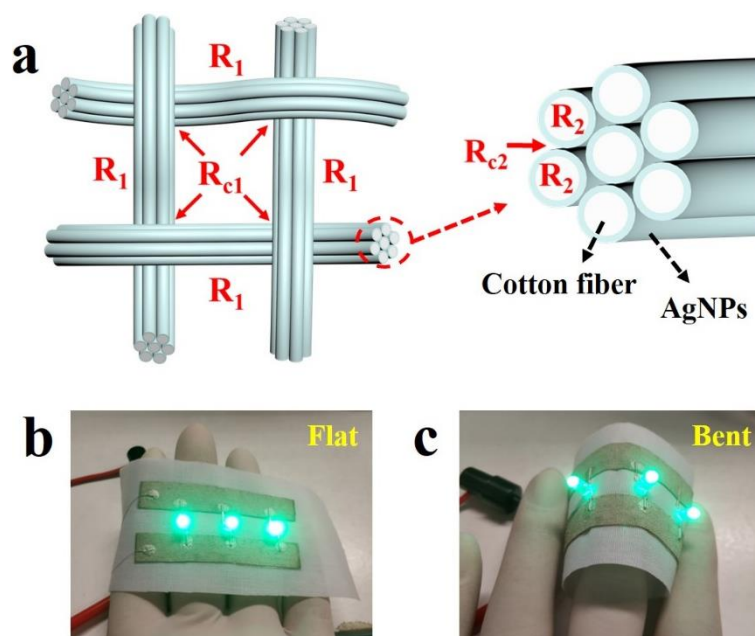


Fig 6.8 (a) Schemes illustrating the electrical resistance model. Photographs showing

the LEDs connected by e-textiles under (b) flat and (c) bent states.

6.3.4 Superhydrophobic and anti-corrosive properties

Fig 6.9a presents the water CAs of CF with different surface modification. The pristine CF is superhydrophilic because of the abundant hydroxyl groups, showing a CA of 0°. After coating with PDA layer, the CA keeps the same value of 0°, indicating the superhydrophilic property of PDA. In clear contrast, the coating of dense AgNPs layer notably increases the CA to 118°, which should be attributed to the enhanced surface roughness. As revealed by SEM, the numerous AgNPs connect with each other, transforming the surface from smooth (Fig 6.5b) to rough and uneven (Fig 6.5f). According to the Cassie-Baxter wetting theory [138,205], the CA θ^* of a water droplet on solid surface can be expressed by equation (5)

$$\cos\theta^* = f_1\cos\theta - f_2 \quad (5)$$

where θ represents the CA of water on the flat solid surface, and f_1 and f_2 are the area fractions of solid surface and air in contact with water, respectively. The CA between water and air is 180°, and $f_1 + f_2 = 1$, thus a larger f_2 will result in a higher θ^* . Herein, the AgNPs tightly interconnect and form a rough surface, and the large amount of air trapped between the interspace of adjacent AgNPs finally contributes to the large CA of 118°. After further treatment with PFDT, the surface of conductive AgNPs layer was uniformly covered by the fluorine-containing molecules, which can be demonstrated

by the elemental mapping of fluorine in Fig 6.5i. The combination of the high surface roughness from the AgNPs and low surface energy from the fluorine-containing PFDT endows the e-textiles a superhydrophobic surface, and the CA value is significantly increased to 152° . As displayed in the inset of Fig 6.5a, when the water droplet is forced to touch the e-textiles surface, it tends to adhere to the syringe needle instead of the e-textiles surface, and no water is observed to leave on the surface after the removal of the syringe needle, clearly indicating the very weak adhesion between water and the e-textiles surface. The notable water repellence allows the e-textiles to be used in high humidity, and even underwater for a prolonged service life. For example, Fig 6.9b shows the resistance change of the e-textiles underwater. From the upper inset, when the e-textiles are immersed in water, strong light reflection can be clearly observed on the surface of e-textiles, which should be ascribed to the light reflection from the trapped air bubbles on the surface, thus it is believed that the superhydrophobic surface is capable of protecting the e-textiles from being wetted from external environment. During the immersing in water of 50 h, the resistance keeps almost same with the original value of R_0 . As a visual proof, the e-textiles were used as interconnects underwater, and the LED can be easily turned on with vivid brightness.

On the other hand, as shown in Fig 6.9c, the e-textiles can retain the superhydrophobicity towards acid and alkaline solutions, presenting same CAs around 152° with that of water, making it promising in the applications of different harsh environment. In addition, an excellent anti-corrosion or self-cleaning ability is also of

great importance for the e-textiles in practical applications. Fig 6.9d shows the status of the e-textiles stained by common liquid foods including tea, milk and coffee, where all the liquid droplets keep free-standing sphere-shape, which can roll off easily without leaving any staining trace. In clear contrast, for the pristine CF, the liquids can quickly diffuse into the fabric, leading to severe staining (Fig 6.9e). This outstanding self-cleaning ability from the superhydrophobic surface can assure the conductive e-textiles a clean and safe condition for wearable electronics.

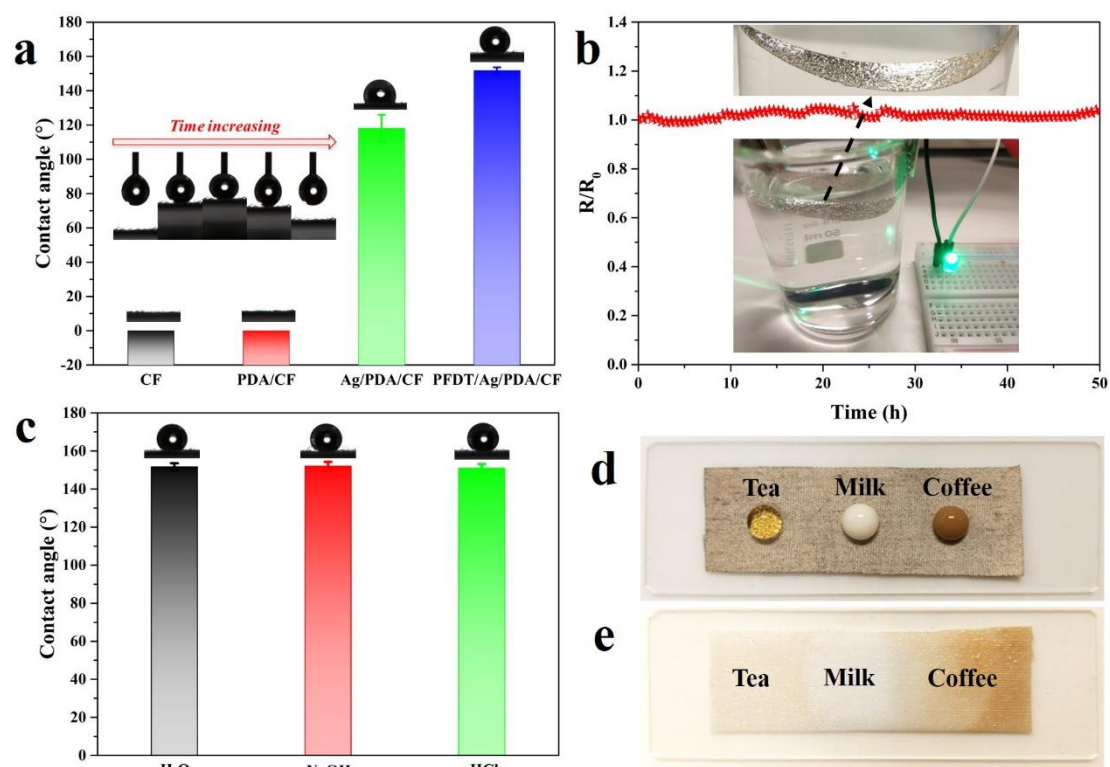


Fig 6.9 (a) Water CAs of CF, PDA/CF, Ag/PDA/CF and PFDT/Ag/PDA/CF, and the insets showing the non-adhesive surface of PFDT/Ag/PDA/CF e-textiles. (b) Resistance stability of PFDT/Ag/PDA/CF e-textiles immersed in water, and insets of application as interconnects underwater. (c) CAs for water, HCl solution (0.1 mol/L)

and NaOH solution (0.1 mol/L) on the surface of PFDT/Ag/PDA/CF e-textiles. Photographs showing the state of different liquid droplets on the surface of (d) PFDT/Ag/PDA/CF e-textiles and (e) CF.

6.3.5 Electromechanical stability

For the practical applications, besides the different environments, the e-textiles will always undergo various deformations with varying amplitude and frequency. To keep a stable conductivity, it is required that the interface bonding between the conductive layer and flexible substrate is strong enough. To this end, strong ultrasonication is applied to evaluate the stability of the e-textiles. As shown in Fig 6.10a, during the multicycles ultrasonication, the e-textiles display stable electrical resistance, with relative resistance change slightly increasing of less than 5%. Sheet resistance can be used to reflect the surface resistance. In Fig 6.10b, under ultrasonication the sheet resistance of e-textiles remains stable, and the SEM image in Fig 6.10a further proves that the conductive layer formed by dense AgNPs can still wrap tightly around the fiber, suggesting the robust adhesion between AgNPs and fabric substrate. Besides the stable electrical performance, the highly waterproof surface can also be well reserved after intensive ultrasonication, presenting a CA of 151° as shown in the inset of Fig 6.10a.

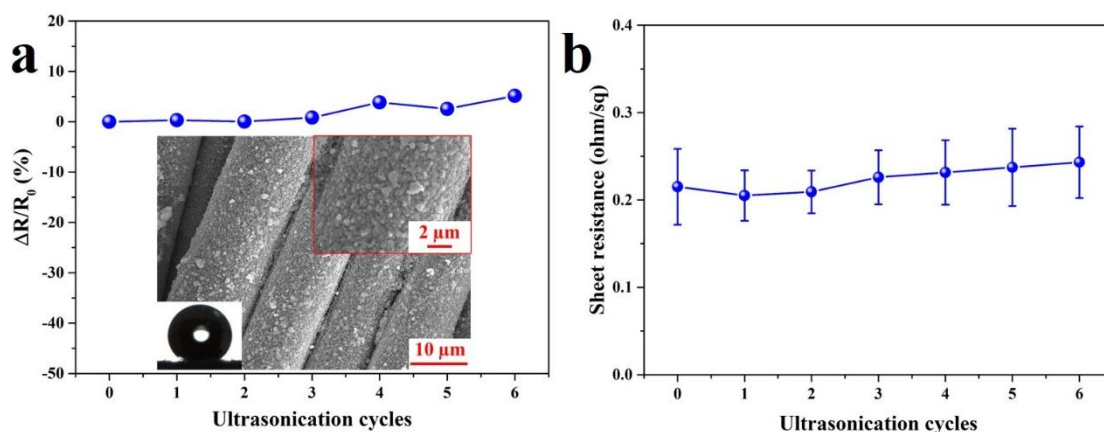


Fig 6.10 (a) The relative resistance change of the e-textiles after different cycles of ultrasonication, where the insets show the water CA and SEM surface morphologies after 6 cycles' ultrasonication. (b) The sheet resistance changes of e-textile after different cycles of ultrasonication.

Washability is another important but still challenging issue to be solved for textile-based electronics. During the common machine washing, apart from the vigorous mechanical actions like twisting and rotating, severe water invasion is another big concern, which may lead to the immediate failure of e-textiles. Herein, the washing durability of e-textiles was evaluated by standard laundering with repeated cycles as described in the experimental section. As illustrated in Fig 6.11a, after the first two washing cycles, the relative resistance change of the e-textiles increases to 10%, and a small plateau value of ca. 13% is reached after 6 standard washing cycles. On the other hand, the sheet resistance slightly increases from 0.25 ohm/sq to 0.41 ohm/sq (Fig 6.11b), and the inset in Fig 6.11c reveals the basically intact conductive layer and reserved high CA after washing. The reason for such resistance increase is mainly due to the mechanical

untwisting of some conductive fibers as shown in Fig 6.11a, as well as a small part of the AgNPs loss on the surface, which should be caused by the mechanical deformations from the spinning action as well as abrasion exerted by the ballast fabrics during washing. Compared with other reported results [174,180,187,189], the resistance change of this e-textiles under washing is relatively small, which should be ascribed to the well-designed structure, i.e. the enhanced interface by PDA and superhydrophobic surface by PFDT, together endowing the e-textiles prominent stability against externally mechanical and water interference during washing.

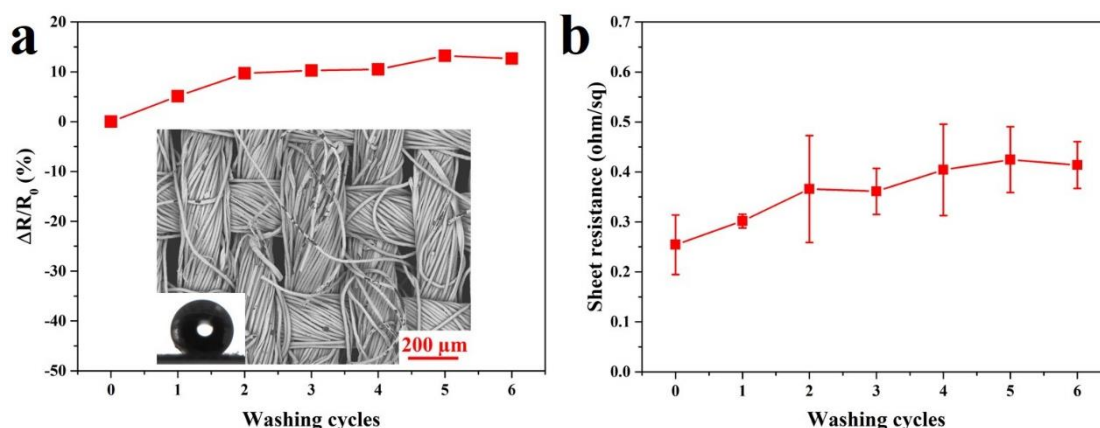


Fig 6.11 (a) The relative resistance change of the e-textiles after different cycles of machine washing, where the insets show the water CA and SEM surface morphologies after 6 cycles' machine washing. (b) The sheet resistance changes of e-textile after different cycles of machine washing.

The rub/abrasion resistance of the e-textile was conducted using the Martindale method. In details, as shown in Fig 6.12a, the sample was firstly cut into the circular shape with

diameter of 38 mm to fit with the sample holder; secondly a pressure weight was used to apply a pressure of 9 KPa to the sample; thirdly, the e-textile sample will be abraded on the standard fabric abrasant and the sheet resistance will be measured every 100 abrasion cycles.

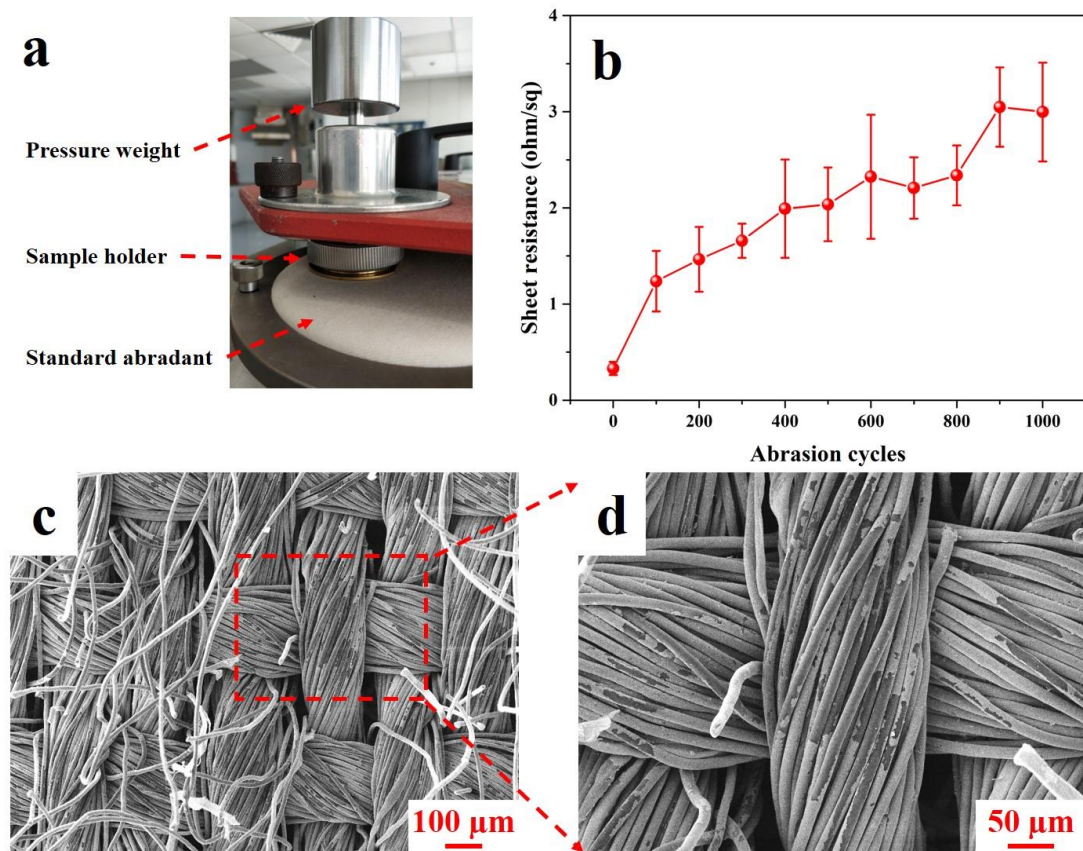


Fig 6.12. (a) Photograph showing the abrasion testing setup (b) the sheet resistance change of the e-textile with increasing abrasion cycles; (c-d) SEM images of the e-textile sample after abrasion testing of 1000 cycles.

Fig 6.12b displays the sheet resistance change with increasing abrasion cycles. It can be seen that the sheet resistance of the e-textile increases to 1.24 ohm/sq after the first

100 cycles, and then slowly increases to 3.05 ohm/sq during the further abrasion cycles of 1000 cycles. As revealed by the SEM images, the resistance change during abrasion mainly comes from the untwisting and breaking of some cotton fibers (Fig 6.12c) as well as partial shedding of the AgNPs on the abrasion surface (Fig 6.12d). By virtue of the 3D conductive network composed by numerous conductive fibers, the e-textile still exhibits low electrical resistance, thus it is considered that the part loss of AgNPs on the surface shows little effect on the conductive paths. However, the mechanical properties of the fabric need further improvement to prevent the fibers' rupture under external interference.

6.3.6 Joule heating effect for wearable heater

Owing to the high conductivity, the e-textiles are also promising to be applied as wearable heater by Joule heating effect. Fig 6.13a presents the temperature development curves of the e-textiles under different voltages ranging from 1 to 5 V. When applied with a voltage, the surface temperature increases rapidly, and subsequently reaching a saturated temperature (T_s) within only 10 s. Moreover, the T_s value is proportional to the applied voltage (U), and the relationship between T_s and U can be defined with equation (6) [206-207]:

$$T_s = T_0 + \frac{U^2}{hRA} (1 - e^{-t/\tau}) \quad (6)$$

where T_0 is the environmental temperature, h is heat transfer coefficient, t is the heating time, τ is the time constant, R and A is the resistance and surface area of the e-textiles respectively. From equation (6), one can know the T_s is a balanced result between the Joule heating and thermal dissipating to the environment, and the low resistance of the e-textiles avails for higher T_s . Moreover, the current-voltage curve in Fig 6.13b presents a linear characteristic, indicating that the e-textiles obey Ohm's law and possess stable resistance under different voltages. As shown in Fig 6.13c, a quite good linear relationship with a coefficient of determination (R^2) of 0.99538 can be observed between the T_s and U^2 , confirming the validity of equation (6). More importantly, the e-textiles can be heated up to 53 °C under a low voltage supply of 3 V, indicating its high conductivity and electrothermal performance. As shown in Fig 6.13d, the stability and reliability of the thermal heating performance is investigated by conducting five heating-cooling cycles under 3 V. The surface temperature increases when the power is on, and cools down gradually to the room temperature once the power is off. Especially, the temperature change curves are almost identical during the five cycles, suggesting the stable and repeatable thermal heating performance.

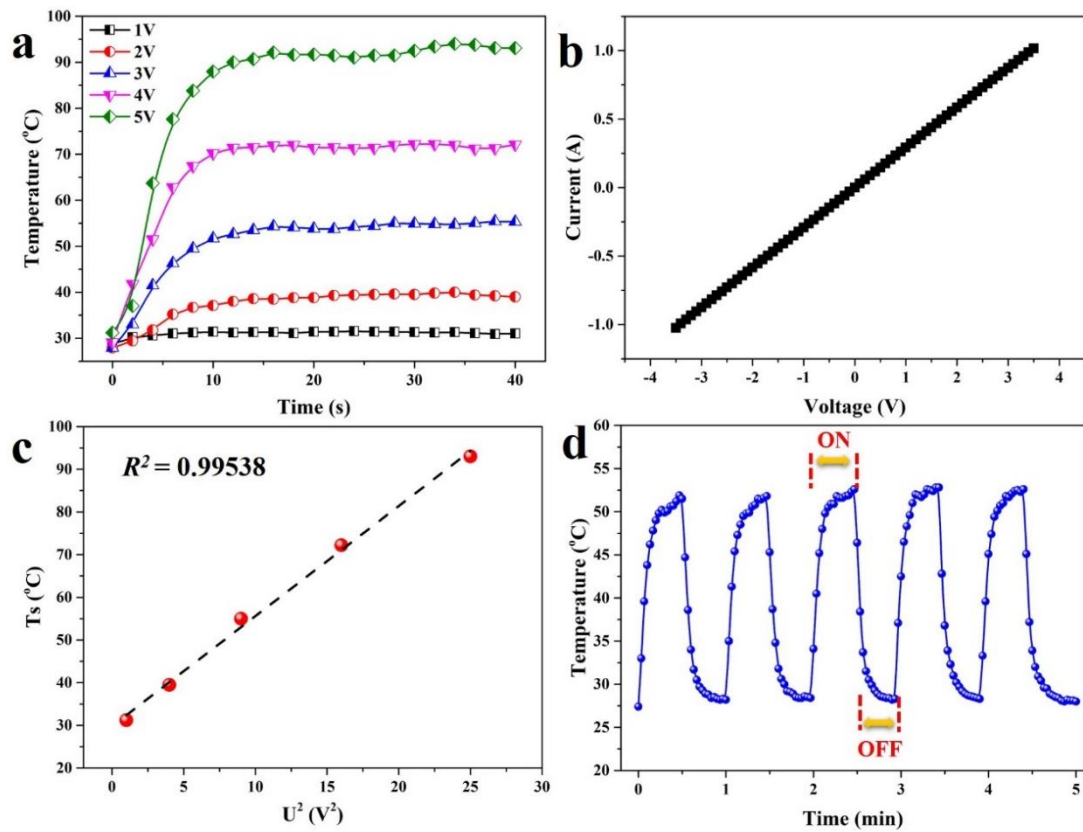


Fig 6.13 (a) Time-dependent temperature development of the e-textiles under different voltages. (b) Current-Voltage curve of the e-textile. (c) Experimental results of T_s versus U^2 and the linear fitting. (d) Temperature development of the e-textiles under cyclic heating and cooling test applied with a voltage of 3V.

Combined with the merit of superhydrophobic surface, the outstanding thermal heating performance is able to grant the e-textiles with good deicing performance. As displayed in Fig 6.14a, applied with a voltage of 3V, the temperature of e-textiles is quickly increased, and the melting of ice cube on the surface is sped up, leading to the transformation of the ice cube to water within 150 s. Moreover, the superhydrophobic surface can hinder the invasion of generated water. In contrast, without voltage, a much

longer time of 390 s is required to fully melt the ice cube at the room temperature of 25 °C (Fig 6.14b). The notable thermal heating performance could help protect the e-textiles from icing, thus extending the applications, especially in the low temperature fields. Since the e-textiles are highly flexible, bendable and tailorable, it can be easily and conformally attached to an in-planar surface on human body as wearable heater with good coverage. As displayed in Fig 6.14c, one of the fingers is wrapped with the e-textiles. When applied with a low voltage of 3V, the temperature of e-textiles is quickly increased in several seconds, and the heat dissipated from the e-textiles heater can be efficiently transferred to the human skin because of the conformal contact, which shows advantage of energy saving. Furthermore, by virtue of clinging to certain parts of human body, this wearable heater can increase blood flow and speed up the rehabilitation, thus promising the huge potentials as wearable thermal therapy devices.

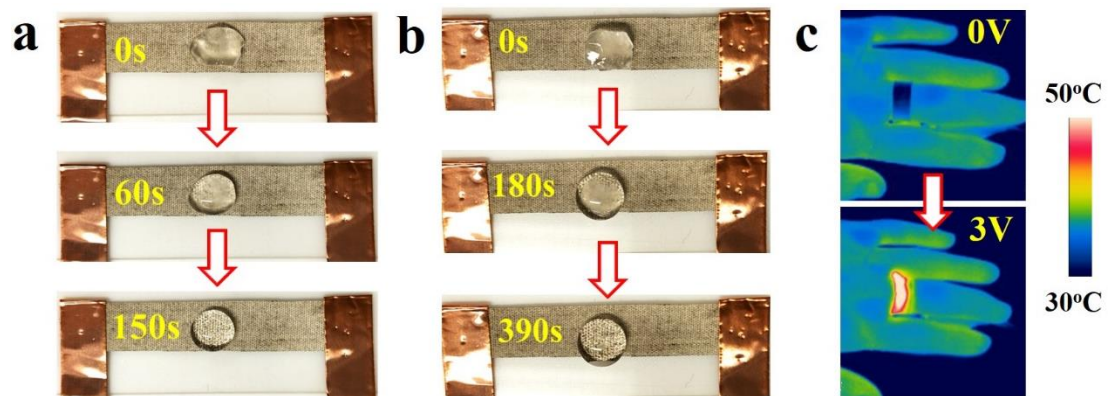


Fig 6.14 The deicing performance of the e-textiles applied (a) with a voltage of 3V and (b) without voltage. (c) IR images of the e-textiles attached on the human finger as wearable heater before and after the applying of a 3V voltage.

6.4 Conclusions

In summary, a highly conductive and superhydrophobic e-textile was prepared based on a facile and efficient method. Dense AgNPs were successfully deposited onto the fabric substrate by electroless plating with the aid of bioinspired PDA, where PDA serves as adhesive layer to tightly bridge the fabric substrate and AgNPs, and on the other hand, a thin layer of PFDT was further applied to endow the e-textiles excellent waterproof capability. In addition to the high conductivity of 233.4 S/cm, the superhydrophobic e-textiles also exhibited remarkable repellence to acid, alkaline solution as well as common liquid foods, thus can be used in wet and other harsh conditions. In addition, the as-made e-textiles showed a superb electromechanical stability, which is able to withstand multicycles ultrasonication and even machine washing, with well-preserved conductivity and waterproof capability. Besides the application as conductive interconnects, the e-textiles demonstrated the wearable applications as bending strain sensor, which can respond to different mechanical bending with a GF of 7.1. Moreover, the high conductivity of the e-textile makes it to be used as an efficient wearable heater. The temperature could increase quickly to more than 50 °C at a relatively low voltage of 3 V, endowing the e-textiles good deicing performance and promising potentials to be applied in thermal therapy. At last, it is worth noting that all the preparation process can be completed in solution without the need of any extreme condition, which can be extended to other e-textiles, thus showing great possibility for scalable production for wearable electronics.

CHAPTER 7: Conclusions and outlook

7.1 Conclusions

In this thesis, flexible and wearable strain sensors have been developed through the proper utilization of conductive materials, polymer substrate and especially the surface modification by mussel inspired PDA. Two kinds of textile-based strain sensors with excellent wearability have been fabricated based on weaving the 1D yarn sensor or directly depositing AgNPs on fabric. The structures, chemical/physical properties, electromechanical performance were characterized.

First, we developed a new 1D coaxial yarn strain sensor consisting of an elastic PUY core, an rGO conductive sheath and PDA package layers. Importantly, the results demonstrate that the dopamine molecules can reach the exposed rGO surface and self-polymerize into a continuous PDA film, thus greatly enhancing the interfacial adhesion between PUY core and rGO sheath, the stability of the sensing layer and the integrality of the sensor. Consequently, the yarn sensor exhibits high sensitivity with a GF of 131.8 at 90% strain, excellent linearity and very low hysteresis behavior, especially superior durability up to 30000 stretching–releasing cycles.

Second, the sensing mechanism of the as-made 1D yarn strain sensor was studied by

recording the cracks morphologies under different strains using SEM, as well as voltage drop simulation by a FEA method. It is proved that the resistance increase of the sensor should be attributed to the crack formation on the conductive rGO layer under stretching strains. In addition, prestretching was demonstrated as an effective method to adjust the electro-mechanical properties of the yarn strain sensor, which is beneficial to higher sensitivity, lower hysteresis and repeatability errors. Furthermore, benefiting from the reasonable design of structure and material system, the yarn strain sensor is proved to possess a good capability to sense multiple mechanical deformations of stretching and bending.

Third, we designed a wearable fabric strain sensor by integrating the yarn sensor into fabric structures like the common elastic yarn for fabricating strain sensing textiles by using the mature textile technology easily. As expected, the sensing fabric presents very good and stable sensing performance even after 10000 dynamic cycles, which can be worn on the human body directly like a common functional textile/clothing without discomfort or other negative effects, showing great potential for application as a real wearable system in long-term monitoring of human motion and conditions.

Fourth, we developed a highly conductive, stable and waterproof e-textile based on the common cotton fabric. It is found that, with the modification of PDA in advance, a dense and compact AgNPs layer can be uniformly formed on the surface of all cotton fibers, resulting in a perfect 3D conductive network. In addition, by further modification

with a fluorine containing agent of PHDT solution, a superhydrophobic surface was granted to the e-textiles, showing a water contact angle as high as 152°. Furthermore, with the aid of enhanced interface as well as superhydrophobic surface, the e-textiles not only present outstanding stability to mechanical deformations including ultrasonication and even machine washing, but also display excellent environmental stability with notable anti-corrosion to water, acid/alkaline solution and food liquid staining. As for wearable applications, the e-textiles can be used as wearable strain sensors to detect mechanical bending. Moreover, the e-textiles possess notable Joule heating efficiency, showing huge potentials as wearable heater for thermal therapy.

In summary, two kinds of wearable textile-based strain sensors have been successfully developed by weaving the 1D yarn strain sensor into the fabric or directly depositing conductive materials on fabric. These strain sensors demonstrate notable electromechanical properties and especially notable wearability, and of great importance is the introduction of bioinspired PDA as encapsulation or interface reinforcer, endowing the greatly enhanced adhesion between conductive materials and the soft fabric substrate, and finally greatly improving the durability of the strain sensors for long-term human motion detection. This systematic study can well serve as a guide to develop more wearable electronics in the future.

7.2 Outlook

Despite that flexible and wearable strain sensors were successfully designed and fabricated in this work, some limitations are still needed to be improved in the future work, which are summarized in the following aspects:

1. As for the PDA strategy, the long time for PDA formation in this research makes it difficult to scalable and fast fabrication. Generally, the PDA coating can be formed at normal conditions, without using high temperature, pressure, vacuum etc. Commonly, the maximum thickness of PDA layer within 24 hours is believed to be ca. 50 nm. Moreover, considering the PDA deposition mainly a redox process, besides the duration time, the deposition speed of PDA is also greatly related to some other conditions, including the introduction of oxidant, pH value, and deposition conditions. For example, it was reported that many chemical oxidants including periodate, copper cations, and hydrogen peroxide can be applied to greatly accelerate the deposition process. In addition, the UV irradiation and some enzymes, such as laccase and tyrosinase, can also facilitate the PDA deposition process. Therefore, the duration time of the PDA formation should be reduced to a short level in accordance with the application fields.
2. For the fabric sensor integrated with 1D strain sensor, it has been proved that the sensing properties of the strain sensor are greatly influenced by the fabric structure, the friction of the fabric, and fabrication process, which makes it complicated to predict the electro-mechanical behavior of the fabric sensor. Hence further work will focus on the

systematic study of the effect of different fabric structures, including the sateen, plain, honeycomb and so forth, and improvement should be put forward to reach the full potential of integrated 1D strain sensors.

3. Although a highly conductive e-textile has been developed, the cotton fabrics used present very limited stretchability, making it difficult to detect large strain human motions like arm and leg bending. Therefore, e-textiles based on highly stretchable fabric should be explored, and the electro-mechanical properties of this e-textile as well as the sensing mechanism under stretching require further systematical investigation. In addition to the application as strain sensors, multifunction including gas, humidity and sweat detection has become a research hotspot recently, and attempt should be focused on coupling two or more functions together to accomplish the detection of various stimulus by only one sensing device.

4. The real applications of the strain sensors should contain some other electrical parts, such as the power supply, communication devices, and electrical signal collection and processing unit. However, this research work only places emphasis on the fabrication and electro-mechanical properties of the strain sensors rather than the full integration with other parts for independent and continuous human motion detection. Therefore, further work should explore the integration of the strain sensor with other function parts, at the same time the small size, light weight, wearing safety and comfort of the integrated device should also in consideration.

REFERENCES

- [1] Amjadi, M.; Kyung, K. U.; Park, I.; Sitti, M. Stretchable, skin-mountable, and wearable strain sensors and their potential applications: a review. *Advanced Functional Materials* **2016**, *26*, 1678-1698,
- [2] Zhao, S.; Li, J.; Cao, D.; Zhang, G.; Li, J.; Li, K.; Yang, Y.; Wang, W.; Jin, Y.; Sun, R. Recent advancements in flexible and stretchable electrodes for electromechanical sensors: strategies, materials, and features. *ACS applied materials & interfaces* **2017**, *9*, 12147-12164,
- [3] Segev-Bar, M.; Haick, H. Flexible sensors based on nanoparticles. *ACS nano* **2013**, *7*, 8366-8378,
- [4] Park, J.; You, I.; Shin, S.; Jeong, U. Material approaches to stretchable strain sensors. *ChemPhysChem* **2015**, *16*, 1155-1163,
- [5] Wu, S.; Peng, S.; Yu, Y.; Wang, C. H. Strategies for Designing Stretchable Strain Sensors and Conductors. *Advanced Materials Technologies* **2020**, *5*, 1900908,
- [6] Lin, L.; Liu, S.; Zhang, Q.; Li, X.; Ji, M.; Deng, H.; Fu, Q. Towards tunable sensitivity of electrical property to strain for conductive polymer composites based on thermoplastic elastomer. *ACS applied materials & interfaces* **2013**, *5*, 5815-5824,
- [7] Liu, H.; Gao, J.; Huang, W.; Dai, K.; Zheng, G.; Liu, C.; Shen, C.; Yan, X.; Guo, J.; Guo, Z. Electrically conductive strain sensing polyurethane nanocomposites with synergistic carbon nanotubes and graphene bifillers. *Nanoscale* **2016**, *8*, 12977-12989,
- [8] Sang, Z.; Ke, K.; Manas-Zloczower, I. Interface design strategy for the fabrication of highly stretchable strain sensors. *ACS applied materials & interfaces* **2018**, *10*, 36483-36492,
- [9] Deng, H.; Ji, M.; Yan, D.; Fu, S.; Duan, L.; Zhang, M.; Fu, Q. Towards tunable resistivity–strain behavior through construction of oriented and selectively distributed conductive networks in conductive polymer composites. *Journal of Materials Chemistry A* **2014**, *2*, 10048-10058,

REFERENCES

- [10] Li, J.; Zhao, S.; Zeng, X.; Huang, W.; Gong, Z.; Zhang, G.; Sun, R.; Wong, C.-P. Highly stretchable and sensitive strain sensor based on facilely prepared three-dimensional graphene foam composite. *ACS applied materials & interfaces* **2016**, *8*, 18954-18961,
- [11] Deng, H.; Lin, L.; Ji, M.; Zhang, S.; Yang, M.; Fu, Q. Progress on the morphological control of conductive network in conductive polymer composites and the use as electroactive multifunctional materials. *Progress in Polymer Science* **2014**, *39*, 627-655,
- [12] Bauhofer, W.; Kovacs, J. Z. A review and analysis of electrical percolation in carbon nanotube polymer composites. *Composites Science and Technology* **2009**, *69*, 1486-1498,
- [13] Alig, I.; Pötschke, P.; Lellinger, D.; Skipa, T.; Pegel, S.; Kasaliwal, G. R.; Villmow, T. Establishment, morphology and properties of carbon nanotube networks in polymer melts. *Polymer* **2012**, *53*, 4-28,
- [14] Chen, J.; Yu, Q.; Cui, X.; Dong, M.; Zhang, J.; Wang, C.; Fan, J.; Zhu, Y.; Guo, Z. An overview of stretchable strain sensors from conductive polymer nanocomposites. *Journal of Materials Chemistry C* **2019**, *7*, 11710-11730,
- [15] Liu, Y.; Wu, F.; Zhao, X.; Liu, M. High-performance strain sensors based on spirally structured composites with carbon black, chitin nanocrystals, and natural rubber. *ACS Sustainable Chemistry & Engineering* **2018**, *6*, 10595-10605,
- [16] Cooper, C. B.; Arutselvan, K.; Liu, Y.; Armstrong, D.; Lin, Y.; Khan, M. R.; Genzer, J.; Dickey, M. D. Stretchable capacitive sensors of torsion, strain, and touch using double helix liquid metal fibers. *Advanced Functional Materials* **2017**, *27*, 1605630,
- [17] Cai, L.; Song, L.; Luan, P.; Zhang, Q.; Zhang, N.; Gao, Q.; Zhao, D.; Zhang, X.; Tu, M.; Yang, F. Super-stretchable, transparent carbon nanotube-based capacitive strain sensors for human motion detection. *Scientific reports* **2013**, *3*, 1-9,
- [18] Li, Y.; Zhou, B.; Zheng, G.; Liu, X.; Li, T.; Yan, C.; Cheng, C.; Dai, K.; Liu, C.; Shen, C. Continuously prepared highly conductive and stretchable SWNT/MWNT synergistically composited electrospun thermoplastic polyurethane yarns for wearable

REFERENCES

- sensing. *Journal of Materials Chemistry C* **2018**, *6*, 2258-2269,
- [19] Zhou, J.; Xu, X.; Xin, Y.; Lubineau, G. Coaxial thermoplastic elastomer-wrapped carbon nanotube fibers for deformable and wearable strain sensors. *Advanced Functional Materials* **2018**, *28*, 1705591,
- [20] Hu, N.; Fukunaga, H.; Atobe, S.; Liu, Y.; Li, J. Piezoresistive strain sensors made from carbon nanotubes based polymer nanocomposites. *Sensors* **2011**, *11*, 10691-10723,
- [21] Wang, Y.; Jia, Y.; Zhou, Y.; Wang, Y.; Zheng, G.; Dai, K.; Liu, C.; Shen, C. Ultra-stretchable, sensitive and durable strain sensors based on polydopamine encapsulated carbon nanotubes/elastic bands. *Journal of Materials Chemistry C* **2018**, *6*, 8160-8170,
- [22] Lipomi, D. J.; Vosgueritchian, M.; Tee, B. C.; Hellstrom, S. L.; Lee, J. A.; Fox, C. H.; Bao, Z. Skin-like pressure and strain sensors based on transparent elastic films of carbon nanotubes. *Nature nanotechnology* **2011**, *6*, 788-792,
- [23] Xu, M.; Qi, J.; Li, F.; Zhang, Y. Highly stretchable strain sensors with reduced graphene oxide sensing liquids for wearable electronics. *Nanoscale* **2018**, *10*, 5264-5271,
- [24] Yang, Z.; Wang, D.-Y.; Pang, Y.; Li, Y.-X.; Wang, Q.; Zhang, T.-Y.; Wang, J.-B.; Liu, X.; Yang, Y.-Y.; Jian, J.-M. Simultaneously detecting subtle and intensive human motions based on a silver nanoparticles bridged graphene strain sensor. *ACS applied materials & interfaces* **2018**, *10*, 3948-3954,
- [25] Bae, S.-H.; Lee, Y.; Sharma, B. K.; Lee, H.-J.; Kim, J.-H.; Ahn, J.-H. Graphene-based transparent strain sensor. *Carbon* **2013**, *51*, 236-242,
- [26] Wang, Y.; Hao, J.; Huang, Z.; Zheng, G.; Dai, K.; Liu, C.; Shen, C. Flexible electrically resistive-type strain sensors based on reduced graphene oxide-decorated electrospun polymer fibrous mats for human motion monitoring. *Carbon* **2018**, *126*, 360-371,
- [27] Jing, Z.; Guang-Yu, Z.; Dong-Xia, S. Review of graphene-based strain sensors. *Chinese Physics B* **2013**, *22*, 057701,
- [28] Wang, Y.; Wang, L.; Yang, T.; Li, X.; Zang, X.; Zhu, M.; Wang, K.; Wu, D.; Zhu, H. Wearable and highly sensitive graphene strain sensors for human motion monitoring.

REFERENCES

- Advanced Functional Materials* **2014**, *24*, 4666-4670,
- [29] Nel, A.; Xia, T.; Meng, H.; Wang, X.; Lin, S.; Ji, Z.; Zhang, H. Nanomaterial toxicity testing in the 21st century: use of a predictive toxicological approach and high-throughput screening. *Accounts of chemical research* **2013**, *46*, 607-621,
- [30] Amjadi, M.; Pichitpajongkit, A.; Lee, S.; Ryu, S.; Park, I. Highly stretchable and sensitive strain sensor based on silver nanowire–elastomer nanocomposite. *ACS nano* **2014**, *8*, 5154-5163,
- [31] Li, X.; Hu, H.; Hua, T.; Xu, B.; Jiang, S. Wearable strain sensing textile based on one-dimensional stretchable and weavable yarn sensors. *Nano Research* **2018**, *11*, 5799-5811,
- [32] Gong, S.; Schwalb, W.; Wang, Y.; Chen, Y.; Tang, Y.; Si, J.; Shirinzadeh, B.; Cheng, W. A wearable and highly sensitive pressure sensor with ultrathin gold nanowires. *Nature communications* **2014**, *5*, 1-8,
- [33] Xiao, X.; Yuan, L.; Zhong, J.; Ding, T.; Liu, Y.; Cai, Z.; Rong, Y.; Han, H.; Zhou, J.; Wang, Z. L. High-strain sensors based on ZnO nanowire/polystyrene hybridized flexible films. *Advanced materials* **2011**, *23*, 5440-5444,
- [34] Lee, T.; Lee, W.; Kim, S. W.; Kim, J. J.; Kim, B. S. Flexible textile strain wireless sensor functionalized with hybrid carbon nanomaterials supported ZnO nanowires with controlled aspect ratio. *Advanced Functional Materials* **2016**, *26*, 6206-6214,
- [35] Li, Y.; Cheng, X.; Leung, M.; Tsang, J.; Tao, X.; Yuen, M. A flexible strain sensor from polypyrrole-coated fabrics. *Synthetic metals* **2005**, *155*, 89-94,
- [36] Li, M.; Li, H.; Zhong, W.; Zhao, Q.; Wang, D. Stretchable conductive polypyrrole/polyurethane (PPy/PU) strain sensor with netlike microcracks for human breath detection. *ACS applied materials & interfaces* **2014**, *6*, 1313-1319,
- [37] Lee, Y. Y.; Kang, H. Y.; Gwon, S. H.; Choi, G. M.; Lim, S. M.; Sun, J. Y.; Joo, Y. C. A strain-insensitive stretchable electronic conductor: PEDOT: PSS/acrylamide organogels. *Advanced materials* **2016**, *28*, 1636-1643,
- [38] Teng, C.; Lu, X.; Zhu, Y.; Wan, M.; Jiang, L. Polymer in situ embedding for highly flexible, stretchable and water stable PEDOT: PSS composite conductors. *Rsc*

REFERENCES

- Advances* **2013**, *3*, 7219-7223,
- [39] Duan, S.; Wang, Z.; Zhang, L.; Liu, J.; Li, C. Three-dimensional highly stretchable conductors from elastic fiber mat with conductive polymer coating. *ACS applied materials & interfaces* **2017**, *9*, 30772-30778,
- [40] Chossat, J.-B.; Park, Y.-L.; Wood, R. J.; Duchaine, V. A soft strain sensor based on ionic and metal liquids. *Ieee sensors journal* **2013**, *13*, 3405-3414,
- [41] Frutiger, A.; Muth, J. T.; Vogt, D. M.; Mengüç, Y.; Campo, A.; Valentine, A. D.; Walsh, C. J.; Lewis, J. A. Capacitive soft strain sensors via multicore-shell fiber printing. *Advanced Materials* **2015**, *27*, 2440-2446,
- [42] Choi, D. Y.; Kim, M. H.; Oh, Y. S.; Jung, S.-H.; Jung, J. H.; Sung, H. J.; Lee, H. W.; Lee, H. M. Highly stretchable, hysteresis-free ionic liquid-based strain sensor for precise human motion monitoring. *ACS applied materials & interfaces* **2017**, *9*, 1770-1780,
- [43] Zhu, Y.; Chao, C.; Cheng, C.-H.; Leung, W. W.-F. A novel ionic-liquid strain sensor for large-strain applications. *Ieee electron device letters* **2009**, *30*, 337-339,
- [44] Liu, C.; Han, S.; Xu, H.; Wu, J.; Liu, C. Multifunctional highly sensitive multiscale stretchable strain sensor based on a Graphene/Glycerol-KCl synergistic conductive network. *ACS applied materials & interfaces* **2018**, *10*, 31716-31724,
- [45] Zhang, Y.-Z.; Lee, K. H.; Anjum, D. H.; Sougrat, R.; Jiang, Q.; Kim, H.; Alshareef, H. N. MXenes stretch hydrogel sensor performance to new limits. *Science advances* **2018**, *4*, eaat0098,
- [46] Cai, Y.; Shen, J.; Ge, G.; Zhang, Y.; Jin, W.; Huang, W.; Shao, J.; Yang, J.; Dong, X. Stretchable Ti₃C₂T_x MXene/carbon nanotube composite based strain sensor with ultrahigh sensitivity and tunable sensing range. *ACS nano* **2018**, *12*, 56-62,
- [47] Ma, Y.; Liu, N.; Li, L.; Hu, X.; Zou, Z.; Wang, J.; Luo, S.; Gao, Y. A highly flexible and sensitive piezoresistive sensor based on MXene with greatly changed interlayer distances. *Nature communications* **2017**, *8*, 1-8,
- [48] Allen, M. J.; Tung, V. C.; Kaner, R. B. Honeycomb carbon: a review of graphene. *Chemical reviews* **2010**, *110*, 132-145,

REFERENCES

- [49] De Volder, M. F.; Tawfick, S. H.; Baughman, R. H.; Hart, A. J. Carbon nanotubes: present and future commercial applications. *science* **2013**, *339*, 535-539,
- [50] Novoselov, K. S.; Fal, V.; Colombo, L.; Gellert, P.; Schwab, M.; Kim, K. A roadmap for graphene. *nature* **2012**, *490*, 192-200,
- [51] Kumar, D.; Sharma, R. Advances in conductive polymers. *European polymer journal* **1998**, *34*, 1053-1060,
- [52] Shi, Y.; Peng, L.; Ding, Y.; Zhao, Y.; Yu, G. Nanostructured conductive polymers for advanced energy storage. *Chemical Society Reviews* **2015**, *44*, 6684-6696,
- [53] Roh, E.; Hwang, B.-U.; Kim, D.; Kim, B.-Y.; Lee, N.-E. Stretchable, transparent, ultrasensitive, and patchable strain sensor for human-machine interfaces comprising a nanohybrid of carbon nanotubes and conductive elastomers. *ACS nano* **2015**, *9*, 6252-6261,
- [54] Wang, X.; Gu, Y.; Xiong, Z.; Cui, Z.; Zhang, T. Silk-molded flexible, ultrasensitive, and highly stable electronic skin for monitoring human physiological signals. *Advanced materials* **2014**, *26*, 1336-1342,
- [55] Mannsfeld, S. C.; Tee, B. C.; Stoltenberg, R. M.; Chen, C. V. H.; Barman, S.; Muir, B. V.; Sokolov, A. N.; Reese, C.; Bao, Z. Highly sensitive flexible pressure sensors with microstructured rubber dielectric layers. *Nature materials* **2010**, *9*, 859-864,
- [56] Yu, X.-G.; Li, Y.-Q.; Zhu, W.-B.; Huang, P.; Wang, T.-T.; Hu, N.; Fu, S.-Y. A wearable strain sensor based on a carbonized nano-sponge/silicone composite for human motion detection. *Nanoscale* **2017**, *9*, 6680-6685,
- [57] Wang, C.; Li, X.; Gao, E.; Jian, M.; Xia, K.; Wang, Q.; Xu, Z.; Ren, T.; Zhang, Y. Carbonized silk fabric for ultrastretchable, highly sensitive, and wearable strain sensors. *Advanced materials* **2016**, *28*, 6640-6648,
- [58] Boland, C. S.; Khan, U.; Backes, C.; O'Neill, A.; McCauley, J.; Duane, S.; Shanker, R.; Liu, Y.; Jurewicz, I.; Dalton, A. B. Sensitive, high-strain, high-rate bodily motion sensors based on graphene-rubber composites. *ACS nano* **2014**, *8*, 8819-8830,
- [59] Wang, L.; Wang, H.; Huang, X.-W.; Song, X.; Hu, M.; Tang, L.; Xue, H.; Gao, J. Superhydrophobic and superelastic conductive rubber composite for wearable strain

REFERENCES

- sensors with ultrahigh sensitivity and excellent anti-corrosion property. *Journal of Materials Chemistry A* **2018**, *6*, 24523-24533,
- [60] Wang, X.; Meng, S.; Tebyetekerwa, M.; Li, Y.; Pionteck, J.; Sun, B.; Qin, Z.; Zhu, M. Highly sensitive and stretchable piezoresistive strain sensor based on conductive poly (styrene-butadiene-styrene)/few layer graphene composite fiber. *Composites Part A: Applied Science and Manufacturing* **2018**, *105*, 291-299,
- [61] Li, X.; Hua, T.; Xu, B. Electromechanical properties of a yarn strain sensor with graphene-sheath/polyurethane-core. *Carbon* **2017**, *118*, 686-698,
- [62] Liu, Y.-J.; Cao, W.-T.; Ma, M.-G.; Wan, P. Ultrasensitive wearable soft strain sensors of conductive, self-healing, and elastic hydrogels with synergistic “soft and hard” hybrid networks. *ACS applied materials & interfaces* **2017**, *9*, 25559-25570,
- [63] Cai, G.; Wang, J.; Qian, K.; Chen, J.; Li, S.; Lee, P. S. Extremely stretchable strain sensors based on conductive self-healing dynamic cross-links hydrogels for human-motion detection. *Advanced Science* **2017**, *4*, 1600190,
- [64] Wang, T.; Zhang, Y.; Liu, Q.; Cheng, W.; Wang, X.; Pan, L.; Xu, B.; Xu, H. A self-healable, highly stretchable, and solution processable conductive polymer composite for ultrasensitive strain and pressure sensing. *Advanced Functional Materials* **2018**, *28*, 1705551,
- [65] Cohen, D. J.; Mitra, D.; Peterson, K.; Maharbiz, M. M. A highly elastic, capacitive strain gauge based on percolating nanotube networks. *Nano letters* **2012**, *12*, 1821-1825,
- [66] Zhou, K.; Zhao, Y.; Sun, X.; Yuan, Z.; Zheng, G.; Dai, K.; Mi, L.; Pan, C.; Liu, C.; Shen, C. Ultra-stretchable triboelectric nanogenerator as high-sensitive and self-powered electronic skins for energy harvesting and tactile sensing. *Nano Energy* **2020**, *70*, 104546,
- [67] Deng, C.; Tang, W.; Liu, L.; Chen, B.; Li, M.; Wang, Z. L. Self-Powered Insole Plantar Pressure Mapping System. *Advanced Functional Materials* **2018**, *28*, 1801606,
- [68] Yi, F.; Zhang, Z.; Kang, Z.; Liao, Q.; Zhang, Y. Recent advances in triboelectric nanogenerator-based health monitoring. *Advanced Functional Materials* **2019**, *29*, 1808849,

REFERENCES

- [69] Wen, F.; Sun, Z.; He, T.; Shi, Q.; Zhu, M.; Zhang, Z.; Li, L.; Zhang, T.; Lee, C. Machine Learning Glove Using Self-Powered Conductive Superhydrophobic Triboelectric Textile for Gesture Recognition in VR/AR Applications. *Advanced Science* **2020**, *7*, 2000261,
- [70] Fan, F.-R.; Lin, L.; Zhu, G.; Wu, W.; Zhang, R.; Wang, Z. L. Transparent triboelectric nanogenerators and self-powered pressure sensors based on micropatterned plastic films. *Nano letters* **2012**, *12*, 3109-3114,
- [71] Zeng, W.; Shu, L.; Li, Q.; Chen, S.; Wang, F.; Tao, X. M. Fiber-based wearable electronics: a review of materials, fabrication, devices, and applications. *Advanced materials* **2014**, *26*, 5310-5336,
- [72] Li, Y.; Luo, S.; Yang, M. C.; Liang, R.; Zeng, C. Poisson Ratio and Piezoresistive Sensing: A New Route to High-Performance 3D Flexible and Stretchable Sensors of Multimodal Sensing Capability. *Advanced Functional Materials* **2016**, *26*, 2900-2908,
- [73] Jeong, Y. R.; Park, H.; Jin, S. W.; Hong, S. Y.; Lee, S. S.; Ha, J. S. Highly stretchable and sensitive strain sensors using fragmented graphene foam. *Advanced Functional Materials* **2015**, *25*, 4228-4236,
- [74] Wang, L.; Wang, D.; Wu, Z.; Luo, J.; Huang, X.; Gao, Q.; Lai, X.; Tang, L.-C.; Xue, H.; Gao, J. Self-Derived Superhydrophobic and Multifunctional Polymer Sponge Composite with Excellent Joule Heating and Photothermal Performance for Strain/Pressure Sensors. *ACS Applied Materials & Interfaces* **2020**, *12*, 13316-13326,
- [75] Cao, J.; Wang, Q.; Dai, H. Electromechanical properties of metallic, quasimetallic, and semiconducting carbon nanotubes under stretching. *Physical review letters* **2003**, *90*, 157601,
- [76] Zhou, J.; Gu, Y.; Fei, P.; Mai, W.; Gao, Y.; Yang, R.; Bao, G.; Wang, Z. L. Flexible piezotronic strain sensor. *Nano letters* **2008**, *8*, 3035-3040,
- [77] Hempel, M.; Nezich, D.; Kong, J.; Hofmann, M. A novel class of strain gauges based on layered percolative films of 2D materials. *Nano letters* **2012**, *12*, 5714-5718,
- [78] Chortos, A.; Bao, Z. Skin-inspired electronic devices. *Materials Today* **2014**, *17*, 321-331,

REFERENCES

- [79] Yu, S.; Wang, X.; Xiang, H.; Tebyetekerwa, M.; Zhu, M. 1-D polymer ternary composites: Understanding materials interaction, percolation behaviors and mechanism toward ultra-high stretchable and super-sensitive strain sensors. *Science China Materials* **2019**, *62*, 995-1004,
- [80] Li, B.; Luo, J.; Huang, X.; Lin, L.; Wang, L.; Hu, M.; Tang, L.; Xue, H.; Gao, J.; Mai, Y.-W. A highly stretchable, super-hydrophobic strain sensor based on polydopamine and graphene reinforced nanofiber composite for human motion monitoring. *Composites Part B: Engineering* **2020**, *181*, 107580,
- [81] Khang, D.-Y.; Jiang, H.; Huang, Y.; Rogers, J. A. A stretchable form of single-crystal silicon for high-performance electronics on rubber substrates. *Science* **2006**, *311*, 208-212,
- [82] Rogers, J. A.; Huang, Y. A curvy, stretchy future for electronics. *Proceedings of the National Academy of Sciences* **2009**, *106*, 10875-10876,
- [83] Yamada, T.; Hayamizu, Y.; Yamamoto, Y.; Yomogida, Y.; Izadi-Najafabadi, A.; Futaba, D. N.; Hata, K. A stretchable carbon nanotube strain sensor for human-motion detection. *Nature nanotechnology* **2011**, *6*, 296,
- [84] Park, S. J.; Kim, J.; Chu, M.; Khine, M. Highly flexible wrinkled carbon nanotube thin film strain sensor to monitor human movement. *Advanced Materials Technologies* **2016**, *1*, 1600053,
- [85] Feng, X.; Yang, B. D.; Liu, Y.; Wang, Y.; Dagdeviren, C.; Liu, Z.; Carlson, A.; Li, J.; Huang, Y.; Rogers, J. A. Stretchable ferroelectric nanoribbons with wavy configurations on elastomeric substrates. *Acs Nano* **2011**, *5*, 3326-3332,
- [86] Wang, X.; Hu, H.; Shen, Y.; Zhou, X.; Zheng, Z. Stretchable conductors with ultrahigh tensile strain and stable metallic conductance enabled by prestrained polyelectrolyte nanoplateforms. *Advanced Materials* **2011**, *23*, 3090-3094,
- [87] Xu, F.; Lu, W.; Zhu, Y. Controlled 3D buckling of silicon nanowires for stretchable electronics. *Acs Nano* **2011**, *5*, 672-678,
- [88] Yao, S.; Zhu, Y. Wearable multifunctional sensors using printed stretchable conductors made of silver nanowires. *Nanoscale* **2014**, *6*, 2345-2352,

REFERENCES

- [89] Kang, D.; Pikhitsa, P. V.; Choi, Y. W.; Lee, C.; Shin, S. S.; Piao, L.; Park, B.; Suh, K.-Y.; Kim, T.-i.; Choi, M. Ultrasensitive mechanical crack-based sensor inspired by the spider sensory system. *Nature* **2014**, *516*, 222-226,
- [90] Zhao, S.; Guo, L.; Li, J.; Li, N.; Zhang, G.; Gao, Y.; Li, J.; Cao, D.; Wang, W.; Jin, Y. Binary synergistic sensitivity strengthening of bioinspired hierarchical architectures based on fragmentized reduced graphene oxide sponge and silver nanoparticles for strain sensors and beyond. *Small* **2017**, *13*, 1700944,
- [91] Liao, X.; Zhang, Z.; Kang, Z.; Gao, F.; Liao, Q.; Zhang, Y. Ultrasensitive and stretchable resistive strain sensors designed for wearable electronics. *Materials Horizons* **2017**, *4*, 502-510,
- [92] Yang, Y.; Huang, Q.; Niu, L.; Wang, D.; Yan, C.; She, Y.; Zheng, Z. Waterproof, ultrahigh areal-capacitance, wearable supercapacitor fabrics. *Advanced Materials* **2017**, *29*, 1606679,
- [93] Lu, H.; Chen, J.; Tian, Q. Wearable high-performance supercapacitors based on Ni-coated cotton textile with low-crystalline Ni-Al layered double hydroxide nanoparticles. *Journal of colloid and interface science* **2018**, *513*, 342-348,
- [94] Pu, J.-H.; Zha, X.-J.; Zhao, M.; Li, S.; Bao, R.-Y.; Liu, Z.-Y.; Xie, B.-H.; Yang, M.-B.; Guo, Z.; Yang, W. 2D end-to-end carbon nanotube conductive networks in polymer nanocomposites: a conceptual design to dramatically enhance the sensitivities of strain sensors. *Nanoscale* **2018**, *10*, 2191-2198,
- [95] Niu, B.; Hua, T.; Hu, H.; Xu, B.; Tian, X.; Chan, K.; Chen, S. A highly durable textile-based sensor as a human-worn material interface for long-term multiple mechanical deformation sensing. *Journal of Materials Chemistry C* **2019**, *7*, 14651-14663,
- [96] Zhang, H.; Tao, X.; Yu, T.; Wang, S.; Cheng, X. A novel sensate 'string' for large-strain measurement at high temperature. *Measurement Science and technology* **2006**, *17*, 450,
- [97] Cheng, Y.; Wang, R.; Sun, J.; Gao, L. A stretchable and highly sensitive graphene-based fiber for sensing tensile strain, bending, and torsion. *Advanced materials* **2015**,

REFERENCES

27, 7365-7371,

[98] Li, L.; Bai, Y.; Li, L.; Wang, S.; Zhang, T. A superhydrophobic smart coating for flexible and wearable sensing electronics. *Advanced Materials* **2017**, *29*, 1702517,

[99] Wang, L.; Chen, Y.; Lin, L.; Wang, H.; Huang, X.; Xue, H.; Gao, J. Highly stretchable, anti-corrosive and wearable strain sensors based on the PDMS/CNTs decorated elastomer nanofiber composite. *Chemical Engineering Journal* **2019**, *362*, 89-98,

[100] Zheng, Y.; Li, Y.; Zhou, Y.; Dai, K.; Zheng, G.; Zhang, B.; Liu, C.; Shen, C. High-Performance Wearable Strain Sensor Based on Graphene/Cotton Fabric with High Durability and Low Detection Limit. *ACS Applied Materials & Interfaces* **2019**, *12*, 1474-1485,

[101] Yang, Z.; Pang, Y.; Han, X.-l.; Yang, Y.; Ling, J.; Jian, M.; Zhang, Y.; Yang, Y.; Ren, T.-L. Graphene textile strain sensor with negative resistance variation for human motion detection. *ACS nano* **2018**, *12*, 9134-9141,

[102] Liu, Z.; Qi, D.; Leow, W. R.; Yu, J.; Xiloyannis, M.; Cappello, L.; Liu, Y.; Zhu, B.; Jiang, Y.; Chen, G. 3D-Structured Stretchable Strain Sensors for Out-of-Plane Force Detection. *Advanced Materials* **2018**, *30*, 1707285,

[103] Chen, S.; Song, Y.; Ding, D.; Ling, Z.; Xu, F. Flexible and anisotropic strain sensor based on carbonized crepe paper with aligned cellulose fibers. *Advanced Functional Materials* **2018**, *28*, 1802547,

[104] Wang, Z.; Huang, Y.; Sun, J.; Huang, Y.; Hu, H.; Jiang, R.; Gai, W.; Li, G.; Zhi, C. Polyurethane/cotton/carbon nanotubes core-spun yarn as high reliability stretchable strain sensor for human motion detection. *ACS applied materials & interfaces* **2016**, *8*, 24837-24843,

[105] Liu, S.; Zeng, T. H.; Hofmann, M.; Burcombe, E.; Wei, J.; Jiang, R.; Kong, J.; Chen, Y. Antibacterial activity of graphite, graphite oxide, graphene oxide, and reduced graphene oxide: membrane and oxidative stress. *ACS nano* **2011**, *5*, 6971-6980,

[106] Kang, S.; Herzberg, M.; Rodrigues, D. F.; Elimelech, M. Antibacterial effects of carbon nanotubes: size does matter! *Langmuir* **2008**, *24*, 6409-6413,

REFERENCES

- [107] Liu, Y.; Zhao, Y.; Sun, B.; Chen, C. Understanding the toxicity of carbon nanotubes. *Accounts of chemical research* **2013**, *46*, 702-713,
- [108] Zhao, X.; Liu, R. Recent progress and perspectives on the toxicity of carbon nanotubes at organism, organ, cell, and biomacromolecule levels. *Environment international* **2012**, *40*, 244-255,
- [109] Evans, K. E.; Alderson, A. Auxetic materials: functional materials and structures from lateral thinking! *Advanced materials* **2000**, *12*, 617-628,
- [110] Liu, Y.; Hu, H. A review on auxetic structures and polymeric materials. *Scientific Research and Essays* **2010**, *5*, 1052-1063,
- [111] Yang, T.; Wang, W.; Zhang, H.; Li, X.; Shi, J.; He, Y.; Zheng, Q.-s.; Li, Z.; Zhu, H. Tactile sensing system based on arrays of graphene woven microfibrils: electromechanical behavior and electronic skin application. *ACS nano* **2015**, *9*, 10867-10875,
- [112] Pang, C.; Lee, G.-Y.; Kim, T.-i.; Kim, S. M.; Kim, H. N.; Ahn, S.-H.; Suh, K.-Y. A flexible and highly sensitive strain-gauge sensor using reversible interlocking of nanofibres. *Nature materials* **2012**, *11*, 795-801,
- [113] Ha, M.; Lim, S.; Park, J.; Um, D. S.; Lee, Y.; Ko, H. Bioinspired interlocked and hierarchical design of ZnO nanowire arrays for static and dynamic pressure-sensitive electronic skins. *Advanced Functional Materials* **2015**, *25*, 2841-2849,
- [114] Park, J.; Lee, Y.; Hong, J.; Lee, Y.; Ha, M.; Jung, Y.; Lim, H.; Kim, S. Y.; Ko, H. Tactile-direction-sensitive and stretchable electronic skins based on human-skin-inspired interlocked microstructures. *ACS nano* **2014**, *8*, 12020-12029,
- [115] Kim, K. H.; Jang, N. S.; Ha, S. H.; Cho, J. H.; Kim, J. M. Highly sensitive and stretchable resistive strain sensors based on microstructured metal nanowire/elastomer composite films. *Small* **2018**, *14*, 1704232,
- [116] Liu, Z.; Qi, D.; Hu, G.; Wang, H.; Jiang, Y.; Chen, G.; Luo, Y.; Loh, X. J.; Liedberg, B.; Chen, X. Surface Strain Redistribution on Structured Microfibers to Enhance Sensitivity of Fiber-Shaped Stretchable Strain Sensors. *Advanced materials* **2018**, *30*, 1704229,

REFERENCES

- [117] Choi, S.; Yoon, K.; Lee, S.; Lee, H. J.; Lee, J.; Kim, D. W.; Kim, M. S.; Lee, T.; Pang, C. Conductive Hierarchical Hairy Fibers for Highly Sensitive, Stretchable, and Water-Resistant Multimodal Gesture-Distinguishable Sensor, VR Applications. *Advanced Functional Materials* **2019**, *29*, 1905808,
- [118] Jia, J.; Pu, J.-H.; Liu, J.-H.; Zhao, X.; Ke, K.; Bao, R.-Y.; Liu, Z.-Y.; Yang, M.-B.; Yang, W. Surface structure engineering for a bionic fiber-based sensor toward linear, tunable, and multifunctional sensing. *Materials Horizons* **2020**,
- [119] Jiang, Y.; Liu, Z.; Matsuhisa, N.; Qi, D.; Leow, W. R.; Yang, H.; Yu, J.; Chen, G.; Liu, Y.; Wan, C. Auxetic mechanical metamaterials to enhance sensitivity of stretchable strain sensors. *Advanced Materials* **2018**, *30*, 1706589,
- [120] Zhang, S. L.; Lai, Y. C.; He, X.; Liu, R.; Zi, Y.; Wang, Z. L. Auxetic foam-based contact-mode triboelectric nanogenerator with highly sensitive self-powered strain sensing capabilities to monitor human body movement. *Advanced functional materials* **2017**, *27*, 1606695,
- [121] Shi, J.; Li, X.; Cheng, H.; Liu, Z.; Zhao, L.; Yang, T.; Dai, Z.; Cheng, Z.; Shi, E.; Yang, L. Graphene reinforced carbon nanotube networks for wearable strain sensors. *Advanced Functional Materials* **2016**, *26*, 2078-2084,
- [122] Luo, S.; Liu, T. SWCNT/Graphite nanoplatelet hybrid thin films for self-temperature-compensated, highly sensitive, and extensible piezoresistive sensors. *Advanced Materials* **2013**, *25*, 5650-5657,
- [123] Oh, J. Y.; Jun, G. H.; Jin, S.; Ryu, H. J.; Hong, S. H. Enhanced electrical networks of stretchable conductors with small fraction of carbon nanotube/graphene hybrid fillers. *ACS applied materials & interfaces* **2016**, *8*, 3319-3325,
- [124] Liu, H.; Xiang, H.; Wang, Y.; Li, Z.; Qian, L.; Li, P.; Ma, Y.; Zhou, H.; Huang, W. A Flexible Multimodal Sensor That Detects Strain, Humidity, Temperature, and Pressure with Carbon Black and Reduced Graphene Oxide Hierarchical Composite on Paper. *ACS applied materials & interfaces* **2019**, *11*, 40613-40619,
- [125] Chen, S.; Wei, Y.; Wei, S.; Lin, Y.; Liu, L. Ultrasensitive cracking-assisted strain sensors based on silver nanowires/graphene hybrid particles. *ACS applied materials &*

REFERENCES

interfaces **2016**, *8*, 25563-25570,

[126] Li, Q.; Ullah, Z.; Li, W.; Guo, Y.; Xu, J.; Wang, R.; Zeng, Q.; Chen, M.; Liu, C.; Liu, L. Wide-Range Strain Sensors Based on Highly Transparent and Supremely Stretchable Graphene/Ag-Nanowires Hybrid Structures. *Small* **2016**, *12*, 5058-5065,

[127] Chen, S.; Wei, Y.; Yuan, X.; Lin, Y.; Liu, L. A highly stretchable strain sensor based on a graphene/silver nanoparticle synergic conductive network and a sandwich structure. *Journal of Materials Chemistry C* **2016**, *4*, 4304-4311,

[128] Liu, Z.; Fang, S.; Moura, F.; Ding, J.; Jiang, N.; Di, J.; Zhang, M.; Lepró, X.; Galvão, D.; Haines, C. Hierarchically buckled sheath-core fibers for superelastic electronics, sensors, and muscles. *Science* **2015**, *349*, 400-404,

[129] Xu, F.; Zhu, Y. Highly conductive and stretchable silver nanowire conductors. *Advanced materials* **2012**, *24*, 5117-5122,

[130] Xu, F.; Wang, X.; Zhu, Y.; Zhu, Y. Wavy ribbons of carbon nanotubes for stretchable conductors. *Advanced Functional Materials* **2012**, *22*, 1279-1283,

[131] Wei, Y.; Chen, S.; Yuan, X.; Wang, P.; Liu, L. Multiscale wrinkled microstructures for piezoresistive fibers. *Advanced Functional Materials* **2016**, *26*, 5078-5085,

[132] Sun, H.; Dai, K.; Zhai, W.; Zhou, Y.; Li, J.; Zheng, G.; Li, B.; Liu, C.; Shen, C. A highly sensitive and stretchable yarn strain sensor for human motion tracking utilizing a wrinkle-assisted crack structure. *ACS applied materials & interfaces* **2019**, *11*, 36052-36062,

[133] Zhou, Y.; Zhan, P.; Ren, M.; Zheng, G.; Dai, K.; Mi, L.; Liu, C.; Shen, C. Significant stretchability enhancement of a crack-based strain sensor combined with high sensitivity and superior durability for motion monitoring. *ACS applied materials & interfaces* **2019**, *11*, 7405-7414,

[134] Boryo, D. The effect of microbes on textile material: a review on the way-out so far. *The International Journal of Engineering and Science (IJES)* **2013**, *2*, 09-13,

[135] Yetisen, A. K.; Qu, H.; Manbachi, A.; Butt, H.; Dokmeci, M. R.; Hinstroza, J. P.; Skorobogatiy, M.; Khademhosseini, A.; Yun, S. H. Nanotechnology in textiles. *ACS nano* **2016**, *10*, 3042-3068,

REFERENCES

- [136] El-Khatib, E. Antimicrobial and self-cleaning textiles using nanotechnology. *Research Journal of Textile and Apparel* **2012**, *16*, 156,
- [137] Lin, L.; Wang, L.; Li, B.; Luo, J.; Huang, X.; Gao, Q.; Xue, H.; Gao, J. Dual conductive network enabled superhydrophobic and high performance strain sensors with outstanding electro-thermal performance and extremely high gauge factors. *Chemical Engineering Journal* **2020**, *385*, 123391,
- [138] Wang, S.; Liu, K.; Yao, X.; Jiang, L. Bioinspired surfaces with superwettability: new insight on theory, design, and applications. *Chemical reviews* **2015**, *115*, 8230-8293,
- [139] Park, J. J.; Hyun, W. J.; Mun, S. C.; Park, Y. T.; Park, O. O. Highly stretchable and wearable graphene strain sensors with controllable sensitivity for human motion monitoring. *ACS applied materials & interfaces* **2015**, *7*, 6317-6324,
- [140] Ryu, S.; Lee, P.; Chou, J. B.; Xu, R.; Zhao, R.; Hart, A. J.; Kim, S.-G. Extremely elastic wearable carbon nanotube fiber strain sensor for monitoring of human motion. *ACS nano* **2015**, *9*, 5929-5936,
- [141] Chen, J.; Zheng, J.; Gao, Q.; Zhang, J.; Zhang, J.; Omisore, O. M.; Wang, L.; Li, H. Polydimethylsiloxane (PDMS)-based flexible resistive strain sensors for wearable applications. *Applied Sciences* **2018**, *8*, 345,
- [142] Yao, H. B.; Ge, J.; Wang, C. F.; Wang, X.; Hu, W.; Zheng, Z. J.; Ni, Y.; Yu, S. H. A flexible and highly pressure-sensitive graphene-polyurethane sponge based on fractured microstructure design. *Advanced Materials* **2013**, *25*, 6692-6698,
- [143] Wei, X.; Cao, X.; Wang, Y.; Zheng, G.; Dai, K.; Liu, C.; Shen, C. Conductive herringbone structure carbon nanotube/thermoplastic polyurethane porous foam tuned by epoxy for high performance flexible piezoresistive sensor. *Composites Science and Technology* **2017**, *149*, 166-177,
- [144] Liu, H.; Dong, M.; Huang, W.; Gao, J.; Dai, K.; Guo, J.; Zheng, G.; Liu, C.; Shen, C.; Guo, Z. Lightweight conductive graphene/thermoplastic polyurethane foams with ultrahigh compressibility for piezoresistive sensing. *Journal of Materials Chemistry C* **2017**, *5*, 73-83,

REFERENCES

- [145] Huang, W.; Dai, K.; Zhai, Y.; Liu, H.; Zhan, P.; Gao, J.; Zheng, G.; Liu, C.; Shen, C. Flexible and lightweight pressure sensor based on carbon nanotube/thermoplastic polyurethane-aligned conductive foam with superior compressibility and stability. *ACS applied materials & interfaces* **2017**, *9*, 42266-42277,
- [146] Liu, X.; Lu, C.; Wu, X.; Zhang, X. Self-healing strain sensors based on nanostructured supramolecular conductive elastomers. *Journal of Materials Chemistry A* **2017**, *5*, 9824-9832,
- [147] Liu, P.; Pan, W.; Liu, Y.; Liu, J.; Xu, W.; Guo, X.; Liu, C.; Zhang, Y.; Ge, Y.; Huang, Y. Fully flexible strain sensor from core-spun elastic threads with integrated electrode and sensing cell based on conductive nanocomposite. *Composites Science and Technology* **2018**, *159*, 42-49,
- [148] Tang, Z.; Jia, S.; Wang, F.; Bian, C.; Chen, Y.; Wang, Y.; Li, B. Highly stretchable core–sheath fibers via wet-spinning for wearable strain sensors. *ACS applied materials & interfaces* **2018**, *10*, 6624-6635,
- [149] Zhong, W.; Liu, C.; Xiang, C.; Jin, Y.; Li, M.; Liu, K.; Liu, Q.; Wang, Y.; Sun, G.; Wang, D. Continuously producible ultrasensitive wearable strain sensor assembled with three-dimensional interpenetrating Ag nanowires/polyolefin elastomer nanofibrous composite yarn. *ACS applied materials & interfaces* **2017**, *9*, 42058-42066,
- [150] Douville, N. J.; Li, Z.; Takayama, S.; Thouless, M. Fracture of metal coated elastomers. *Soft Matter* **2011**, *7*, 6493-6500,
- [151] Shi, X.; Wang, H.; Xie, X.; Xue, Q.; Zhang, J.; Kang, S.; Wang, C.; Liang, J.; Chen, Y. Bioinspired ultrasensitive and stretchable MXene-based strain sensor via nacre-mimetic microscale “brick-and-mortar” architecture. *ACS nano* **2018**, *13*, 649-659,
- [152] Ryu, J. H.; Messersmith, P. B.; Lee, H. Polydopamine surface chemistry: a decade of discovery. *ACS applied materials & interfaces* **2018**, *10*, 7523-7540,
- [153] Lee, H.; Dellatore, S. M.; Miller, W. M.; Messersmith, P. B. Mussel-inspired surface chemistry for multifunctional coatings. *science* **2007**, *318*, 426-430,
- [154] Barclay, T. G.; Hegab, H. M.; Clarke, S. R.; Ginic-Markovic, M. Versatile surface

REFERENCES

modification using polydopamine and related polycatecholamines: Chemistry, structure, and applications. *Advanced Materials Interfaces* **2017**, *4*, 1601192,

[155] Guo, L.; Liu, Q.; Li, G.; Shi, J.; Liu, J.; Wang, T.; Jiang, G. A mussel-inspired polydopamine coating as a versatile platform for the in situ synthesis of graphene-based nanocomposites. *Nanoscale* **2012**, *4*, 5864-5867,

[156] Jiang, J.; Zhu, L.; Zhu, L.; Zhu, B.; Xu, Y. Surface characteristics of a self-polymerized dopamine coating deposited on hydrophobic polymer films. *Langmuir* **2011**, *27*, 14180-14187,

[157] Liu, X.; Cao, J.; Li, H.; Li, J.; Jin, Q.; Ren, K.; Ji, J. Mussel-inspired polydopamine: a biocompatible and ultrastable coating for nanoparticles in vivo. *ACS nano* **2013**, *7*, 9384-9395,

[158] Yan, C.; Wang, J.; Kang, W.; Cui, M.; Wang, X.; Foo, C. Y.; Chee, K. J.; Lee, P. S. Highly stretchable piezoresistive graphene–nanocellulose nanopaper for strain sensors. *Advanced materials* **2014**, *26*, 2022-2027,

[159] Seyedin, S.; Zhang, P.; Naebe, M.; Qin, S.; Chen, J.; Wang, X.; Razal, J. M. Textile strain sensors: a review of the fabrication technologies, performance evaluation and applications. *Materials Horizons* **2019**, *6*, 219-249,

[160] Lee, J.; Kim, S.; Lee, J.; Yang, D.; Park, B. C.; Ryu, S.; Park, I. A stretchable strain sensor based on a metal nanoparticle thin film for human motion detection. *Nanoscale* **2014**, *6*, 11932-11939,

[161] Pu, J.-H.; Zhao, X.; Zha, X.-J.; Bai, L.; Ke, K.; Bao, R.-Y.; Liu, Z.-Y.; Yang, M.-B.; Yang, W. Multilayer structured AgNW/WPU-MXene fiber strain sensors with ultrahigh sensitivity and a wide operating range for wearable monitoring and healthcare. *Journal of Materials Chemistry A* **2019**, *7*, 15913-15923,

[162] Fan, Q.; Qin, Z.; Gao, S.; Wu, Y.; Pionteck, J.; Mäder, E.; Zhu, M. The use of a carbon nanotube layer on a polyurethane multifilament substrate for monitoring strains as large as 400%. *Carbon* **2012**, *50*, 4085-4092,

[163] Ge, J.; Sun, L.; Zhang, F. R.; Zhang, Y.; Shi, L. A.; Zhao, H. Y.; Zhu, H. W.; Jiang, H. L.; Yu, S. H. A stretchable electronic fabric artificial skin with pressure-, lateral

REFERENCES

- strain-, and flexion-sensitive properties. *Advanced materials* **2016**, *28*, 722-728,
- [164] Eom, J.; Jaisutti, R.; Lee, H.; Lee, W.; Heo, J.-S.; Lee, J.-Y.; Park, S. K.; Kim, Y.-H. Highly sensitive textile strain sensors and wireless user-interface devices using all-polymeric conducting fibers. *ACS Applied Materials & Interfaces* **2017**, *9*, 10190-10197,
- [165] Bi, S.; Hou, L.; Zhao, H.; Zhu, L.; Lu, Y. Ultrasensitive and highly repeatable pen ink decorated cuprammonium rayon (cupra) fabrics for multifunctional sensors. *Journal of Materials Chemistry A* **2018**, *6*, 16556-16565,
- [166] Heo, J. S.; Eom, J.; Kim, Y. H.; Park, S. K. Recent progress of textile-based wearable electronics: a comprehensive review of materials, devices, and applications. *Small* **2018**, *14*, 1703034,
- [167] Castano, L. M.; Flatau, A. B. Smart fabric sensors and e-textile technologies: a review. *Smart Materials and structures* **2014**, *23*, 053001,
- [168] Liao, X.; Liao, Q.; Yan, X.; Liang, Q.; Si, H.; Li, M.; Wu, H.; Cao, S.; Zhang, Y. Flexible and highly sensitive strain sensors fabricated by pencil drawn for wearable monitor. *Advanced Functional Materials* **2015**, *25*, 2395-2401,
- [169] Seyedin, S.; Razal, J. M.; Innis, P. C.; Jeiranikhameneh, A.; Beirne, S.; Wallace, G. G. Knitted strain sensor textiles of highly conductive all-polymeric fibers. *ACS applied materials & interfaces* **2015**, *7*, 21150-21158,
- [170] Foroughi, J.; Spinks, G. M.; Aziz, S.; Mirabedini, A.; Jeiranikhameneh, A.; Wallace, G. G.; Kozlov, M. E.; Baughman, R. H. Knitted carbon-nanotube-sheath/spandex-core elastomeric yarns for artificial muscles and strain sensing. *ACS nano* **2016**, *10*, 9129-9135,
- [171] Wu, J.; Zhou, D.; Too, C. O.; Wallace, G. G. Conducting polymer coated lycra. *Synthetic Metals* **2005**, *155*, 698-701,
- [172] Seyedin, S.; Moradi, S.; Singh, C.; Razal, J. M. Continuous production of stretchable conductive multifilaments in kilometer scale enables facile knitting of wearable strain sensing textiles. *Applied materials today* **2018**, *11*, 255-263,
- [173] La, T. G.; Qiu, S.; Scott, D. K.; Bakhtiari, R.; Kuziek, J. W.; Mathewson, K. E.;

REFERENCES

- Rieger, J.; Chung, H. J. Two-layered and stretchable e-textile patches for wearable healthcare electronics. *Advanced Healthcare Materials* **2018**, *7*, 1801033,
- [174] Cai, G.; Yang, M.; Xu, Z.; Liu, J.; Tang, B.; Wang, X. Flexible and wearable strain sensing fabrics. *Chemical Engineering Journal* **2017**, *325*, 396-403,
- [175] Zhang, Y.; He, P.; Luo, M.; Xu, X.; Dai, G.; Yang, J. Highly stretchable polymer/silver nanowires composite sensor for human health monitoring. *Nano Research* **2020**, 1-8,
- [176] Choi, S.; Kwon, S.; Kim, H.; Kim, W.; Kwon, J. H.; Lim, M. S.; Lee, H. S.; Choi, K. C. Highly flexible and efficient fabric-based organic light-emitting devices for clothing-shaped wearable displays. *Scientific reports* **2017**, *7*, 1-8,
- [177] Kwon, S.; Hwang, Y. H.; Nam, M.; Chae, H.; Lee, H. S.; Jeon, Y.; Lee, S.; Kim, C. Y.; Choi, S.; Jeong, E. G. Recent progress of fiber shaped lighting devices for smart display applications—a fibertronic perspective. *Advanced Materials* **2020**, *32*, 1903488,
- [178] Weng, W.; Chen, P.; He, S.; Sun, X.; Peng, H. Smart electronic textiles. *Angewandte Chemie International Edition* **2016**, *55*, 6140-6169,
- [179] Chen, G.; Li, Y.; Bick, M.; Chen, J. Smart textiles for electricity generation. *Chemical Reviews* **2020**, *120*, 3668-3720,
- [180] Afroj, S.; Tan, S.; Abdelkader, A. M.; Novoselov, K. S.; Karim, N. Highly Conductive, Scalable, and Machine Washable Graphene-Based E-Textiles for Multifunctional Wearable Electronic Applications. *Advanced Functional Materials* **2020**, *30*, 2000293,
- [181] Du, D.; Tang, Z.; Ouyang, J. Highly washable e-textile prepared by ultrasonic nanosoldering of carbon nanotubes onto polymer fibers. *Journal of Materials Chemistry C* **2018**, *6*, 883-889,
- [182] Wu, B.; Zhang, B.; Wu, J.; Wang, Z.; Ma, H.; Yu, M.; Li, L.; Li, J. Electrical switchability and dry-wash durability of conductive textiles. *Scientific reports* **2015**, *5*, 11255,
- [183] Cui, H.-W.; Suganuma, K.; Uchida, H. Highly stretchable, electrically conductive textiles fabricated from silver nanowires and cupro fabrics using a simple dipping-

REFERENCES

- drying method. *Nano Research* **2015**, *8*, 1604-1614,
- [184] Li, Y.; Li, Y.; Su, M.; Li, W.; Li, Y.; Li, H.; Qian, X.; Zhang, X.; Li, F.; Song, Y. Electronic textile by dyeing method for multiresolution physical kineses monitoring. *Advanced Electronic Materials* **2017**, *3*, 1700253,
- [185] He, S.; Xin, B.; Chen, Z.; Liu, Y. Flexible and highly conductive Ag/G-coated cotton fabric based on graphene dipping and silver magnetron sputtering. *Cellulose* **2018**, *25*, 3691-3701,
- [186] Kim, S. J.; Song, W.; Yi, Y.; Min, B. K.; Mondal, S.; An, K.-S.; Choi, C.-G. High durability and waterproofing rGO/SWCNT-fabric-based multifunctional sensors for human-motion detection. *ACS applied materials & interfaces* **2018**, *10*, 3921-3928,
- [187] Ren, J.; Wang, C.; Zhang, X.; Carey, T.; Chen, K.; Yin, Y.; Torrissi, F. Environmentally-friendly conductive cotton fabric as flexible strain sensor based on hot press reduced graphene oxide. *Carbon* **2017**, *111*, 622-630,
- [188] Harris, K.; Elias, A.; Chung, H.-J. Flexible electronics under strain: a review of mechanical characterization and durability enhancement strategies. *Journal of materials science* **2016**, *51*, 2771-2805,
- [189] Zhao, Z.; Yan, C.; Liu, Z.; Fu, X.; Peng, L. M.; Hu, Y.; Zheng, Z. Machine-washable textile triboelectric nanogenerators for effective human respiratory monitoring through loom weaving of metallic yarns. *Advanced Materials* **2016**, *28*, 10267-10274,
- [190] Zhang, M.; Wang, C.; Wang, H.; Jian, M.; Hao, X.; Zhang, Y. Carbonized cotton fabric for high-performance wearable strain sensors. *Advanced Functional Materials* **2017**, *27*, 1604795,
- [191] Wang, C.; Xia, K.; Jian, M.; Wang, H.; Zhang, M.; Zhang, Y. Carbonized silk georgette as an ultrasensitive wearable strain sensor for full-range human activity monitoring. *Journal of Materials Chemistry C* **2017**, *5*, 7604-7611,
- [192] Li, P.; Zhang, Y.; Zheng, Z. Polymer-Assisted Metal Deposition (PAMD) for Flexible and Wearable Electronics: Principle, Materials, Printing, and Devices. *Advanced Materials* **2019**, *31*, 1902987,

REFERENCES

- [193] Liu, X.; Chang, H.; Li, Y.; Huck, W. T.; Zheng, Z. Polyelectrolyte-bridged metal/cotton hierarchical structures for highly durable conductive yarns. *ACS applied materials & interfaces* **2010**, *2*, 529-535,
- [194] Ye, Q.; Zhou, F.; Liu, W. Bioinspired catecholic chemistry for surface modification. *Chemical Society Reviews* **2011**, *40*, 4244-4258,
- [195] Wang, W.; Jiang, Y.; Wen, S.; Liu, L.; Zhang, L. Preparation and characterization of polystyrene/Ag core-shell microspheres—A bio-inspired poly (dopamine) approach. *Journal of colloid and interface science* **2012**, *368*, 241-249,
- [196] Yin, Y.; Li, Z.-Y.; Zhong, Z.; Gates, B.; Xia, Y.; Venkateswaran, S. Synthesis and characterization of stable aqueous dispersions of silver nanoparticles through the Tollens process. *Journal of Materials Chemistry* **2002**, *12*, 522-527,
- [197] Ulman, A. Formation and structure of self-assembled monolayers. *Chemical reviews* **1996**, *96*, 1533-1554,
- [198] Gao, J.; Li, B.; Huang, X.; Wang, L.; Lin, L.; Wang, H.; Xue, H. Electrically conductive and fluorine free superhydrophobic strain sensors based on SiO₂/graphene-decorated electrospun nanofibers for human motion monitoring. *Chemical Engineering Journal* **2019**, *373*, 298-306,
- [199] Hu, L.; Pasta, M.; La Mantia, F.; Cui, L.; Jeong, S.; Deshazer, H. D.; Choi, J. W.; Han, S. M.; Cui, Y. Stretchable, porous, and conductive energy textiles. *Nano letters* **2010**, *10*, 708-714,
- [200] Liu, Z.; Zhang, X.; Liu, C.; Li, D.; Zhang, M.; Yin, F.; Xin, G.; Wang, G. Ferroconcrete-inspired design of a nonwoven graphene fiber fabric reinforced electrode for flexible fast-charging sodium ion storage devices. *Journal of Materials Chemistry A* **2020**, *8*, 2777-2788,
- [201] Ding, Y.; Invernale, M. A.; Sotzing, G. A. Conductivity trends of PEDOT-PSS impregnated fabric and the effect of conductivity on electrochromic textile. *ACS applied materials & interfaces* **2010**, *2*, 1588-1593,
- [202] Oh, K. W.; Park, H. J.; Kim, S. H. Stretchable conductive fabric for electrotherapy. *Journal of Applied Polymer Science* **2003**, *88*, 1225-1229,

REFERENCES

- [203] Liu, H.; Li, Q.; Bu, Y.; Zhang, N.; Wang, C.; Pan, C.; Mi, L.; Guo, Z.; Liu, C.; Shen, C. Stretchable conductive nonwoven fabrics with self-cleaning capability for tunable wearable strain sensor. *Nano Energy* **2019**, *66*, 104143,
- [204] Liu, H.; Jiang, H.; Du, F.; Zhang, D.; Li, Z.; Zhou, H. Flexible and degradable paper-based strain sensor with low cost. *ACS Sustainable Chemistry & Engineering* **2017**, *5*, 10538-10543,
- [205] Cassie, A.; Baxter, S. Wettability of porous surfaces. *Transactions of the Faraday society* **1944**, *40*, 546-551,
- [206] Cheng, Y.; Zhang, H.; Wang, R.; Wang, X.; Zhai, H.; Wang, T.; Jin, Q.; Sun, J. Highly stretchable and conductive copper nanowire based fibers with hierarchical structure for wearable heaters. *ACS Applied Materials & Interfaces* **2016**, *8*, 32925-32933,
- [207] Zhang, M.; Wang, C.; Liang, X.; Yin, Z.; Xia, K.; Wang, H.; Jian, M.; Zhang, Y. Weft-knitted fabric for a highly stretchable and low-voltage wearable heater. *Advanced Electronic Materials* **2017**, *3*, 1700193,